MODELING OF HIGH FLUENCE TI ION IMPLANTATION AND VACUUM CARBURIZATION IN STEEL

by

Mukundhan Rangaswamy

Thesis submitted to the Faculty of the

Virginia Polytechnic Institute and State University

in partial fulfillment of the requirements for the degree of

Master of Science

in

Materials Engineering

APPROVED:

D. Farkas, Chairperson

C. R. Houska

C. W. Smith

March 6, 1985

Blacksburg, Virginia

MODELING OF HIGH FLUENCE TI ION IMPLANTATION

AND VACUUM CARBURIZATION IN STEEL

by

Mukundhan Rangaswamy

D. Farkas, Chairperson

Materials Engineering

(ABSTRACT)

Concentration-versus-depth profiles have been calculated for Ti and C in Ti-implanted 52100 steel. A computer formalism was developed to account for diffusion and mixing processes, as well as sputtering and lattice dilation. A Gaussian distribution of Ti was assumed to be incorporated at each time interval. The effects of sputtering and lattice dilation were then included by means of an appropriate coordinate transformation. C was assumed to be gettered from the vacuum system in a one-to-one ratio with the surface Ti concentration up to a saturation point. Both Ti and C were allowed to diffuse. A series of experimental (Auger) concentration-versus-depth profiles of Ti implanted steel were analyzed using the above-mentioned assumptions. A best fit procedure for these curves yielded information on the values of the sputtering yield, range and straggling, as well as the mixing processes that occur during the implantation.

The effective diffusivity of Ti was found to be $6x10^{-15}cm^2/sec$, a value that is consistent with the cascade mixing mechanism. The effective diffusivity of C was found to be $6x10^{-15}cm^2/sec$, and the sputtering yield by Ti atoms was best fit by a value of about 2. The observed range and straggling values were in very good agreement with the values predicted by existing theories, so long as the lattice was allowed to dilate.

ACKNOWLEDGEMENTS

The author would like to thank his committee chairperson, Dr. Diana Farkas, for her invaluable guidance during the course of this study. The author would also like to acknowledge the assistance and cooperation of Dr. C. R. Houska and Prof. C. W. Smith in the production of this thesis.

The author is greatly indebted to Dr. I. L. Singer, of Naval Research Laboratory, for providing the experimental details and for the ensuing discussions. A warm and sincere thanks is also extended to the secretarial staff of the department of Materials Engineering for their help.

Financial support by the Naval Research Laboratory under Grant # N00014-84-M-023 is gratefully acknowledged.

TABLE OF CONTENTS

LIST OF ILLUSTRATIONS

LIST OF TABLES

1.0 INTRODUCTION

In the present work a theoretical model is presented for Ti implantation into AISI 52100 steel and vacuum carburization, a process which resulted in improved tribological properties. A brief description of the implantation process and the applications of ion implantation follows.

1.1 THE ION IMPLANTATION PROCESS

Ion implantation, the process of embedding ions accelerated through high voltages, has been widely used for several years in semi-conductor device manufacture. It is only recently that its potential to modify the surface properties of metals and alloys has been realized. Implantation of ions into metals and alloys differs from implantation into semi-conductors in that, in general, the desired concentration of the ions are several orders of magnitude greater for metals and alloys.

High fluence ion implantation into metals and alloys has proved successful for selectively changing the surface chemistry and microstructure of materials (within about 1 μm of the surface) without changes in bulk chemistry. Super-alloys

with a large concentration of the implanted species can be formed at the surface which cannot be produced by other means. It is possible to alter the composition to a significant extent within limits set by the sputtering of atoms which accompanies the implantation. Defects caused by the energetic ion bombardment can interact both with the host matrix and the implanted atoms to stabilize particular atomic configurations, such as substitutional site occupancy of over-sized impurity atoms; leading at times to the formation of an amorphous layer.

Published literature concerning ion implantation on metallurgical surfaces has demonstrated several beneficial effects on mechanical properties and corrosion resistance.

There are different processes that operate during the implantation process that determine the final concentration distribution. Some of these processes are ion collection, sputtering of atoms, lattice dilation to accommodate the implanted ions, and diffusion due to implantation.

1.2 THE IMPLANTATION PROCEDURE

Ion implantation is a line of sight process wherein ionized atoms or molecules are accelerated through high voltages and then impinge on the surface of the target (1). The process is performed at pressures less than 10^{-6} torr for

two reasons: (1) the ion beam is scattered and adsorbed over short distances by gases at pressures over 10^{-5} torr; and (2) ion-beam-enhanced reaction of environmental gases may produce an undesirable surface chemistry. Since the ion beam carries energy to the work piece, adequate cooling or heat-sinking must also be provided.

The ions, if available in the form of a molecular gas, are ionized in a plasma zone and extracted using an electric field. Metallic ion beams are often produced by passing chlorine gas over a metal powder to produce gaseous metal chloride molecules, which when passed through the plasma split to form metal ions, which are then extracted to produce the initial ion beam. The desired ions are then separated from other impurity atoms using an analyzing magnet. The ion beam then passes through an accelerating potential; is shaped using electrostatic lenses, and electrically rastered to evenly cover the target.

1.3 APPLICATIONS TO CORROSION RESISTANCE

Metallic corrosion is typified by two simultaneous and complementary reactions that together determine the net corrosion rate: anodic oxidation and cathodic reaction (1). Ion implantation may be useful in the reduction of either rate (2). In general, implantation increases corrosion resistance

by adding a chemically reactive species to the bulk material. The beneficial effects of ion implantation on corrosion resistance are represented in the work of Bonara et. al. (3) in acidic and basic environments. There are several other publications (4-7) which describe the beneficial effects of ion implantation on corrosion resistance.

1.4 APPLICATIONS TO MECHANICAL PROPERTIES.

Ion implantation has been found to modify friction and static microhardness (4). Problems peculiar to friction and wear have been reviewed by Hartley (8). Hirvonen (9) and dos Santos et al.(10) have reported major improvements in the wear rate of steels ion-implanted with relatively high doses of nitrogen. Investigations of Ti^+ and N^+-implanted steels have been motivated by tribological studies showing that these two implantation treatments greatly improved the friction and wear properties (11-13). Work on frictional behavior and abrasive resistance of ion implanted AISI 52100 steel has been carried out by Singer and others (14,15).

Improvements in wear-resistance is also effected by interaction of the sputtered surface with residual gases in the vacuum system, forming unexpected surface alloys containing atoms such as carbon (16-18). In addition, the surface has also been found to be amorphous (17,18). Another

case of amorphous alloy formation at the surface due to high fluence implantation of Au into iron has been presented by Poate (19). In general, ion implantation has been found to markedly affect the friction and wear-resistance of metals and alloys.

1.5 TI IMPLANTATION INTO AISI 52100 STEEL

In the present work the case of Ti implanted into AISI 52100 steel, which resulted in a wear-resistant amorphous layer (18) is considered. Implantation to a fluence of 50×10^{16} at/cm^2 is found to produce superior tribological properties. The amorphous layer forms by adsorbing carbon from residual gases in the vacuum chamber (20), assisted by Ti atoms which reach the surface by sputter erosion during implantation (21). The mechanism by which carbon migrates into the solid (thermal diffusion, collision cascades, etc.) is not better understood today than when the effect was first recognized. This is in part due to the lack of appreciation for vacuum/solid interactions but even more to the scarcity of models for high fluence implantation into solids.

In this work a computational method for modeling high fluence implantation is described which calculates Ti and C depth profiles that mimic those observed for the above mentioned Ti implantation into 52100 steel. The model accounts

for ion collection, sputtering and lattice dilation in a manner similar to the earlier treatments by Schultz and Wittmaak (22,23) and Krautle (24). It also considers the diffusion-like transport processes which affect the shape of the evolving profiles and incorporates the vacuum carburization process elucidated by Singer (21). The computational method is based on a numerical solution of the coupled diffusion equations for implanted Ti and adsorbed C. Effective diffusivities for the two species and sputtering yield by Ti ions are obtained by comparison of the calculated and experimental profiles. The experimental data of the room temperature implantation modeled in the present work were obtained by Singer (21). The Auger sputter depth profiles are believed to be accurate to ±20% in both concentration and depth scales.

2.0 THEORETICAL CONSIDERATIONS

The ion collection profile is affected by a number of processes that operate during implantation. These processes include ion collection, sputtering, lattice dilation, radiation-enhanced diffusion and collision-cascade mixing. Other processes that could also affect the ion collection profile are preferential sputtering and radiation-induced segregation, which are not included in the present model.

2.1 ION COLLECTION

An energetic ion entering a thick target will, through collisions with the target nuclei and electrons, lose its energy and finally come to rest. The total distance that the ion travels in coming to rest is called its range; the projection of this distance onto the direction of incidence is called the projected range. These two quantities are defined in Figure 1, where the range is denoted by R and the projected range by R_p. The associated range R_1 is defined as the component of range perpendicular to R_p (25).

Because the number of collisions and the energy transferred per collision (and thus also the scattering angle per collision) are random variables, all ions of a given type

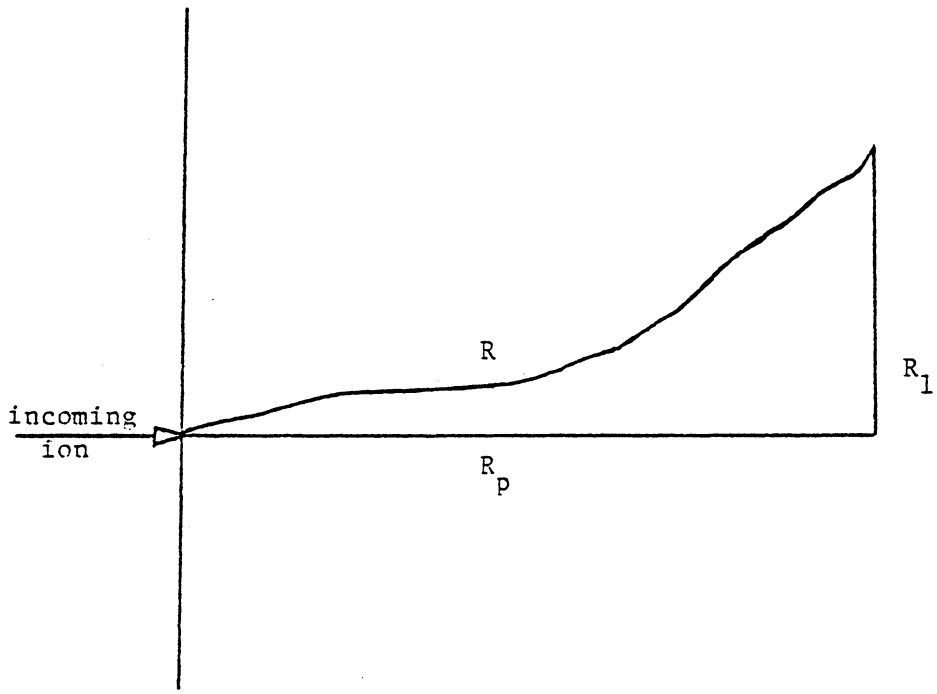

Figure 1. Implanted ion trajectory in the target material.

with given initial conditions will not have the same range. Rather, the ions will form a distribution that must be characterized by quoting a mean ion range, a standard deviation in ion range, and perhaps higher moments of the distribution function. The projected range must also be described statistically.

If the target is amorphous, the range distribution will depend primarily on the energy, mass, and nuclear charge of the incoming ions, and the mass, nuclear charge, and atomic density of the target. Also influential, but of relatively minor importance in most cases, are other parameters, such as target temperature and surface condition. If the target is a single crystal, the range distribution will depend on all these factors, plus many more. Important among these additional parameters are the target lattice parameters, crystallographic orientation, and, depending on temperature, the total ion dose.

Implanting along non-low-index directions in a crystalline target, or implanting into polycrystalline targets yields ion distributions that are adequately characterized by the range statistics for amorphous targets. For many purposes, it is sufficient to represent the distribution in both range and projected range by a Gaussian profile. Considering the projected range distribution for the moment, the Gaussian approximation gives the impurity density n(x) as

$$n(x_p) = \frac{\phi t}{\Delta R_p \sqrt{2\pi}} \exp\left[-(x_p - R_p)^2/(2\Delta R_p^2)\right] \quad (1)$$

where x_p is the depth penetrated, measured along the direction of incidence of the beam;

ϕ = flux of ions in atoms/cm^2.sec;

t = the implantation time in seconds;

ΔR_p = standard deviation in projected range; and

R_p = projected range.

Estimates of the values of R_p and ΔR_p can be obtained using different theories on range distributions such as the statistical amorphous theory of Lindhard, Scharff and Schiott (LSS) (26) or the Monte-Carlo simulation code (TRIM) (27). The Gaussian distribution described by Equation (1) is then representative of the distribution of the incoming flux in the target material.

2.2 SPUTTERING

As the ions impinge on the target, there is an ejection of surface atoms which is dependent on the energy deposited at and immediately below the surface. This removal of surface atoms, causes the surface to recede.

Since the basic experimental work of Almen and Bruce (28,29) on the influence of sputtering on the collection of

noble gas ions in solids, several papers concerning this subject have been published (30-37). Analytical models of ion collection during sputtering have been established in which both the sputtering yield and the range in which both the sputtering yield and the range distribution of the implanted species were assumed to remain unaffected by ion collection (30,34). Numerical analysis of the problem has also been proposed (24). Diffusion has usually been neglected and the effect of lattice dilation was considered only in one case (24).

Schulz and Wittmaak (23) presented a zero order approximation of ion collection during sputtering. In their model, the effects of diffusion, range shortening and recoil implantation were not considered. Lattice dilation was also neglected. Krautle's (24) numerical model considers the sputtering yield as a function of concentration, which changes as the implantation proceeds. This is important if the sputtering yields of the target atoms and the implanted atoms are significantly different. He also takes lattice dilation into account.

At each implantation step, the sputtered layer thickness, 'δx' is calculated from the total number of atoms sputtered by:

$$\delta x = DS/N_o \qquad (2)$$

where, D is the implanted dose in atoms/cm^2;

S is the sputtering yield; and

N_o is the atomic density of the surface layer.

2.3 EFFECT OF LATTICE DILATION

The ion distribution profiles given by LSS theory and the Monte-Carlo simulation do not take into account the expansion resulting from adding ions to the work piece. While this is of negligible consequence at low fluences, the expansion effect is extremely important at higher fluences.

The lattice dilation effect causes the gaussian profiles describing ions implanted early in the process to broaden and penetrate further into the material. Krautle (24) includes the broadening of the target in his model. In his model he considers a layer dx at the depth x from the surface with the concentration $C_n(x)$ of implanted ions. After the additional implantation of atoms, the concentration in this layer increases according to the depth distribution given by the gaussian profile. The implanted ions will increase the concentration to the new density C_{n+1} (x') and the thickness of the layer dx to dx'. At the same time the depth of this layer relative to the surface changes to $x' = x + dx_1$, where dx_1 is due to the accumulated implanted ions. The concentration at the depth x for small fluence is:

$$C(x) = D/\sqrt{2}\Delta R_p \exp[-(x-R_p)^2/2\Delta R_p^2] \quad (3)$$

with

R_p = range of the implanted ions,

ΔR_p = straggling of the ions, and

D = implanted dose.

The implanted ion in a layer dx at the depth x will cause a widening of the layer to dx' and the concentration of the implanted ions will become:

$$C_{n+1}(x) = \frac{[C_n(x) + C(x)]}{[1 + C(x)/N_0]} \quad (4)$$

N_0 being the density of the pure implanted material.

The implanted ions cause an increase of x by dx_1, corresponding to the thickness of a layer containing the amount of implanted atoms until the depth X:

$$dx_1 = 0.5 \left[\operatorname{erf}\left(\frac{R_p}{\sqrt{2}\Delta R_p}\right) + \operatorname{erf}\left(\frac{x-R_p}{\sqrt{2}\Delta R_p}\right) \right] D/N_0 \quad (5)$$

2.4 DIFFUSION LIKE PROCESSES

Diffusion like processes include collision-cascade mixing and radiation enhanced diffusion.

Collision-Cascade Mixing:

The ion on entering the target is slowed down continuously as it interacts inelastically with the electrons in the target. It also collides with the target atom nuclei elastically and transfers energy in discrete quantities with each collision (25). In this elastic collision, a cascade-action takes place when several atoms around the collision point are knocked off their lattice sites. The displaced atoms quickly return to lattice sites, but in a random fashion accompanied by mixing of atoms within the cascade. This mixing is called collision-cascade mixing and is also referred to as ion-beam-mixing (1). This mixing process can be compared to a diffusion process with an effective diffusion coefficient.

Myers (38) has obtained an expression which at least gives an insight into the order of magnitude of this diffusion coefficient. He considers the production of vacancy-interstitial pairs. The creation of a vacancy-interstitial pair moves at least one target atom with respect to the host lattice. If the distribution of momentum transfers is assumed isotropic, the resulting migration is essentially a random-walk process. Adapting the standard expression for thermally activated diffusion in a cubic

lattice to characterize the diffusion coefficient for collision-cascade-mixing gives:

$$D^* = (1/6)\ \lambda^2 P, \tag{6}$$

where λ is the root-mean square separation for a vacancy-interstitial pair and P the number of displacements per target atom per unit time is given by (39):

$$P(x) = (0.8/2NE_d)(dE/dx)\phi \tag{7}$$

where ϕ is the ion flux, N is the atomic density at the solid, E_d is the effective threshold displacement energy, typically ~30 eV, and (dE/dx) is the ion energy deposited per unit depth into atomic processes; E being in eV and dx in nanometers.

The expression for D^* assumes the number of atoms moved by each atomic collision is one. Since a quantitative estimate of λ is not available, and since most of the displaced atoms are ejected from their lattice sites with an energy not much greater than the threshold value, λ is probably several times the nearest-neighbor distance. Values of 1 nm and several nanometers have been used. The main aspect of D^* is that it is dose dependent and not time or temperature dependent.

Radiation Enhanced Diffusion:

Ion bombardment may greatly accelerate the diffusion of substitutional atoms at lower temperatures (38). The increased vacancy concentration due to the irradiation causes a proportional increase in diffusion by the vacancy mechanism. In addition, substitutional atoms are ejected into interstitial sites from which they diffuse rapidly. These two transport processes comprise what is known as "Radiation enhanced diffusion". The major difference between this and collision-cascade-mixing is that enhanced diffusion is dependent on thermally activated defect migration. The overall atomic diffusivity under conditions of enhanced diffusion is governed by the production rate of mobile vacancies and interstitials, by the migration rate of these defects and by the probabilities of their annihilation by recombination, agglomeration, or assimilation into immobile sinks.

In general, the combination of cascade-mixing and radiation-enhanced diffusion produces a net effective diffusivity of the diffusion-like process, which is several orders greater in magnitude than the corresponding thermally activated diffusivity.

3.0 DESCRIPTION OF THE EXPERIMENTAL PROCEDURE

The implantation of the Ti implantation into AISI 52100 steel (Fe-1.5 Cr-1C by weight) samples was done at N.R.L. The details of the procedure were obtained from Reference (21).

3.1 IMPLANTATION

The Ti implantation was carried out using N.R.L.'s modified model 200-20A2F Varian/Extrion ion implanter. The ion source was a hot filament (cathode) arc discharge type. Ti ion beams were produced by employing an internal chlorination technique: chlorine gas was passed through fine titanium powder contained in a graphite chamber mounted within the source, near the filament, producing titanium chlorides; which volatilize at the high source temperature (800°C) and subsequently ionize. This technique produced ion beam intensities of about 200 μA of $^{48}Ti^{+}$.

The AISI-52100 steel samples, disks 0.95 cm in diameter and 0.32 cm thick, were heat-sunk onto a water-cooled holder so that the temperature was maintained at less than 40°C throughout the implantation process. The samples were implanted simultaneously with 190 keV or 55 keV $^{48}Ti^{+}$ ions in

a target chamber that was cryogenically pumped to pressures of about 5×10^{-5} torr. The ion beam was scanned electrostatically over the sample holder to give a unknown current density of 10 to 20 $\mu A/cm^2$ as measured with a built-in Faraday cup. The implantation was interrupted when fluences of 5×10^{16} at/cm^2, 16×10^{16} at/cm^2 and 40×10^{16} at/cm^2 were obtained, to remove the samples and then continued (for the 190 keV case) upto a fluence of 50×10^{16} at/cm^2. The concentration profiles obtained are given in Figure 2. The figure also shows significant carbon concentrations. The presence of carbon could be explained by gettering of carbonaceous residual gases in the vacuum chamber during implantation. A model for the pickup of carbon is presented further on.

3.2 AUGER ANALYSIS

Auger analysis was performed in a UHV chamber equipped with a Perkin-Elmer (PHI) model 545 Auger microprobe, a rasterable ion gun, a Ti sublimator and liquid nitrogen cooled cryopanels. The electron gun was operated at 2 kV, with a 1 μA beam current, rastered over a spot size of 50 μm to reduce the intensity. Auger derivative spectra were recorded either directly or by a peak-height recording multiplexer with a 3 eV modulation amplitude. The ion gun

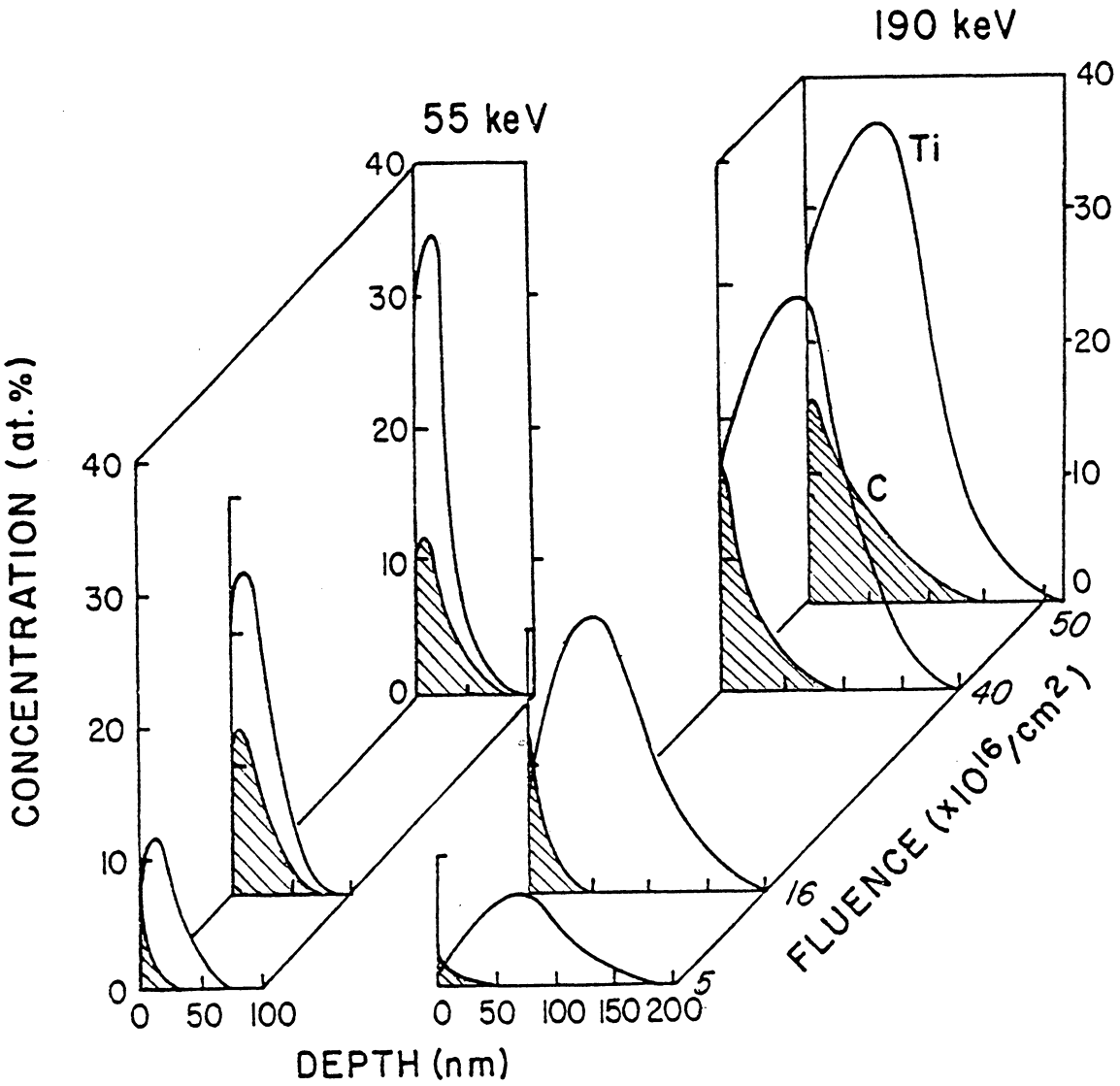

Figure 2. Concentration vs depth profiles for Ti and C in Ti-implanted 52100 steel at several fluences and energies, obtained by Auger sputter profiling. (Left) 5, 16, and $40 \times 10^{16} Ti^{+}/cm^{2}$ at 55keV; (right) 5, 16, 40, and $50 \times 10^{16} Ti^{+}/cm^{2}$ at 190 keV. Note: bulk C concentration of the steel (4 at. %) was subtracted from data (Ref. 21).

was operated in an Ar atmosphere (about 5 x 10^{-5} torr) with a rastered beam of 2 keV Ar^+ ions, at selected current densities between 2 and 30 $\mu A/cm^2$. Depth profiles were recorded during ion milling with Ti sublimators operating and cryopanels cooled to liquid nitrogen temperature. These procedures reduced contamination of ion-milled surfaces by residual gas vapors to below detectable levels.

3.3 VACUUM CARBURIZATION MODEL

Vacuum carburization of Ti-implanted steel can be understood in terms of the four step process illustrated in Fig. 3:

1) sputtering uncovers implanted Ti;
2) surface Ti atoms adsorb carbonaceous molecules from residual gases in the vacuum chamber;
3) surface carbide species are formed by dissociation; and
4) surface carbon atoms diffuse inward.

Each of these steps will be treated in detail here.

Sputtering:

During implantation, ions sputter erode the surface in passage to their ultimate resting place. Sputtering is evident in the Ti profiles of Fig. 2, especially at higher

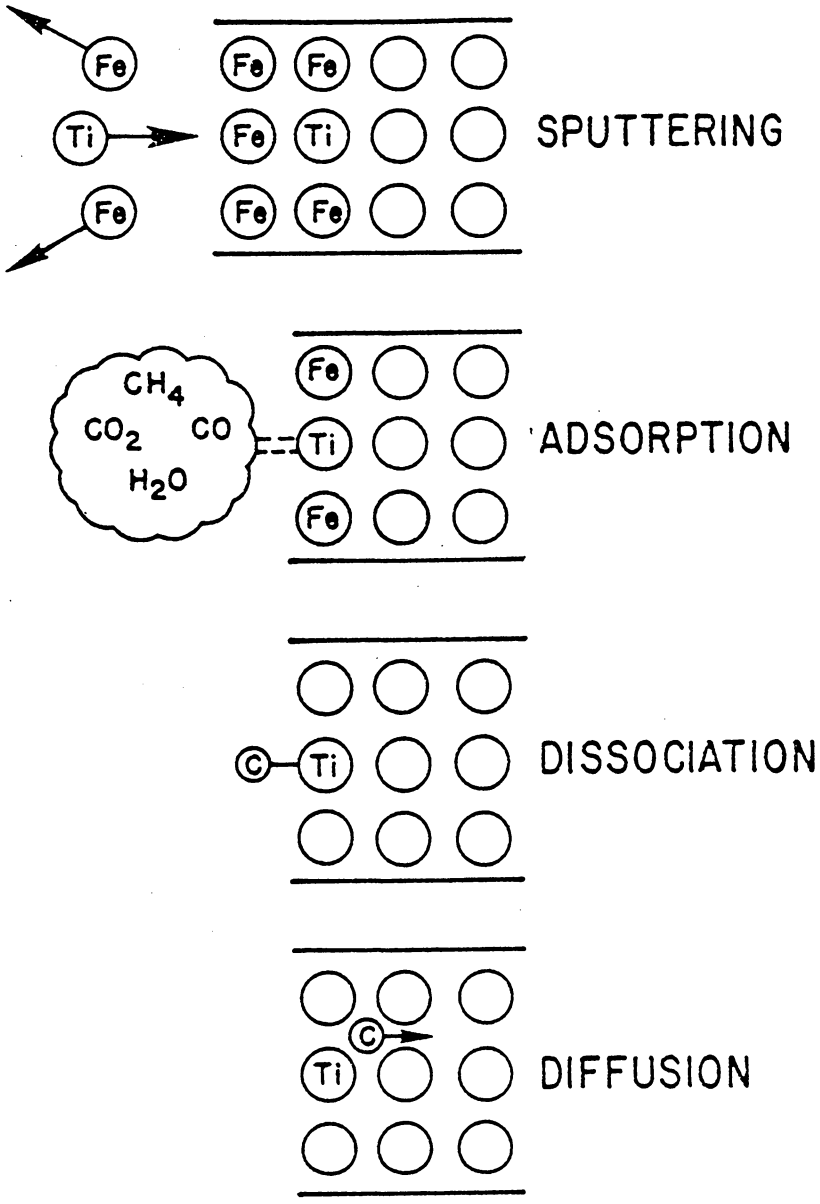

Figure 3. An illustration of the four atomic processes involved in vacuum carburization during Ti-implantation of Fe.

fluences. Ion erosion brings implanted Ti atoms to the surface, the vacuum-solid interface.

Adsorption:

Once at the surface, Ti atoms are bombarded continually by residual gas molecules present in the vacuum chamber. In chambers routinely opened to air and cycled without baking, carbonaceous gas molecules such as CO and CO_2 are major constituents of the residual gases (Ref. 40). At vacuum pressures of approximately $p = 1 \times 10^{-6}$ torr, typical of present day implanters, residual gas molecules strike each surface atom once each second.

Whether or not carbonaceous gas molecules are adsorbed by surface atoms depends on their mutual affinity. Ti is known to have a high affinity for a molecule like CO, and at low surface coverage the sticking probability can be as high as one (Ref. 41). To maintain an adsorbed layer, the flux of residual gas molecules which "stick" must exceed the flux of surface atoms sputtered off. Even under optimal implantation conditions ($p \sim \times 10^{-6}$ torr and ion current density $J = 20\ \mu A/cm^2$), sputtering cannot remove all the adsorbed molecules from surface Ti atoms: for a sputtering yield of $S = 3$ atoms/ion (Ref. 42) the erosion flux for $J = 20\ \mu A/cm^2$ is 4×10^{14} atoms/cm^2-sec, or 1/3 of the residual gas flux.

Dissociation:

Adsorbed carbonaceous gas molecules cannot themselves carburize the surface; they must first dissociate forming surface carbide species. In recent years, there have been many surface analytical studies of CO adsorption on Ti, both experimental (Ref. 41,43) and theoretical (Ref. 44), and all have concluded that dissociative adsorption occurs at or above temperatures T = 300K. Most Auger spectroscopists who have had the occasion to sputter clean reactive metals such as Ti are familiar with the buildup of carbide species adsorbed from residual gases, even in UHV chambers. Moreover, surface carbide species, even under electron and ion bombardment, are quite tenacious unlike surface oxide species, which tend to dissociate and desorb in the presence of electrons (electron stimulated desorption) (Ref. 45).

Diffusion:

Surface carbide species are well attached to the surface (Ref. 44). They may not desorb, like surface oxide species. They may however dissociate, freeing C atoms to diffuse inwards (as dictated by the thermodynamics).

Subsurface [C], barely detectable (~1 at.%) below 5 x 10^{16} Ti/cm^2 at 190 keV, rose to a significant fraction of the near surface concentration at a fluence of 50 x 10^{16}Ti/cm^2. At 55 keV, however, [C] comprised a significant fraction of the near surface concentration even at a fluence of 16 x 10^{16}Ti/cm^2. In general, the subsurface C buildup began at lower fluences for lower implantation energies and ultimately saturated at lower fluences for lower energies (compare 16 and 40 x $10^{16}Ti^+/cm^2$ for 55 keV versus 190 keV in Fig. 2). The concentration of C at the surface $[C]^s$, increased with fluence and energy in the same manner as the subsurface C concentration. This behavior is also expected for a diffusion-like profile.

The surface concentrations $[T]^s$ and $[C]^s$ showed similar fluence and energy dependence and, during the early stages of C buildup, were nearly equal in value. Ti and C also bonded chemically at the surface as inferred from Auger lineshape analysis.

Auger derivative spectra, shown in Fig. 4a, are representative of spectra obtained from implanted surfaces after ion milling through a thin oxide layer. The lineshape of the C(KLL) spectrum is identical to that observed for C(KLL) in TiC (Ref. 46), shown in Fig. 4b, and can easily be distinguished from other forms of carbon (Ref. 43), even the carbide present in 52100 steel (Ref. 18). The Ti (LMM)

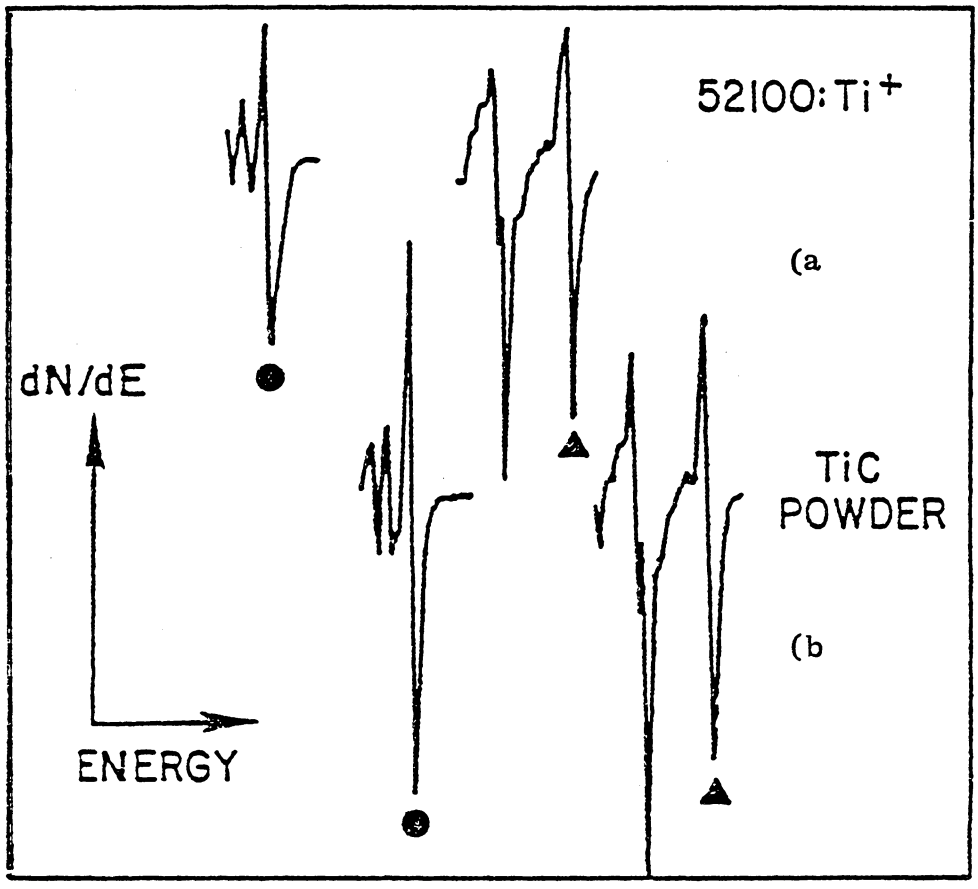

Figure 4. Auger derivative spectra of C(KLL) and Ti(LMM) energy regions of(a) Ti-implanted 52100 steel at the oxide/metal interface and (b) ion milled TiC powder. (• indicates 272 eV C peak; Δ, 420 eV Ti peak.

spectrum also shows a lineshape identical to that observed in TiC (Ref. 46), shown in Fig. 4b. C atoms, therefore, were bonded to Ti atoms at the surface.

The affinity of Ti for C at the surface, the parallel increases of $[T])^s$ and $[C]^s$ with fluence and energy, and the diffusion-like profile of C can all be explained by a model in which C is gettered from the vacuum chamber by Ti atoms that reach the surface during sputtering. This hypothesis, put forth several years ago (Ref. 18), was recently verified (Ref. 20). In the experiment, isotopic ^{13}CO gas was back-filled into a vacuum chamber during Ti implantation of steel surfaces. Secondary ion mass spectroscopy detected ^{13}C profiles like those shown in Fig. 2 at concentrations two orders of magnitude greater than found in steels implanted without residual ^{13}CO gas. It has, therefore, been shown that implanted Ti, after sufficient sputtering of the host steel, can getter residual gases from a vacuum chamber. This process will hereafter be referred to as vacuum carburization.

4.0 NUMERICAL METHOD FOR DIFFUSION CALCULATIONS.

The diffusion of C or Ti can be described by Fick's second law (47):

$$\frac{\partial c}{\partial t} = \frac{\partial}{\partial x}\left[D\left(\frac{\partial c}{\partial x}\right)\right] \tag{8}$$

For the case where D is not a function of concentration, Eq. (8) reduces to:

$$\frac{\partial c}{\partial t} = D\,\frac{\partial^2 c}{\partial x^2} \tag{9}$$

The most useful methods for solving differential equations such as the diffusion equation are the finite-difference techniques. One of these, the Crank-Nicolson finite difference analog is second-order correct with respect to both independent variables x and t and, in addition, stable over a large range of increments of the variables (48,49).

The finite difference technique employs a one-dimensional space grid. L is the total length of the grid, as shown in Figure 5. C_i represents the concentration at any grid point i or nude along the grid. The diffusion problem is bounded spatially by a boundary condition at the surface at grid point i = 1 and a zero mass transfer boundary where the gradient $\partial c/\partial x = 0$ at x = L, that is at grid point

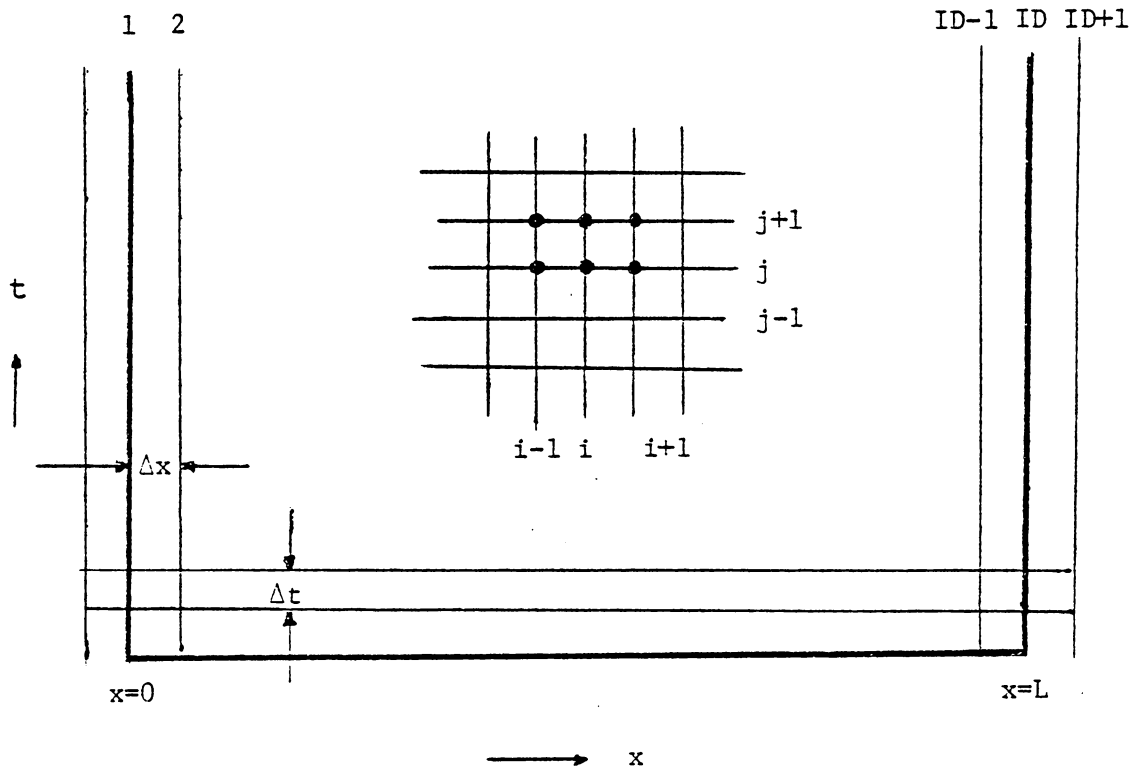

Figure 5. Illustration of the finite-difference grid.

$i = ID$. The size of each grid spacing Δx is equal to $L/(ID-1)$.

The finite difference equations used in the Crank-Nicolson method to solve Eq. (9) are presented below:

$$\frac{\partial c}{\partial t} = (c_{i,n+1} - c_{i,n})/\Delta t \tag{10}$$

$$\frac{\partial^2 c}{\partial x^2} = (1/2\Delta x^2)\ (c_{i+1,n+1} - 2c_{i,n+1} + c_{i-1,n+1} + c_{i+1,n} - 2c_{i,n} + c_{i-1,n}) \tag{11}$$

At any time step, $C_{i-1,n}$, $C_{i,n}$, $C_{i+1,n}$ are known values and $C_{i-1,n+1}$, $C_{i,n+1}$, $C_{i+1,n+1}$ are unknown values. The subscripts i and n refer to the space position of a particular grid point (Fig. 5) and the time step respectively. The time increment between time step n and n+1 is given by Δt.

For a ternary system the generalized Fick's equations for the flux of elements 1 and 2 in terms of the concentration gradients are:

$$J_1 = -D_{11}\frac{\partial c_1}{\partial x} - D_{12}\frac{\partial c_2}{\partial x} \tag{12a}$$

$$J_2 = -D_{22}\frac{\partial c_2}{\partial x} - D_{21}\frac{\partial c_1}{\partial x} \tag{12b}$$

D_{11} and D_{22} are measures of the effect of the concentration gradient of a given component on its own flux; whereas D_{12}

and D_{21} reflect cross-effects usually referred to as the ternary diffusional interaction. Combining Eq. (12) with the continuity equation and assuming that the ternary coefficients are composition independent, the Fick's second law for a ternary system is:

$$\frac{dc_1}{dt} = D_{11} \frac{\partial c_1}{\partial x^2} + D_{12} \frac{\partial c_2}{\partial x^2} \tag{13a}$$

$$\frac{dc_2}{dt} = D_{22} \frac{\partial c_2}{\partial x^2} + D_{21} \frac{\partial c_1}{\partial x^2} \tag{13b}$$

Components 1 and 2 may be taken as carbon and titanium respectively. Component 3 is the iron solvent.

The Crank-Nicolson finite difference technique can also be used to solve Eqs. (13) for both C_1 or [C] and C_2 or [Ti]. The finite difference equations used in the Crank-Nicolson method to solve Eqs. (12) and (13) are given by Eqs. (10) and (11). By combining Eqs. (10), (11), (12) and (13) and using the boundary condition that links the surface concentration of carbon to that of titanium, one obtains a system of linear equations:

$$(D)_n = (A)\ (X)_n \tag{14a}$$

$$(X)_n = ([C]_{i,n}\ ,\ [Ti]_{i,n}) \tag{14b}$$

$$(D)_n = (d^1_{i,n},\ d^2_{i,n}) \tag{14c}$$

$$d^1_{i,n} = (D_C \Delta t/2\Delta x^2)(2[C]_{i,n} - [C]_{i+1,n} - [C]_{i-1,n}) - [C]_{i,n} \tag{14d}$$

$$d^2_{i,n} = (D_{Ti} \Delta t/2\Delta x^2)(2[Ti]_{i,n} - [Ti]_{i+1,n} - [Ti]_{i-1,n}) - [Ti]_{i,n} \tag{14e}$$

where [C], [Ti] denote the concentrations of carbon and titanium, respectively. D_C and D_{Ti} are the apparent diffusivities of carbon and titanium, respectively. A is a bi-tridiagonal matrix :

$$A = \begin{bmatrix} b & c & 0 & . & . & . \\ a & b & c & 0 & . & . \\ 0 & a & b & c & . & . \\ 0 & 0 & a & b & . & . \\ 0 & 0 & 0 & a & . & . \\ . & . & . & . & . & . \end{bmatrix} \tag{15}$$

where,

$$a = c = \begin{bmatrix} \frac{D_C \Delta t}{2\Delta x^2} & 0 \\ 0 & \frac{D_{Ti} \Delta t}{2\Delta x^2} \end{bmatrix}$$

$$b = \begin{bmatrix} \frac{-D_C \Delta t}{\Delta x^2} - 1 & 0 \\ 0 & \frac{-D_{Ti} \Delta t}{\Delta x^2} - 1 \end{bmatrix}$$

The coefficients a, b, c and the term d_i are constants. The

d_i are determined at each time interval. The matrix A can be inverted with standard subroutines. The concentrations at time step n+1 can be obtained from the concentrations at step n as,

$$(X)_{n+1} = (A)^{-1} (D)_n. \tag{16}$$

The calculation of the C and Ti gradient proceeds in the following manner: an initial [C] and [Ti] profile is specified (usually zero) as well as the appropriate ternary diffusion coefficients, D_{11}, D_{22}, D_{12}, D_{21} and boundary conditions. In the present model, the cross-diffusion coefficients D_{12} and D_{21} were made equal to zero. For each new time step N+1 of Δt's, a new set of concentrations $[C]_{i,n+1}$, $[Ti]_{i,n+1}$ are obtained for each grid point. In the same time step coordinate transformations to account for surface recession due to sputtering and lattice dilation are also carried out. The method for determining the extent of surface recession and lattice dilation is described in chapter (5).

The specification of Δx and Δt is relatively flexible in the Crank-Nicolson method. In the forward finite difference technique stability requires that

$$D\Delta t/(\Delta x)^2 \leq 1/2 \tag{17}$$

In this work the initial value of Δt was taken so that Eq. (17) was satisfied. After each profile generation, a new value of surface concentration was used for the next time increment.

5.0 DESCRIPTION OF THE FORMALISM

The profile of Ti implanted to high fluences is affected by four processes:

- Ion collection;
- Diffusion-like broadening resulting from the collision cascades or radiation-enhanced diffusion;
- Sputter erosion of the surface;
- Lattice dilation as a result of ion collection.

The adsorbed C profiles are affected by two processes:

- Surface buildup of C as a function of time;
- Diffusion-like penetration.

These processes and the way in which they are treated in the present formalism are described in detail in the following sections.

5.1 ION COLLECTION

The ion collection was described by a gaussian distribution given by Eq. (1) for a very small time Δt, the time increment in the finite difference grid used. In the present formalism the collection of the implanted atoms at a depth x was given by:

$$dC_{Ti}(x) = \frac{\phi \Delta t}{\Delta R_p \sqrt{2\pi}} \exp\left[-(x-R_p)^2/(2\Delta R_p^2)\right] \tag{18}$$

The new concentration of Ti at all depths was determined after accounting for the lattice dilation introduced by ion collection.

5.2 DIFFUSION-LIKE PROCESSES

The term "diffusion-like" is used here to denote transport processes that obey Fick's second law (47):

$$\frac{\partial [Ti]}{\partial t} = D_{Ti} \frac{\partial^2 [Ti]}{\partial x^2} \tag{19a}$$

$$\frac{\partial [C]}{\partial t} = D_C \frac{\partial^2 [C]}{\partial x^2} \tag{19b}$$

where [C] and [Ti] denote the concentrations of carbon and titanium respectively, and D the effective diffusivity. These equations describe thermal and radiation-enhanced diffusion, as well as cascade mixing.

Equations (19a) and (19b) were solved for D_{Ti} and D_C values which best fit all the experimental curves illustrated in Fig. 2. Eltoukhy et al. (50) calculated diffusion profiles on the assumption of a diffusivity that varied exponentially with depth and compared the results with those

obtained for constant diffusivity. They concluded that a constant enhancement approximation introduced negligible errors. In these calculations D_{Ti} and D_C were approximated as constants, as suggested by the calculations of Eltoukhy et al. Non-zero values for D_{Ti} indicate the relative importance of diffusion-like mixing under the conditions of implantation studied. It is reemphasized that both D_C and D_{Ti} should be considered as effective diffusivities, since they may result from processes other than thermally activated diffusion.

The solution of Eqs. (19) required the definition of boundary conditions. The ion collection process, as described below, was used as a boundary condition for Eq. (19a). For Eq. (19b) the boundary condition was the surface carbon concentration as a function of time, as obtained from the model for vacuum carburization as described in chapter (3).

The vacuum carburization model predicted a surface concentration of C that was proportional to the amount of Ti exposed at the surface. As a first approximation it could be assumed that every exposed Ti atom adsorbs a C atom. This assumption was justified by the experimental data for surface contents up to concentrations around 16 at% where there appeared to be a saturation of the adsorbed carbon. Therefore, the boundary condition used in the solution of Eq. (19b) was that the C and Ti concentrations become equal at the surface.

The diffusion equations (19a) and (19b) were solved by a finite difference technique, the Crank-Nicholson method. The finite difference method, described in more detail in chapter (4), was based on a space-time grid. The size of the space increment Δx was taken to be 1/30 of the total depth of penetration, and the size of the time increment Δt was taken as 1/50 of the total time of implantation for the particular fluence considered. The coupling between the two differential equations introduced by the boundary conditions required that the two equations be solved simultaneously. At each time step the profiles were adjusted as follows : A Gaussian distribution of collected Ti was added to the existing profile, which was initially zero; the C concentration at the surface was made equal to the Ti concentration; and the depth coordinates were transformed to account for the sputter erosion of the surface and the lattice dilation.

5.3 SPUTTERING

The sputtering process assumed a constant sputtering yield. The amount sputtered away, δx, during a time period, Δt, was calculated as:

$$\delta x = (\phi \; S \; \Delta t)/n_0 \qquad (20)$$

where ϕ is the number of incoming ions per unit time per unit area, S is the sputtering yield, and n_o is the atomic density of the implanted target.

The coordinate transformation corresponding to the recession of the surface due to sputtering was given by:

$$x'(I) = x(I) - \delta x \tag{21}$$

5.4 LATTICE DILATION

The method used to account for the effect of lattice dilation was similar to that used by Krautle (24). The atomic density n_o of the material was considered constant and the dilation of each space interval Δx was made proportional to the increment of implanted species collected in that space interval. In Krautle's calculations the total shift of a point x was computed analytically as the integral of the Gaussian distribution of the implanted species.

However, in our calculations, it was found more convenient to obtain the cumulative shift of a point x as a sum of the incremental dilations. The procedure followed to calculate the cumulative shift of a particular point x at node I was as follows: An increment Δx of index I was dilated during time Δt by an amount dx

$$dx(I) = \frac{\Delta x.\phi.\Delta t}{n_0} \cdot \frac{1}{\Delta R_p\sqrt{2\pi}} \exp\left[-(I\Delta x-R_p)^2/(2\Delta R_p^2)\right] \quad (22)$$

Thus after each implantation increment, coordinate x' is transformed to x" as :

$$x''(I) = x'(I) + \varepsilon(I) \quad (23)$$

where $\varepsilon(I)$ is the cumulative dilation of increment I, given by:

$$\varepsilon(I) = \sum_{k=0}^{I} dx(k) \quad (24)$$

The total coordinate transformation made in a time Δt is obtained from Eqs. (21) and (23). A schematic representation of the surface recession due to sputtering and effect of lattice dilation is shown in Figure 6.

In each time interval Δt, the effects of ion collection, sputtering, lattice dilation and diffusion were considered. All these processes were included within the finite difference formulation to solve the partial differential equations of Fick's second law for Ti and C. Within the time interval, the new concentrations were determined which were used as initial concentrations for the next time interval. The process was repeated in successive time intervals till the required fluence was reached at which point an output containing the concentration profile was generated.

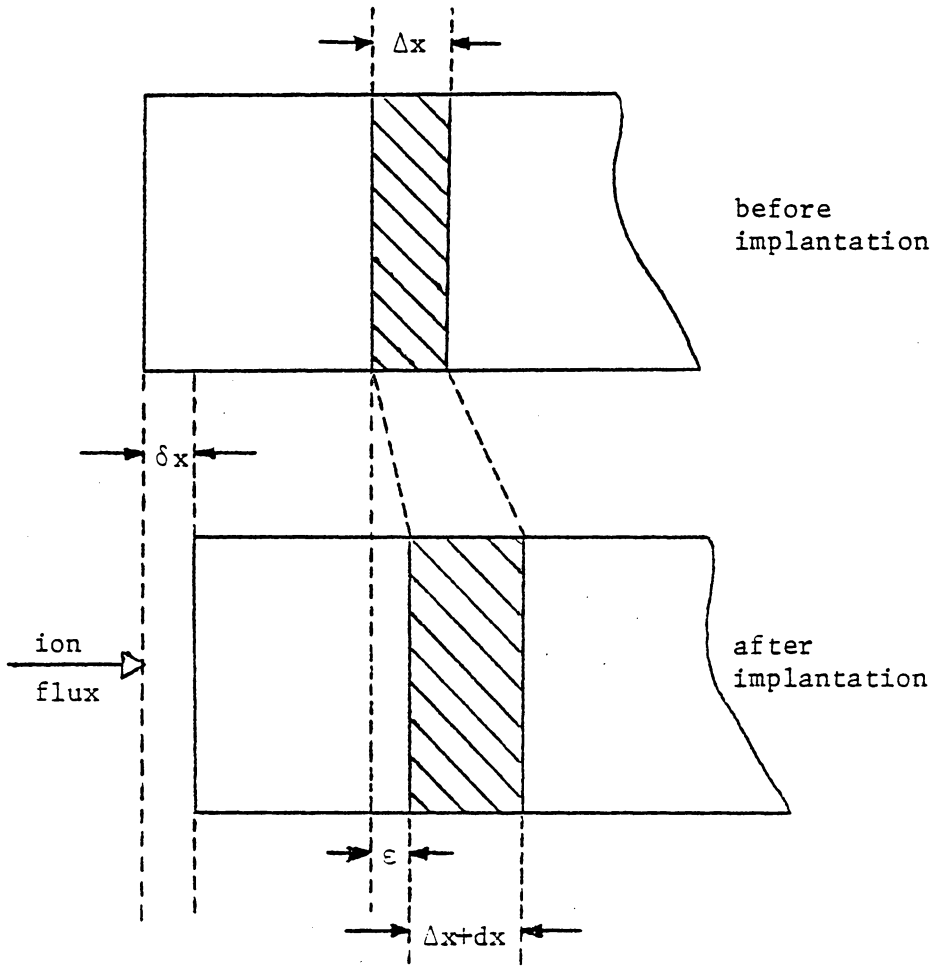

Figure 6. Schematic diagram of sputtering and lattice dilation.

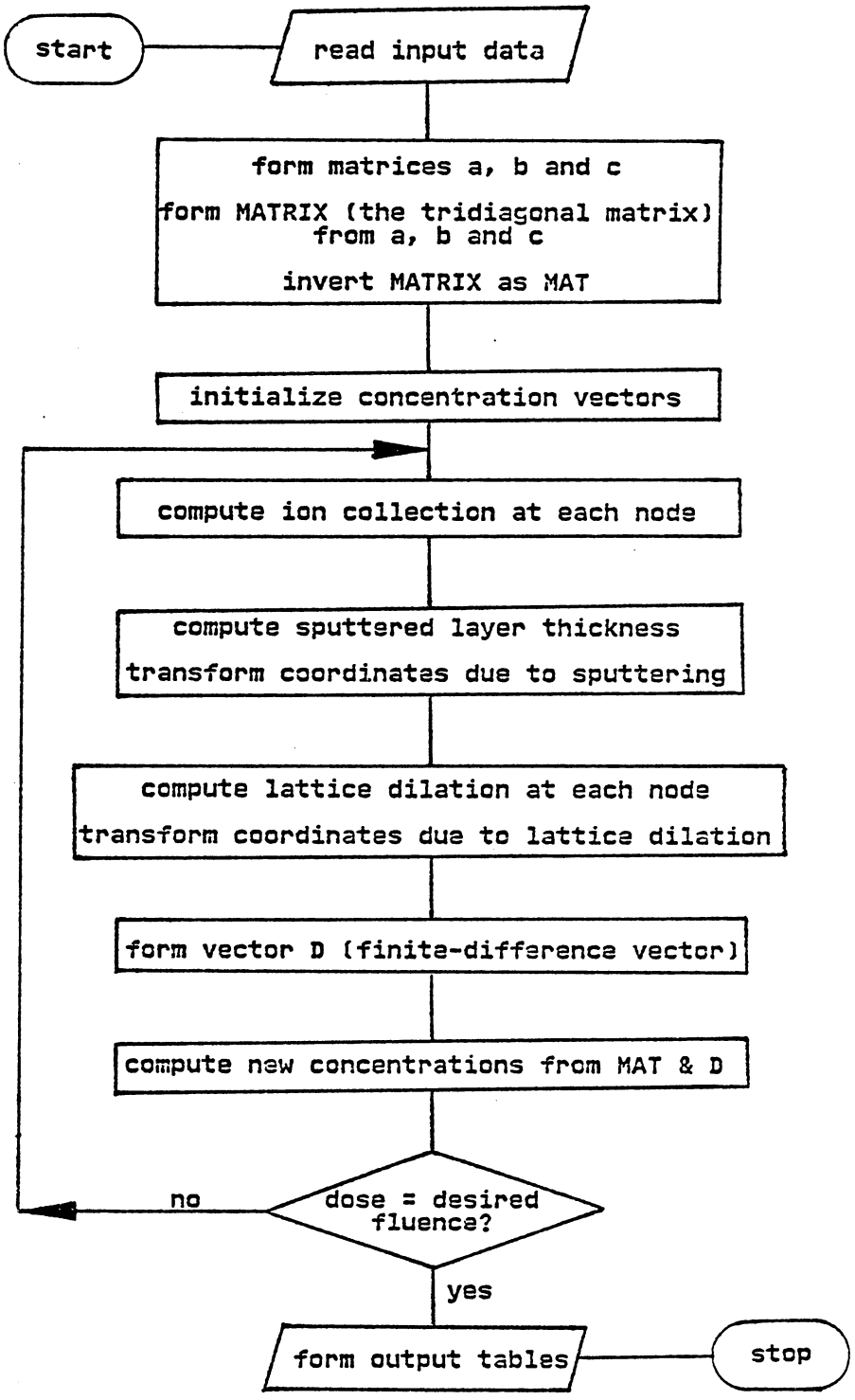

Figure 7. Flow-Chart for the program 'IMPLANT'.

The general procedure of the program 'IMPLANT' used to generate the ion implantation concentration profiles is illustrated in Fig. 7. A listing of the program 'IMPLANT' is included in the appendix. The program used to plot the calculated concentration profiles is also included in the appendix.

6.0 RESULTS

The formalism described required the input of the following parameters:

- Range R_p and range straggling ΔR_p of Ti ions in steel. These values were obtained from calculations done using LSS theory as described in the Manning and Mueller procedure (26). The values are shown in Table I.
- Flux of the incoming ions, ϕ, which was obtained from the experimental conditions as fluence per unit time. The Ti flux was converted to added thickness per unit time, using the atomic density n_o of the 52100 steel. (ϕ = 9.26×10^{13} at/sec cm², $n_o = 8.21 \times 10^{22}$ at/cm^3)
- Effective diffusivity of C, which was varied in order to obtain a good fit with the experimental C profiles.
- Effective diffusivity of Ti, which was varied in order to obtain the best fit to the experimental Ti profiles.
- Sputtering yield, S. A value of the sputtering yield was obtained directly from the experimental

TABLE I : Range and Straggling values using LSS Theory

Energy	Most probable range R_p	Range straggling ΔR_p
55 keV	20 nm	8.6 nm
190 keV	59 nm	23 nm

data and indirectly by comparing computed curves using varying sputtering yields to the experimental profiles in a best fit procedure.

6.1 ESTIMATE OF THE SPUTTERING YIELD

A value of the sputtering yield was obtained directly from experimental data by considering the areas under the Ti profiles as a function of fluence and sputtering yield. The amount of Ti sputtered away is proportional to the surface concentration of Ti, the incoming flux and the sputtering yield. The retained dose of Ti, A(t), is given by an integral over time of the incoming flux minus whatever was sputtered away.

$$A(t) = \int_0^t [f/n_0 - S(f/n_0)[Ti]^s(t)]\, dt \qquad (25)$$

where $[Ti]^s(t)$ is the surface concentration of Ti at time t. Schultz and Wittmaak calculated an expression for the surface concentration of an implanted species in the presence of sputtering, obtaining an expression in terms of error functions. In the present calculation the experimental data for the surface concentration was approximated by a linear function. This was a good approximation for low fluences.

$$[Ti]^s(t) = kt \qquad (26)$$

where k is the slope of the surface concentration versus time curve and is obtained directly from experimental data. This was shown to be a good approximation for the 190 keV case (18). The sputtering yield was calculated by substituting Eq. (26) into Eq. (25) and integrating. The analysis resulted in a value of S = 1.9 for Ti implantation in 52100 steel.

6.2 ESTIMATE OF TI DIFFUSIVITY

An estimate of the order of D_{Ti} was obtained using the Kinchin-Pease relation described by Eq. (7), and Eq. (6). Substituting Eq. (7) in Eq. (8) resulted in:

$$D^* = (1/6)\lambda^2(0.8/2N_0E_d)(dE/dx)\phi \qquad (27)$$

For the 190 keV case, an approximate estimate of (dE/dx) gave

$$dE/dx = 190 \text{ keV}/59 \text{ nm} = 3.2\text{x}10^{10}\text{eV/cm}.$$

Similarly, for the 55 keV case,

$$dE/dx = 55 \text{ keV}/20 \text{ nm} = 2.7\text{x}10^{10}\text{eV/cm}.$$

This resulted in an average dE/dx of $3x10^{10}$ eV/cm.

With E_d ~ 30 eV;

ϕ = $9.26x10^{13}$ Ti/cm²-sec;

N_0 = $8.21x10^{22}$ at/cm^3; and

λ of the order of 2 nm,

Eq. (27) yielded D^* = $5.33x10^{-15}$cm^2/sec, i.e. of the order of $5x10^{-15}$cm^2/sec.

6.3 FITTING OF THE PARAMETERS S, D_{TI} AND D_C

Lattice dilation effect:

Lattice dilation was found to be very important. Calculations performed without lattice dilation required range and range straggling values that were very much different from the ones predicted by the Manning and Mueller formalism which is based on LSS theory. This is illustrated in Figs. 8-14. The lowest fluences could be fitted very well with the values predicted by LSS theory since the effects of lattice dilation were insignificant in their cases. The fitted values for the highest fluence of the 190 keV implant were R_p = 90 nm and ΔR_p = 50 nm, which are almost double the LSS values shown in Table 1. Since this discrepancy is unlikely, it was concluded that the lattice dilation effect is abso-

lutely necessary to describe high fluence ion implantation profiles.

The next series of calculations included the lattice dilation effect but did not consider a diffusion-like process for Ti. The calculated curves were consistently narrower than the experimental ones, suggesting that a diffusion-like process was in fact necessary to account for the observed results. When both diffusion and lattice dilation were included in the calculations, only one combination of S and D_{Ti} values resulted in Ti profiles that fit all seven measured profiles. These values were $D_{Ti} = 6x10^{-15} cm^2/sec$ and S = 2.

Sputtering Effect:

The sensitivity of the profiles to the value of S can be seen in Figs. 15-21. These figures show calculated and experimental [Ti]-versus-depth profiles for all the seven cases studied. As expected, the effect of increasing sputtering yield is to move the profiles closer to the surface. The value of S that best describes the experimental curves seems to decrease from a value somewhat greater than 2 to a value less than 2 as the fluence increases. This is consistent with the value of 1.9 derived directly from exper-

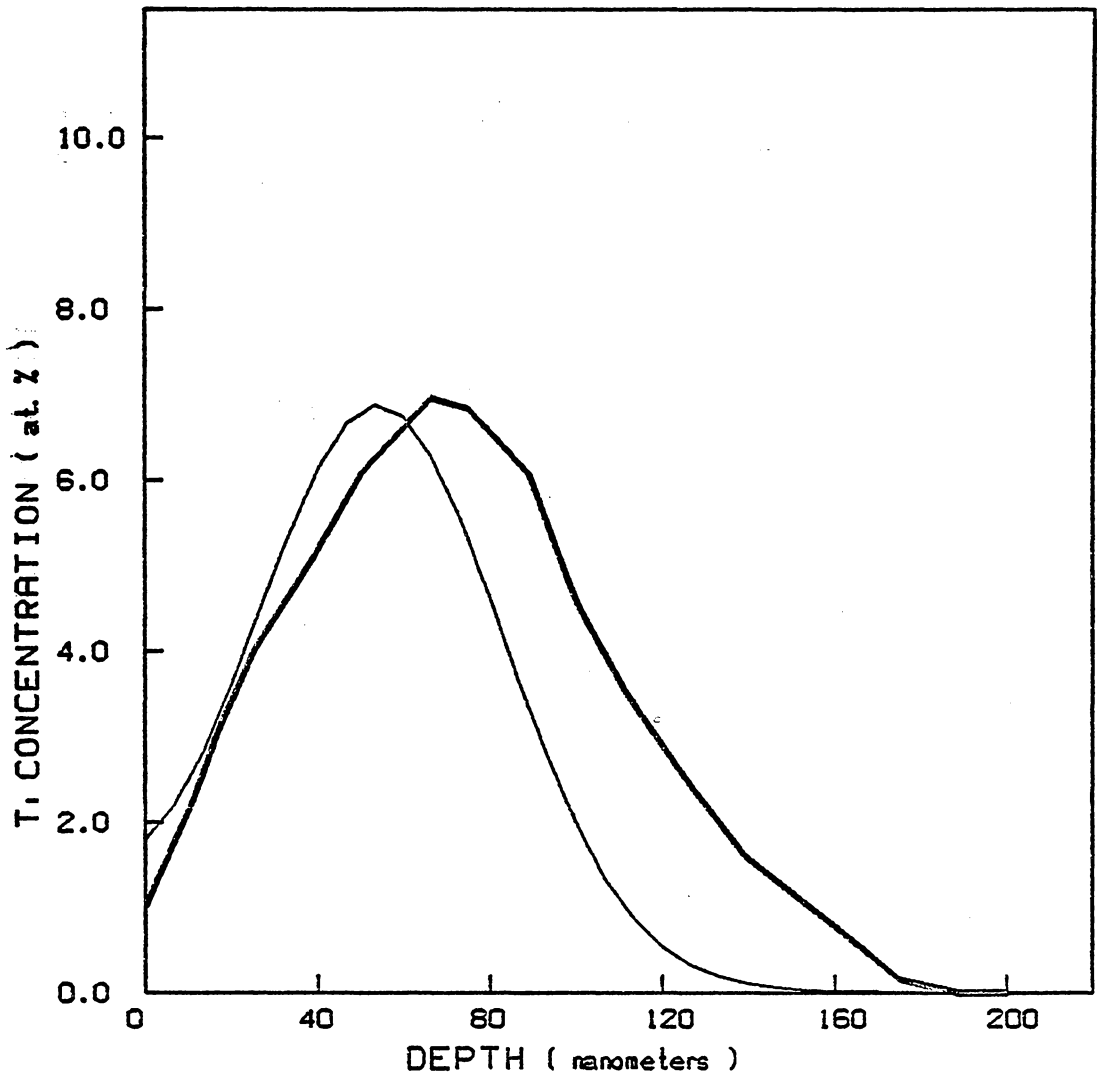

Figure 8. Experimental (heavy line) and calculated profiles (without lattice dilation) for a fluence of $5 \times 10^{16}/cm^2$ at 190 keV.

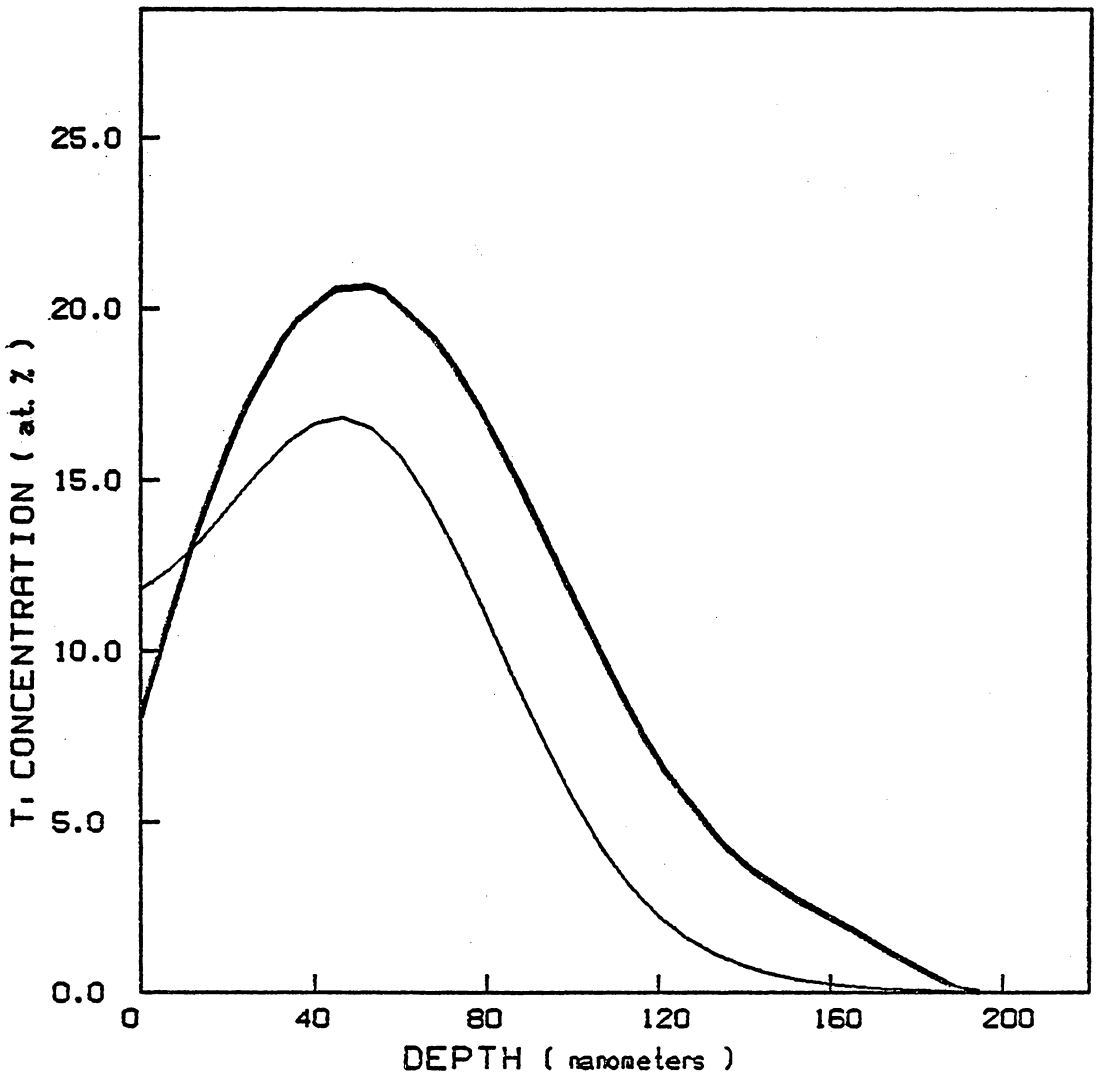

Figure 9. Experimental (heavy line) and calculated profiles (without lattice dilation) for a fluence of $16 \times 10^{16}/cm^2$ at 190 keV.

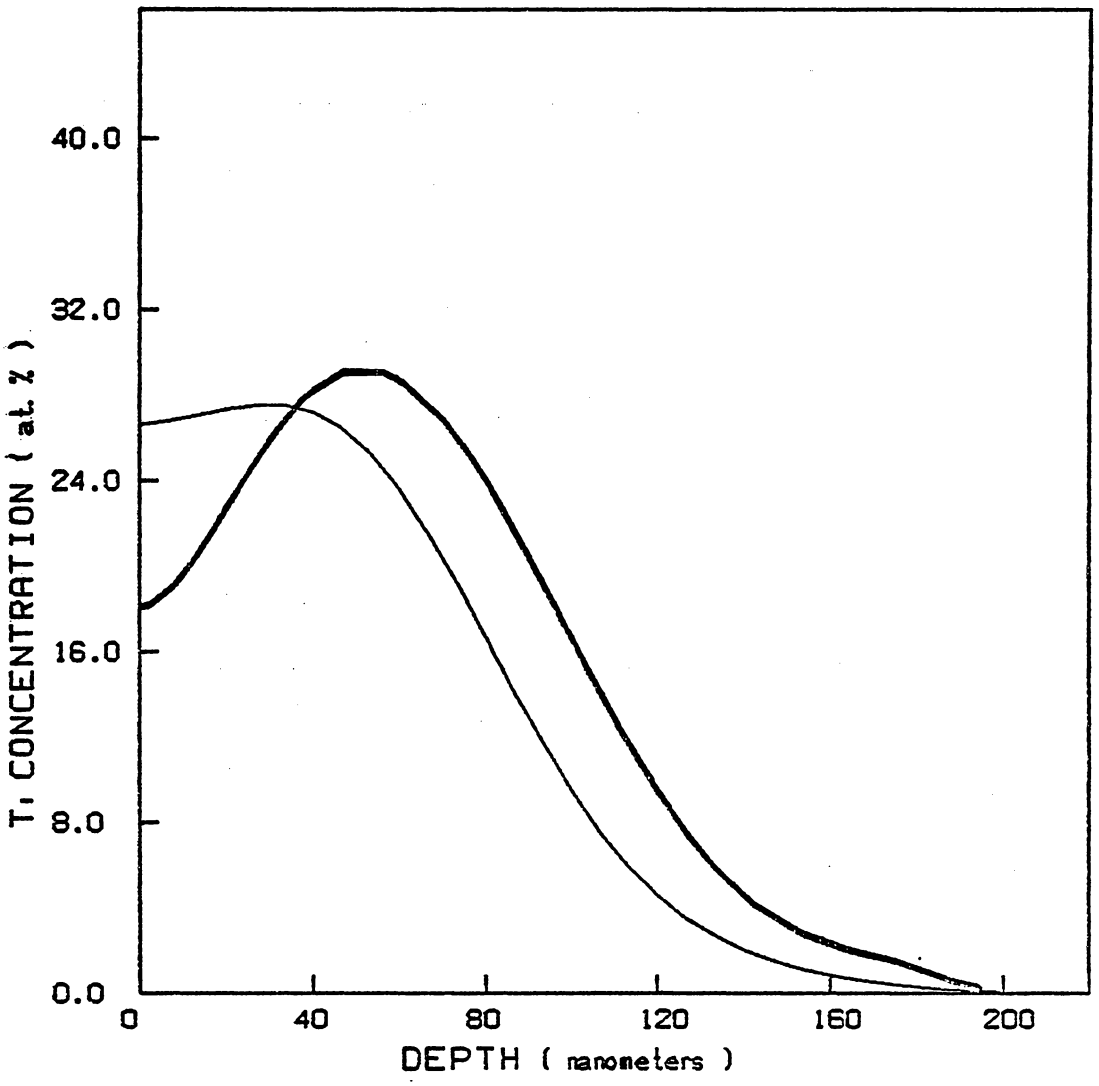

Figure 10. Experimental (heavy line) and calculated profiles (without lattice dilation) for a fluence of $40 \times 10^{16}/cm^2$ at 190 keV.

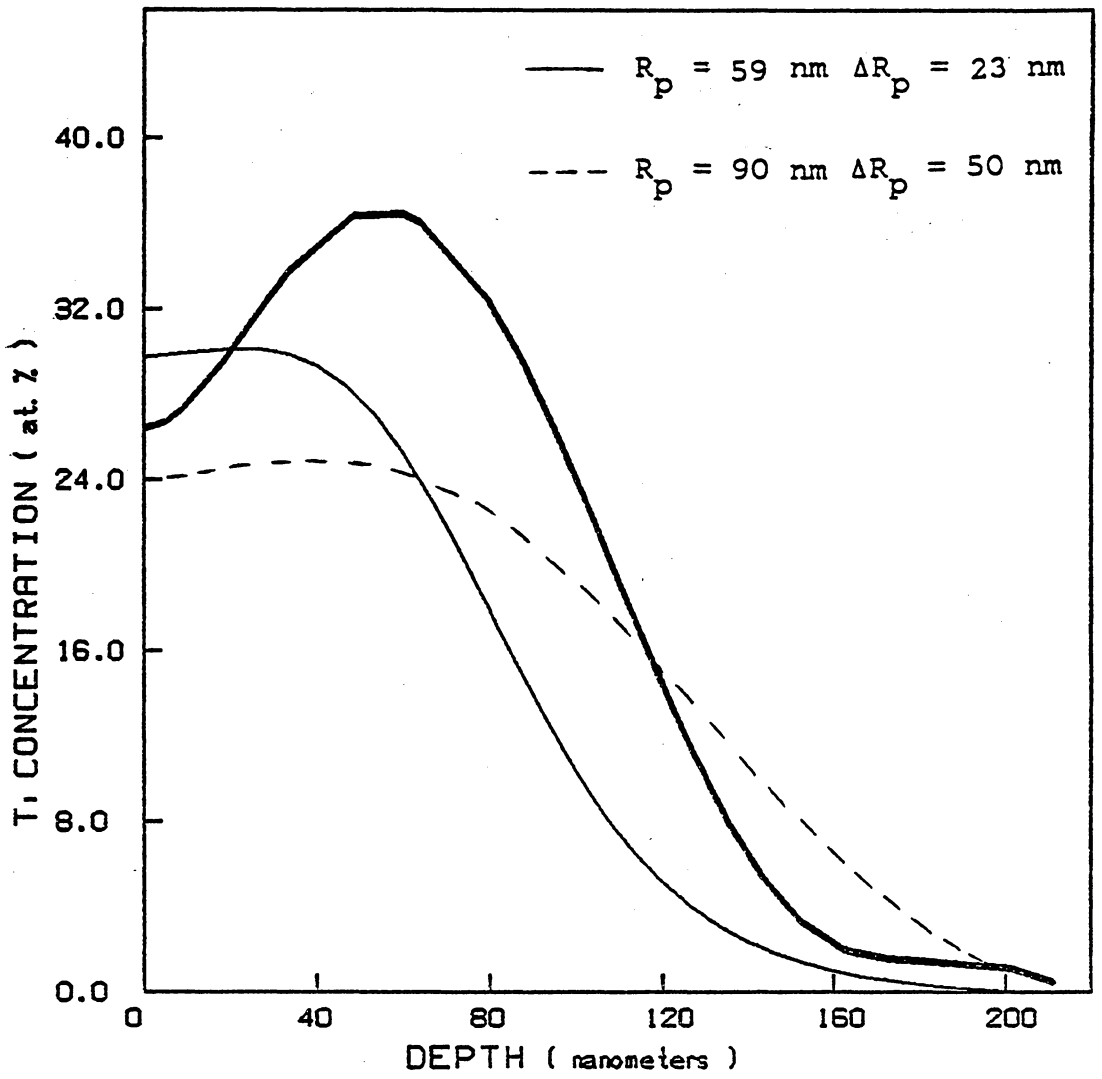

Figure 11. Experimental (heavy line) and calculated profiles (without lattice dilation) for a fluence of $50 \times 10^{16}/cm^2$ at 190 keV.

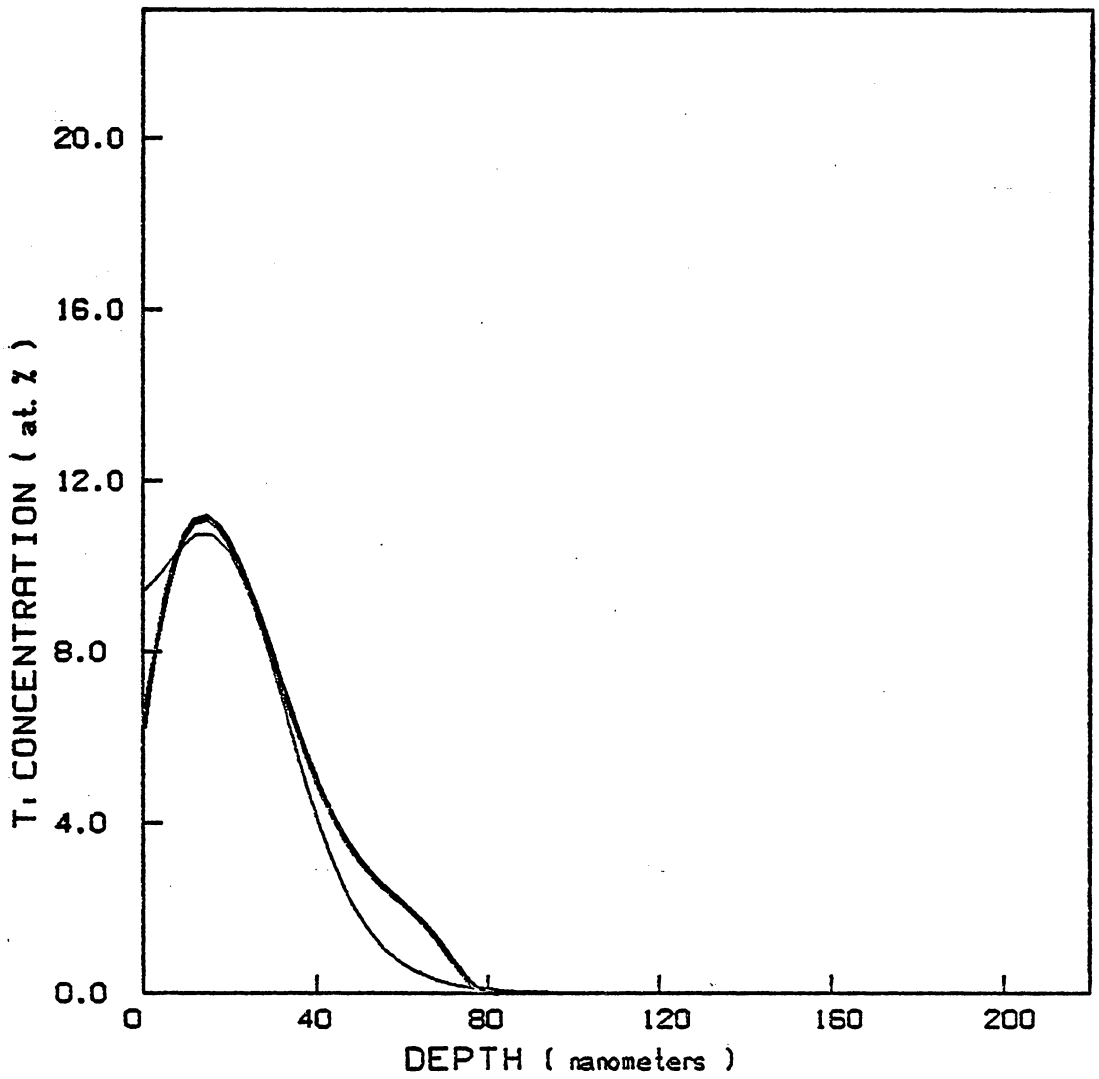

Figure 12. Experimental (heavy line) and calculated profiles (without lattice dilation) for a fluence of $5x10^{16}/cm^2$ at 55 keV.

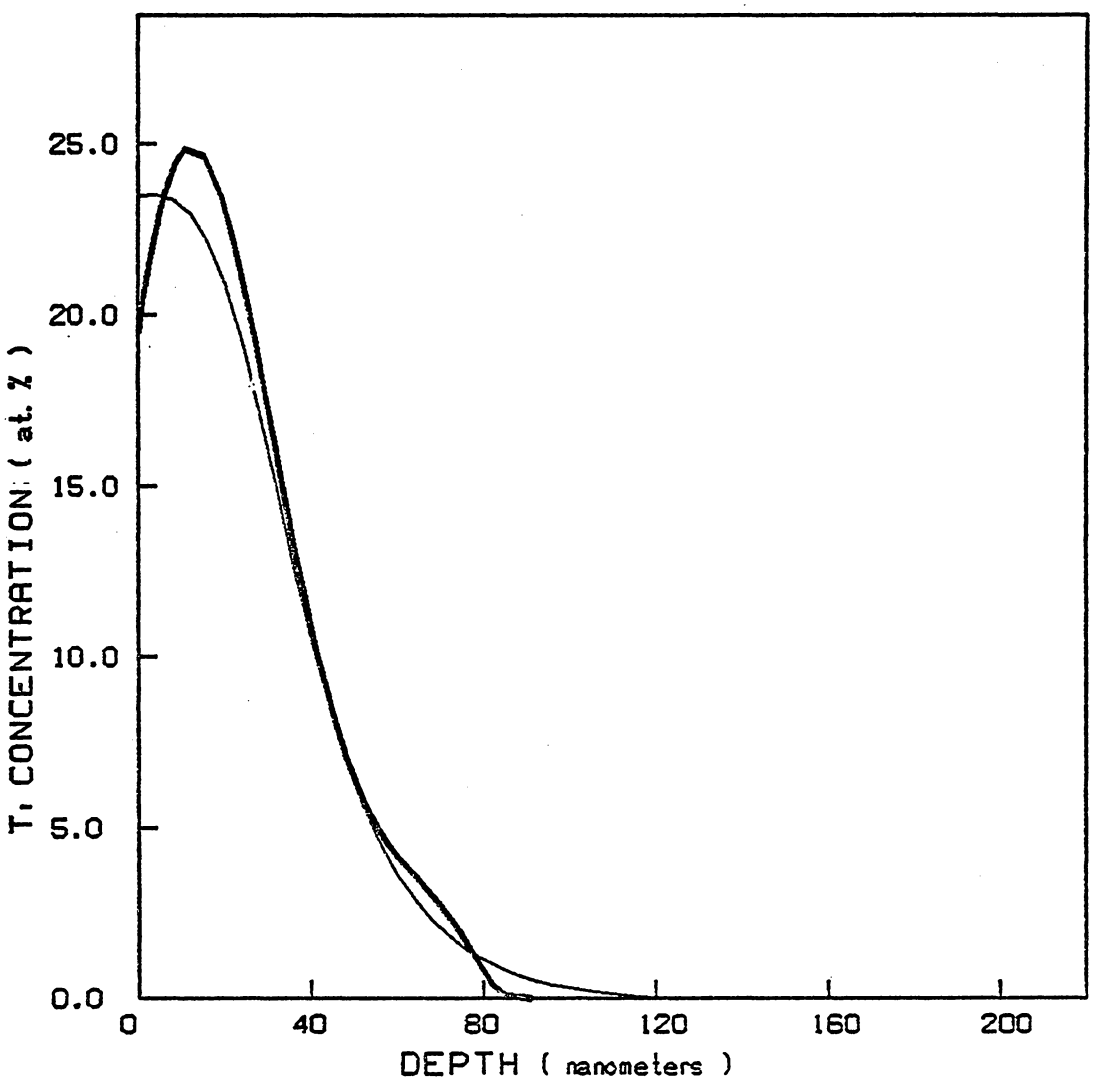

Figure 13. Experimental (heavy line) and calculated profiles (without lattice dilation) for a fluence of $16 \times 10^{16}/cm^2$ at 55 keV.

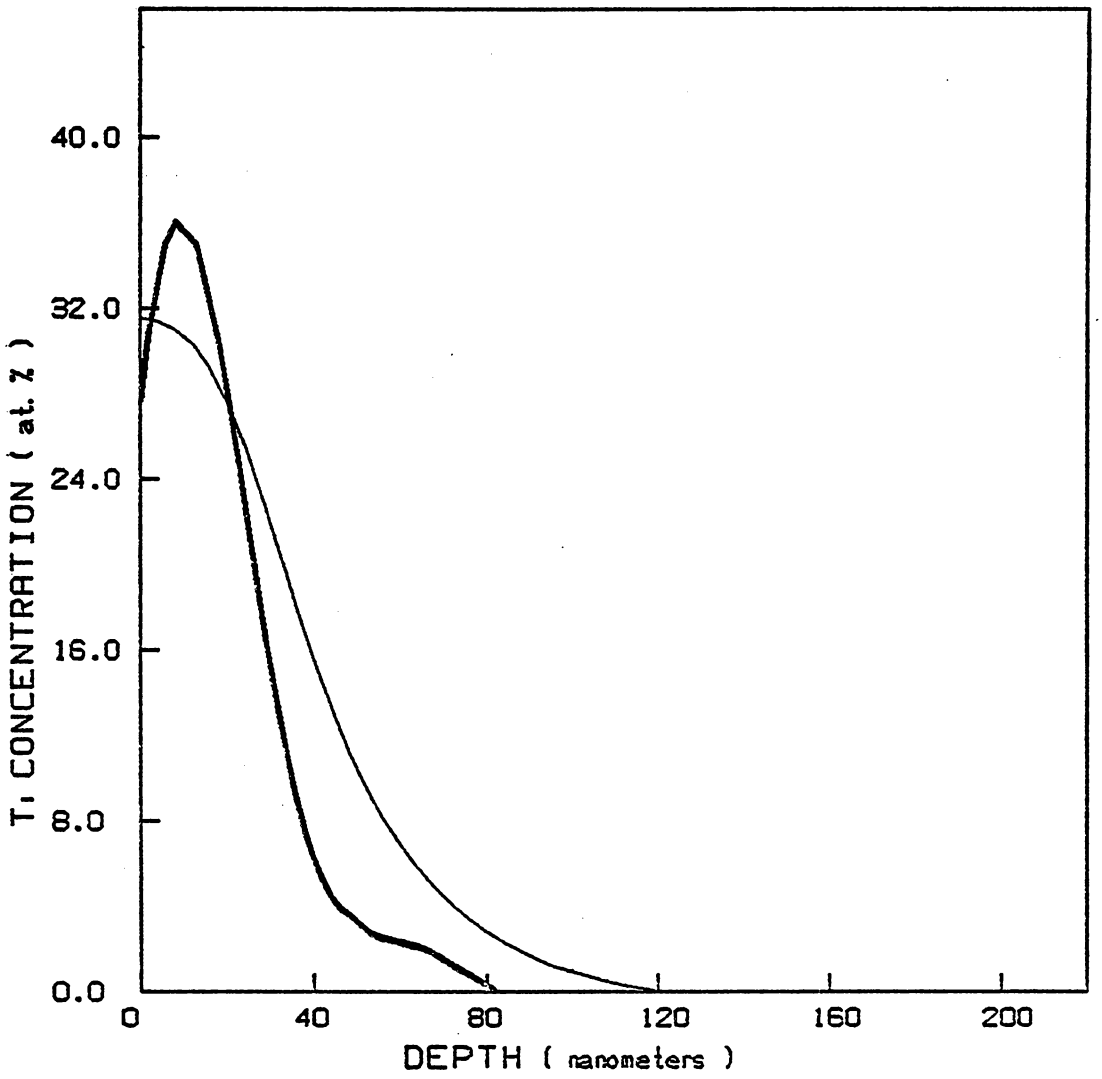

Figure 14. Experimental (heavy line) and calculated profiles (without lattice dilation) for a fluence of $40 \times 10^{16}/cm^2$ at 55 keV.

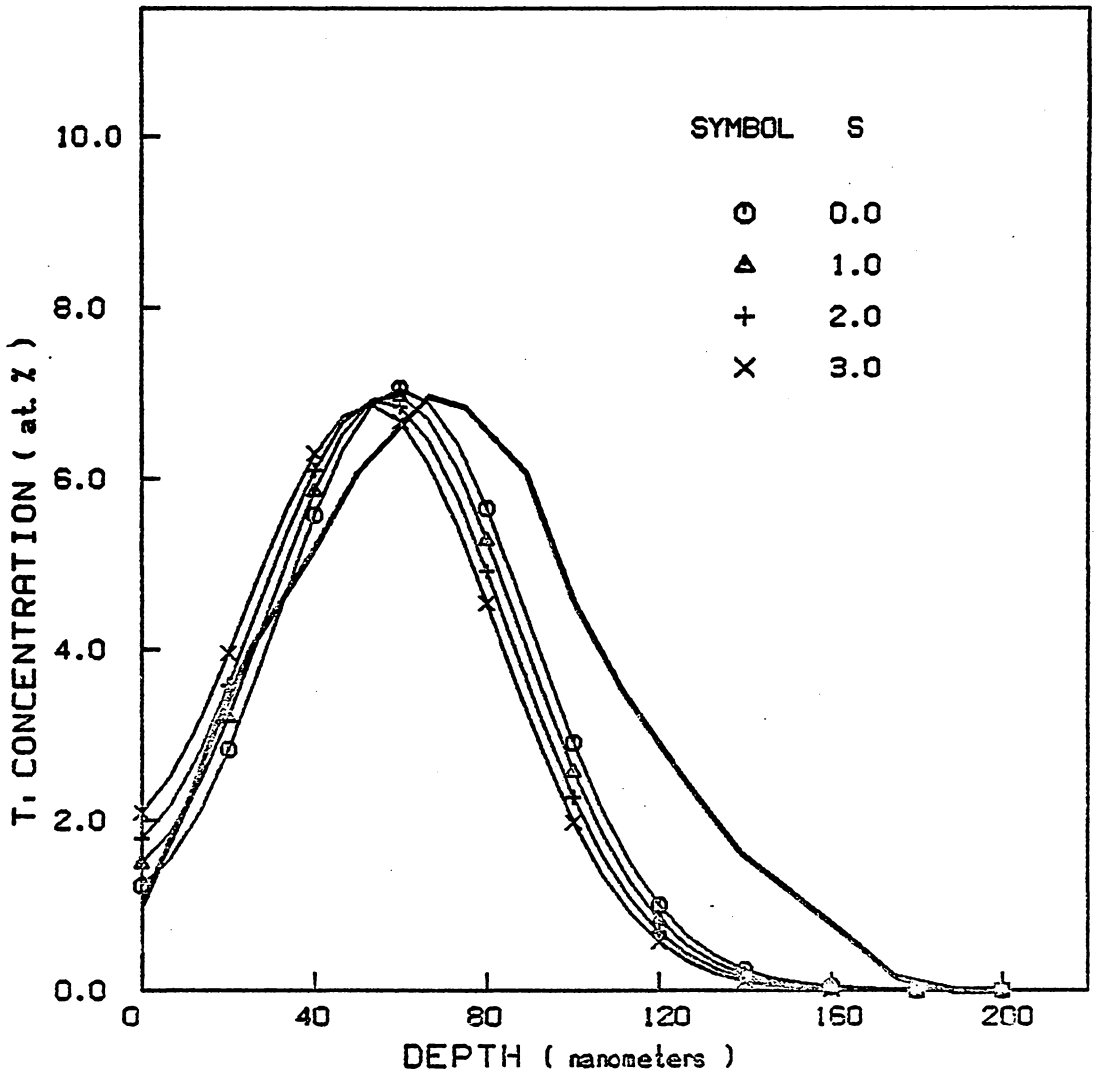

Figure 15. Experimental (heavy line) and calculated profiles (for various sputtering yields) for a fluence of $5x10^{16}/cm^2$ at 190 keV.

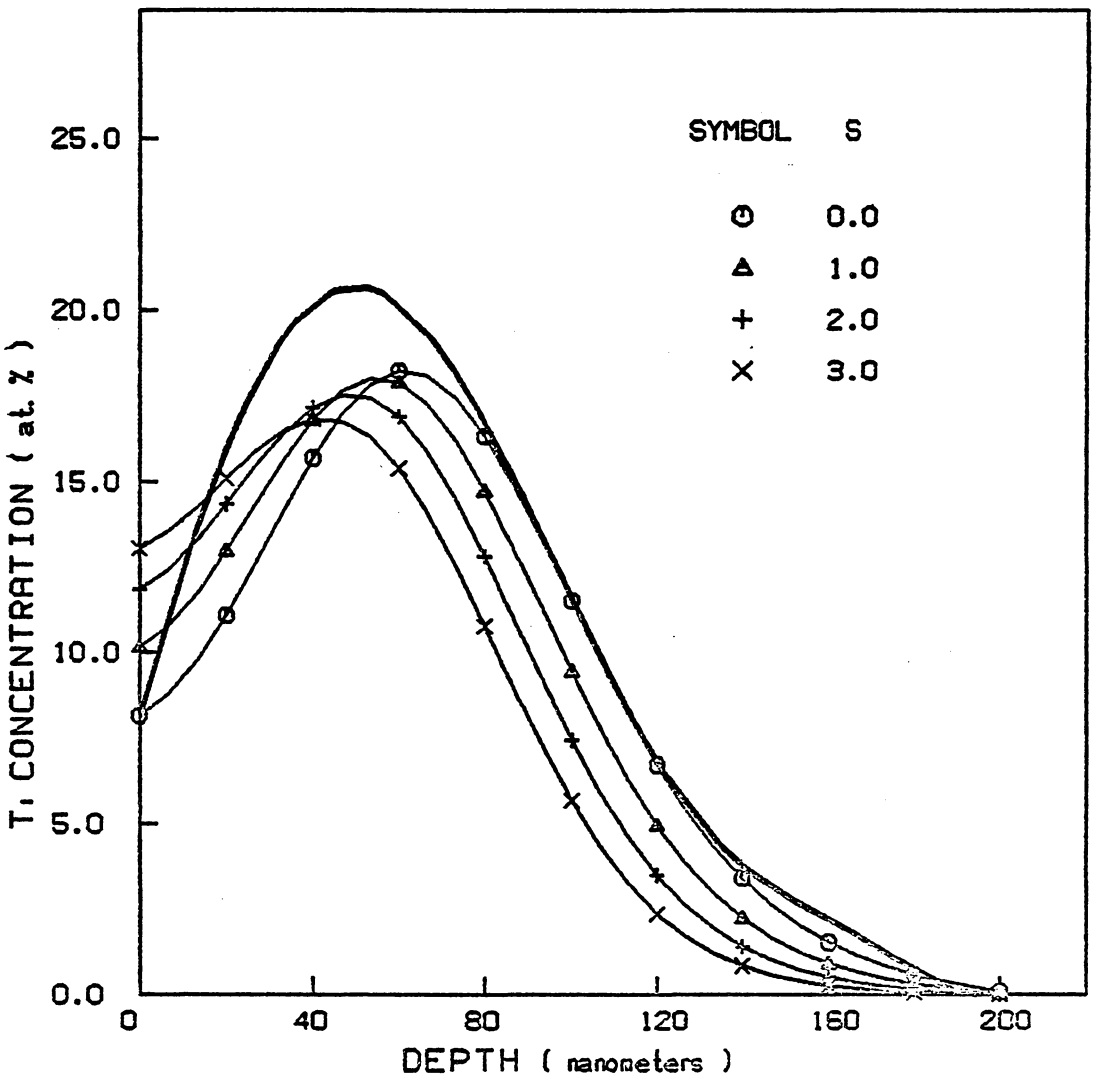

Figure 16. Experimental (heavy line) and calculated profiles (for various sputtering yields) for a fluence of $16 \times 10^{16}/cm^2$ at 190 keV.

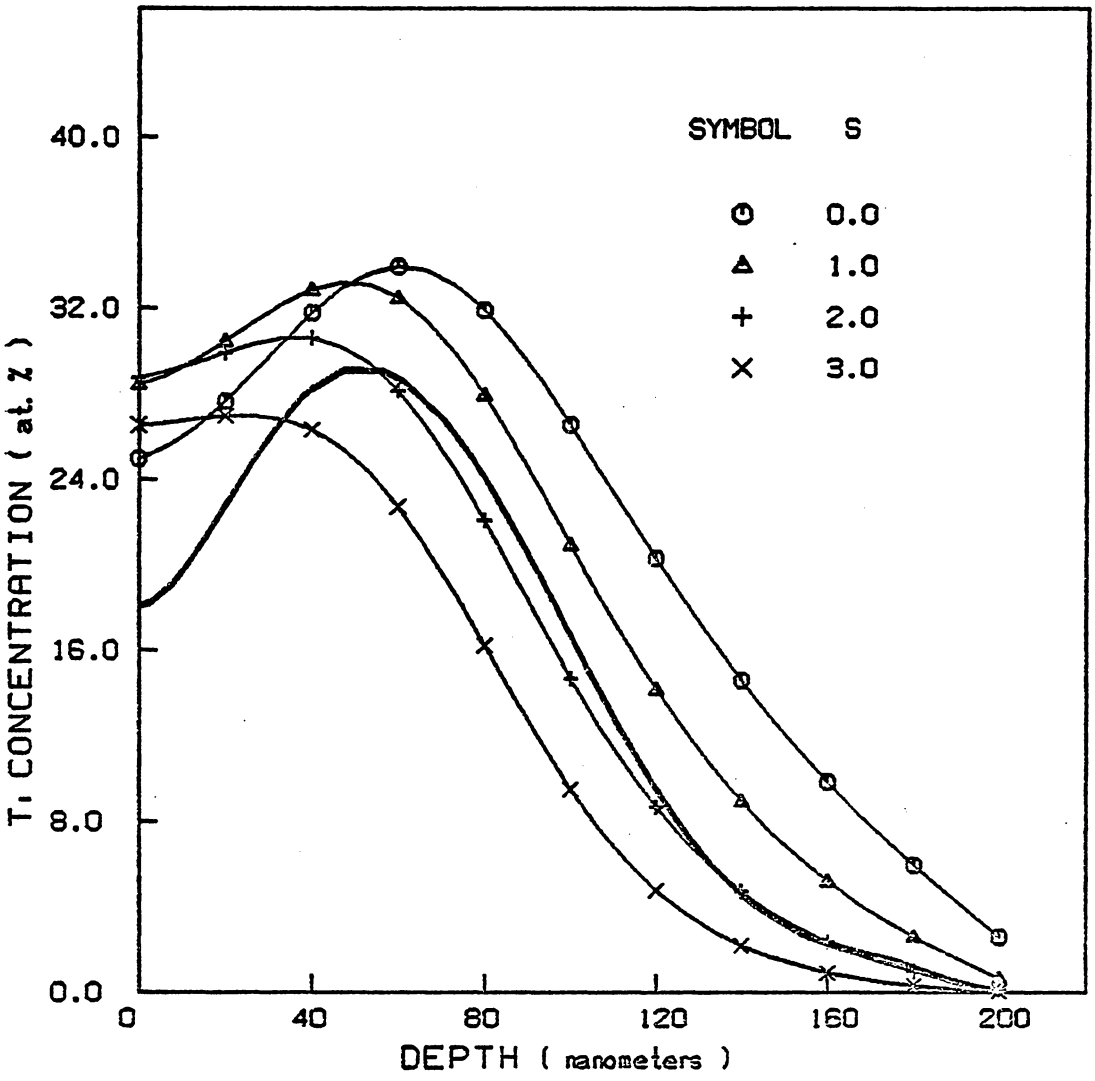

Figure 17. Experimental (heavy line) and calculated profiles (for various sputtering yields) for a fluence of $40 \times 10^{16}/cm^2$ at 190 keV.

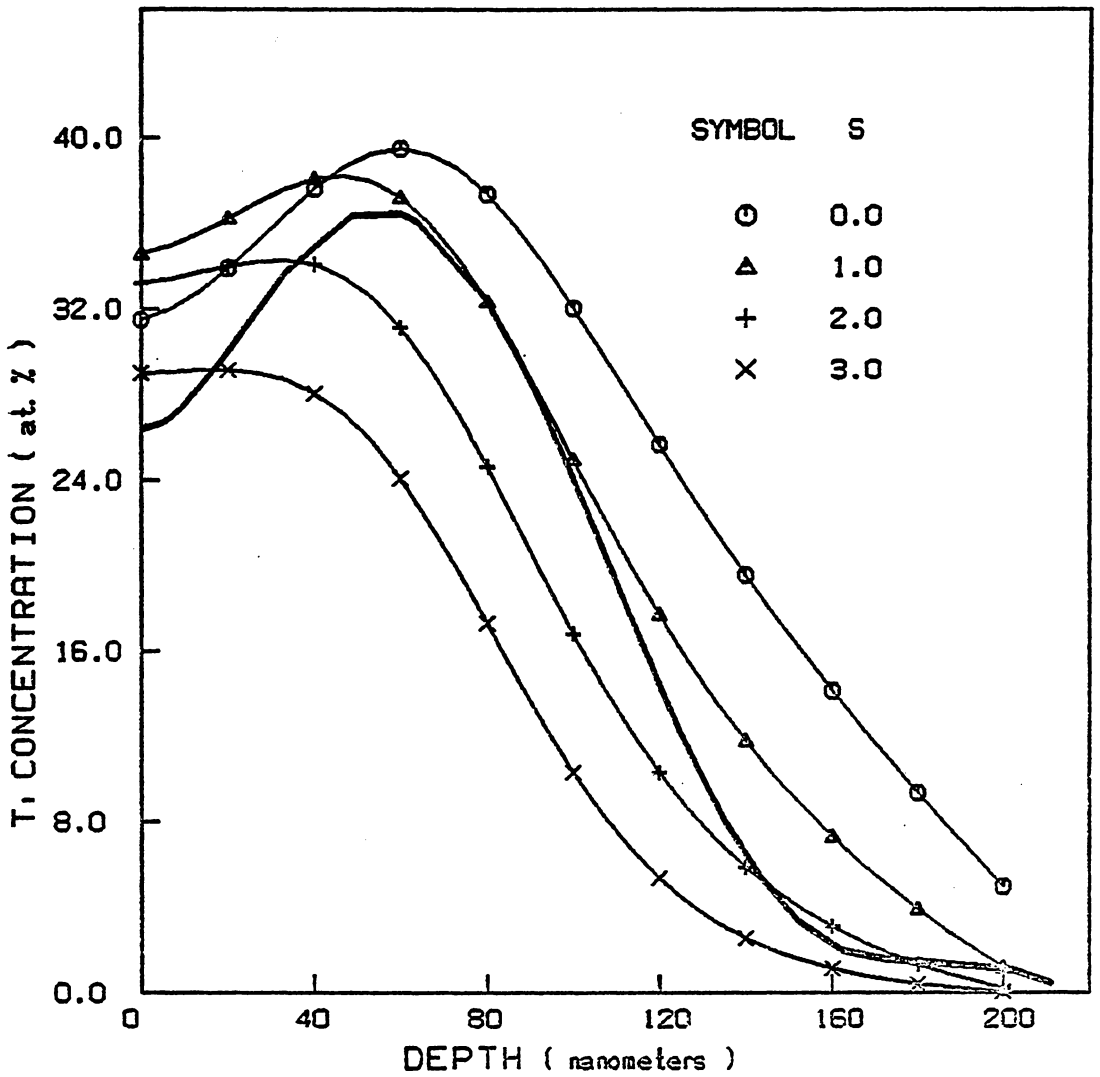

Figure 18. Experimental (heavy line) and calculated profiles (for various sputtering yields) for a fluence of $50 \times 10^{16}/cm^2$ at 190 keV.

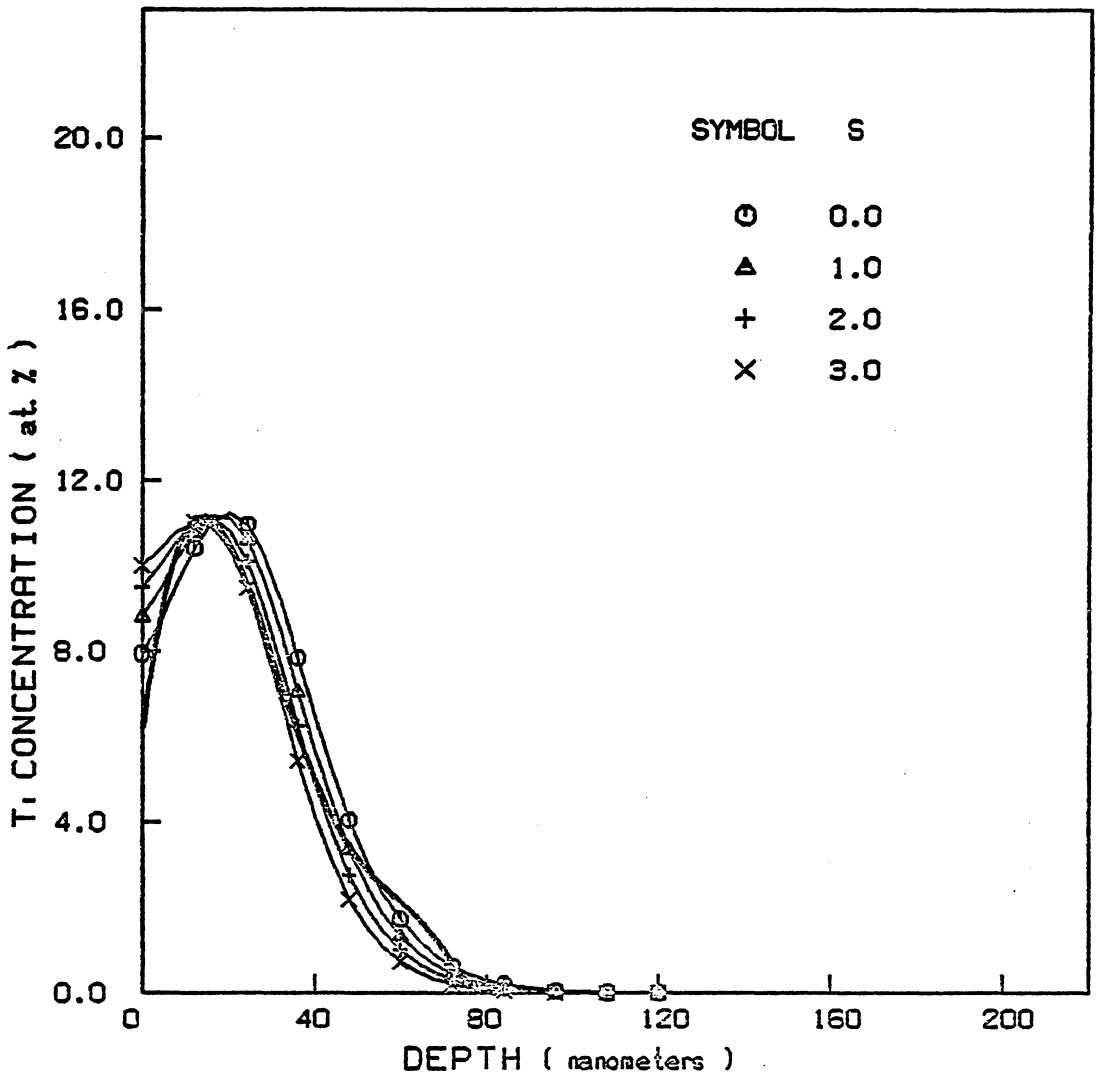

Figure 19. Experimental (heavy line) and calculated profiles (for various sputtering yields) for a fluence of $5x10^{16}/cm^2$ at 55 keV.

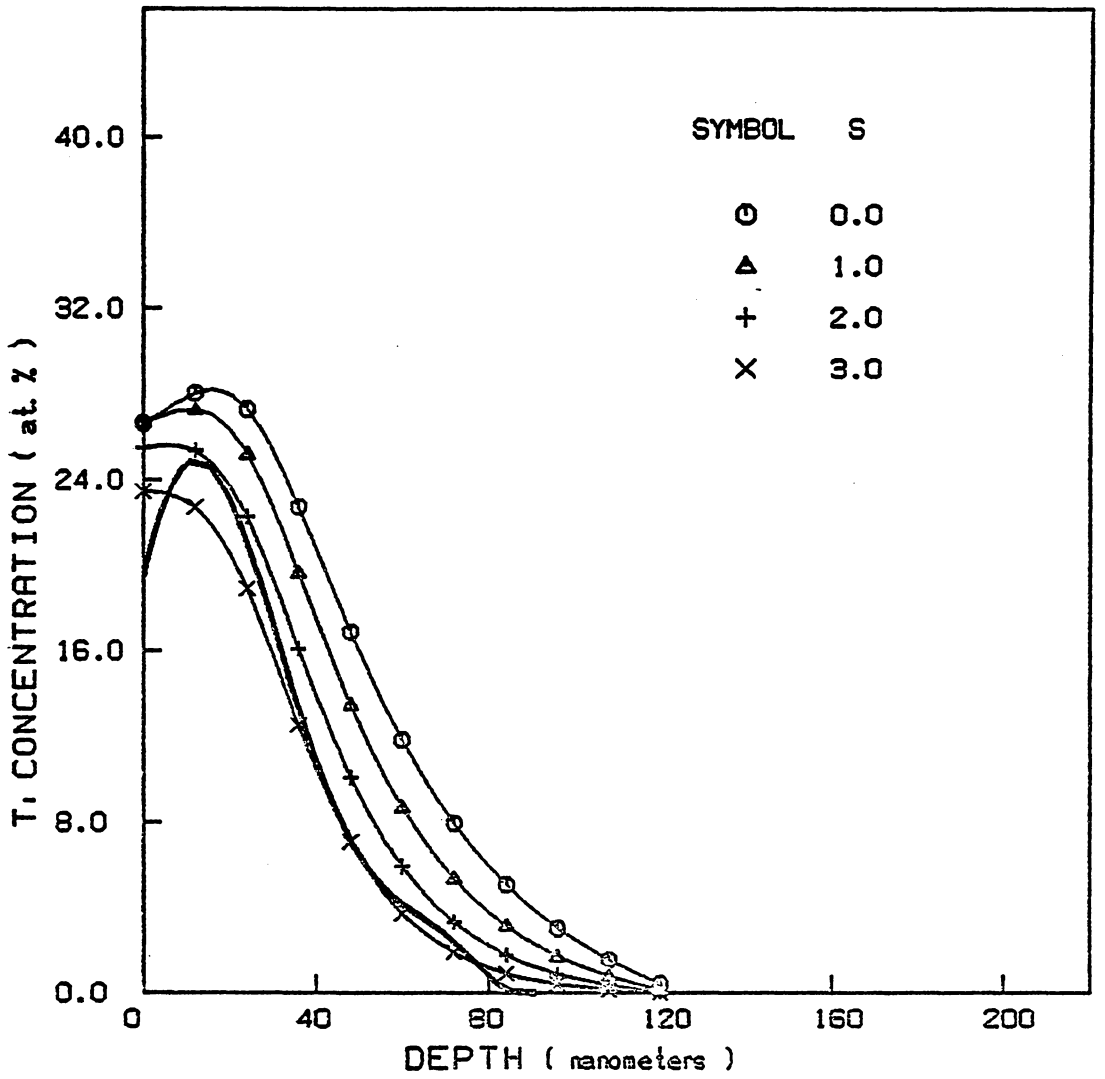

Figure 20. Experimental (heavy line) and calculated profiles (for various sputtering yields) for a fluence of $16 \times 10^{16}/cm^2$ at 55 keV.

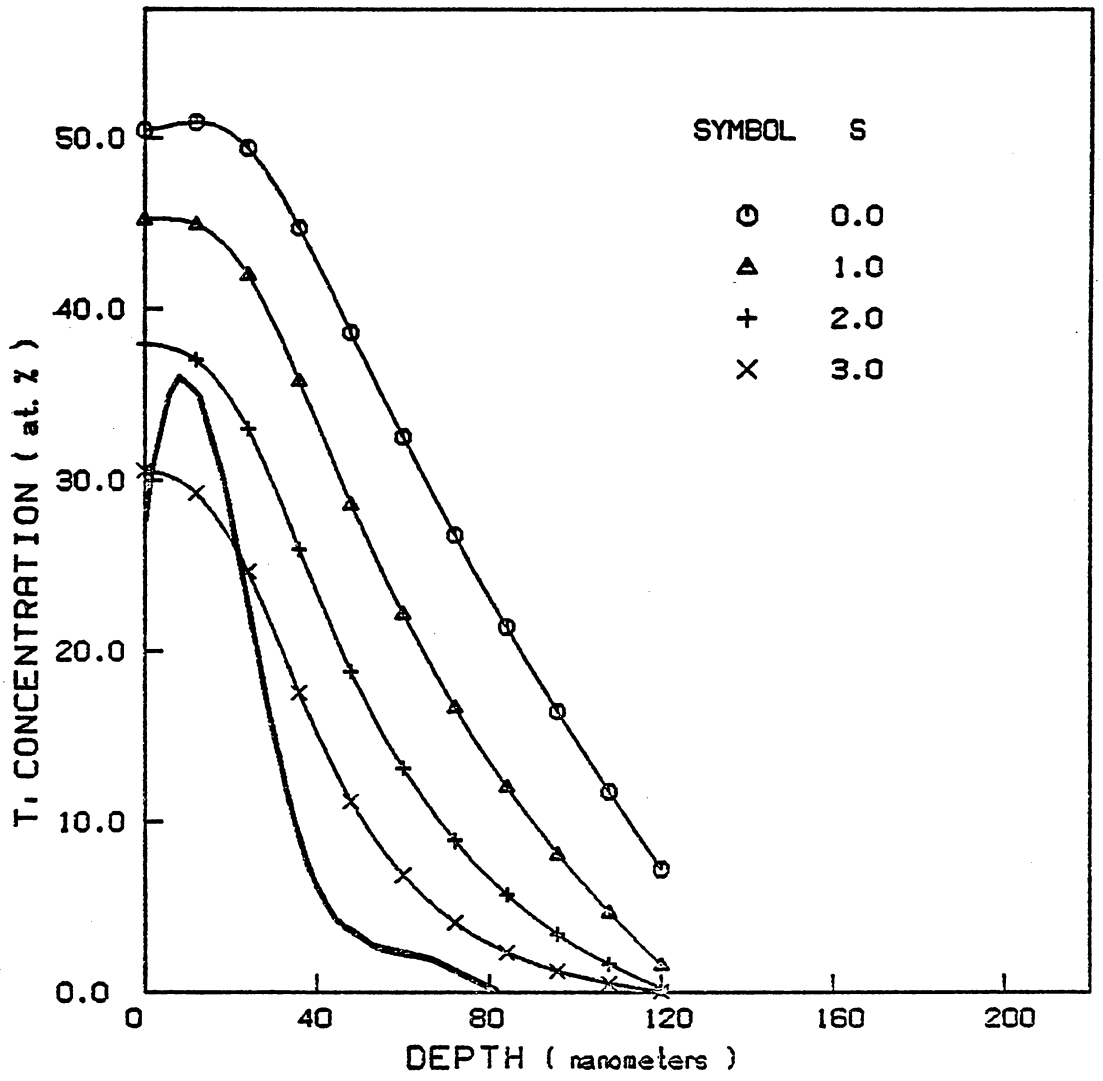

Figure 21. Experimental (heavy line) and calculated profiles (for various sputtering yields) for a fluence of $40 \times 10^{16}/cm^2$ at 55 keV.

imental data. The results of Figs. 15-21 were calculated for a Ti effective diffusivity of $6x10^{-15}cm^2/sec$.

Ti Diffusivity Effect:

The sensitivity of the calculated profiles to the value of D_{Ti} is shown in Figs. 22-28. These figures show calculations done for a sputtering yield of 2. These results include the ones obtained in the absence of diffusion broadening, showing that the experimental data are consistently broader. A value of D_{Ti} different from zero results in better agreement with experiment. An order of magnitude estimate of the transport process present can be obtained from these figures and it is approximately $D_{Ti} = 6x10^{-15}cm^2/sec$.

C Diffusivity Effect:

Figs. 29-35 show the calculated carbon concentration profiles compared to experiment. In these figures calculations are presented for different values of D_C. For the lower fluences the value $D_C = 6x10^{-15}cm^2/sec$ gives good agreement with the measured profiles. At higher fluences the agreement is not good because there appears to be a saturation of carbon at the surface. At high fluences the as-

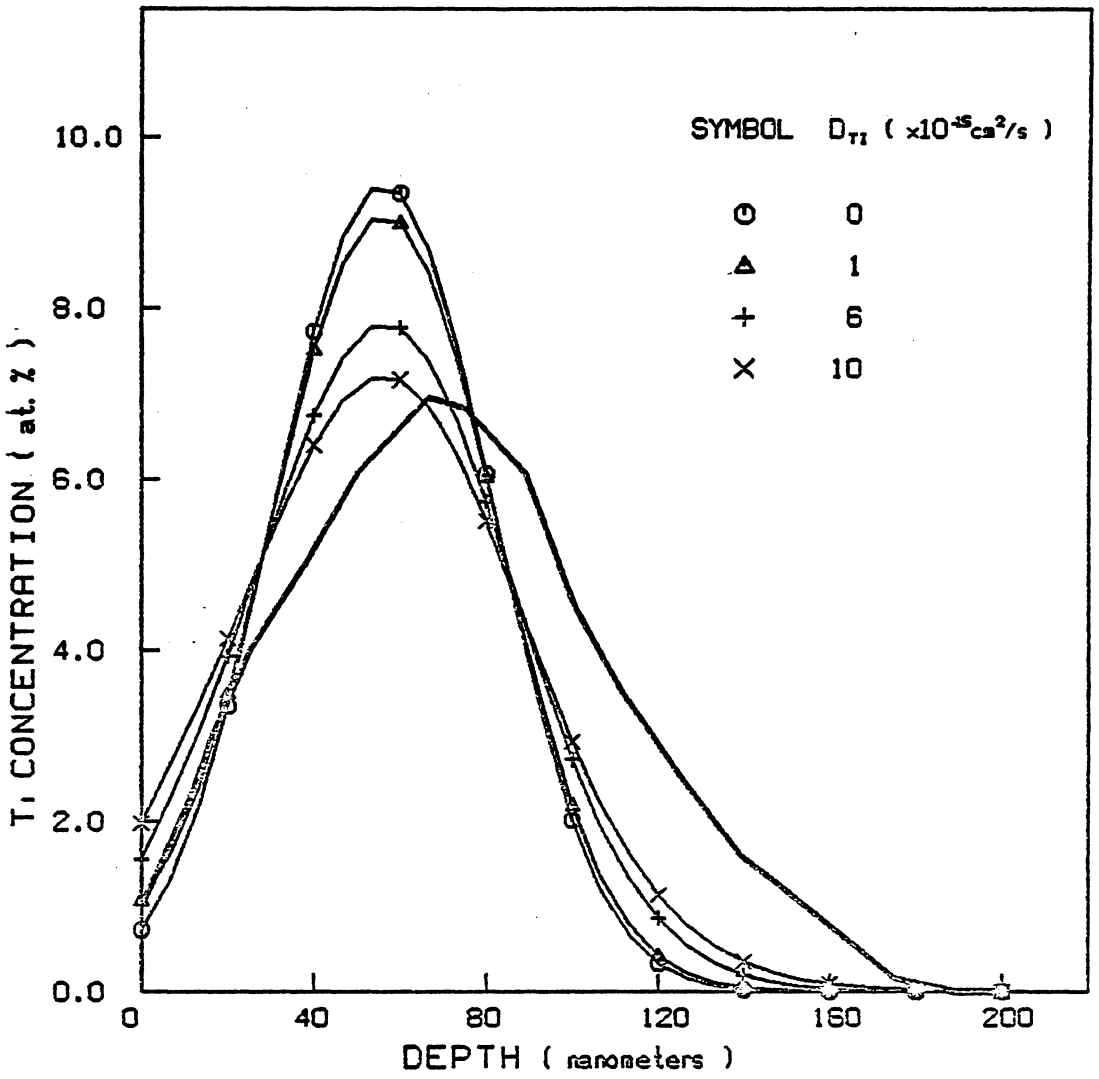

Figure 22. Experimental (heavy line) and calculated profiles (for various Ti diffusivities) for a fluence of $5 \times 10^{16}/cm^2$ at 190 keV.

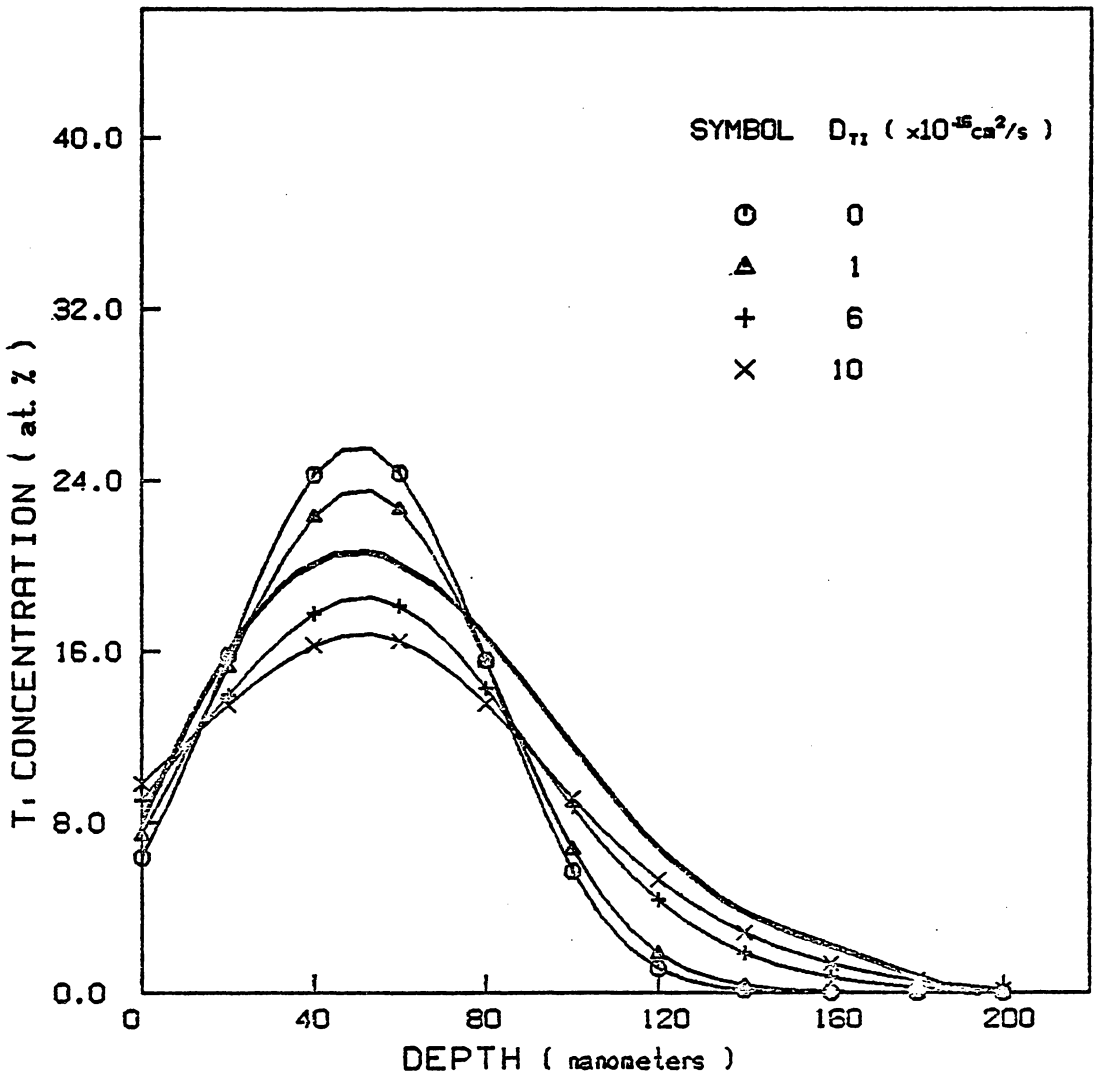

Figure 23. Experimental (heavy line) and calculated profiles (for various Ti diffusivities) for a fluence of $16 \times 10^{16}/cm^2$ at 190 keV.

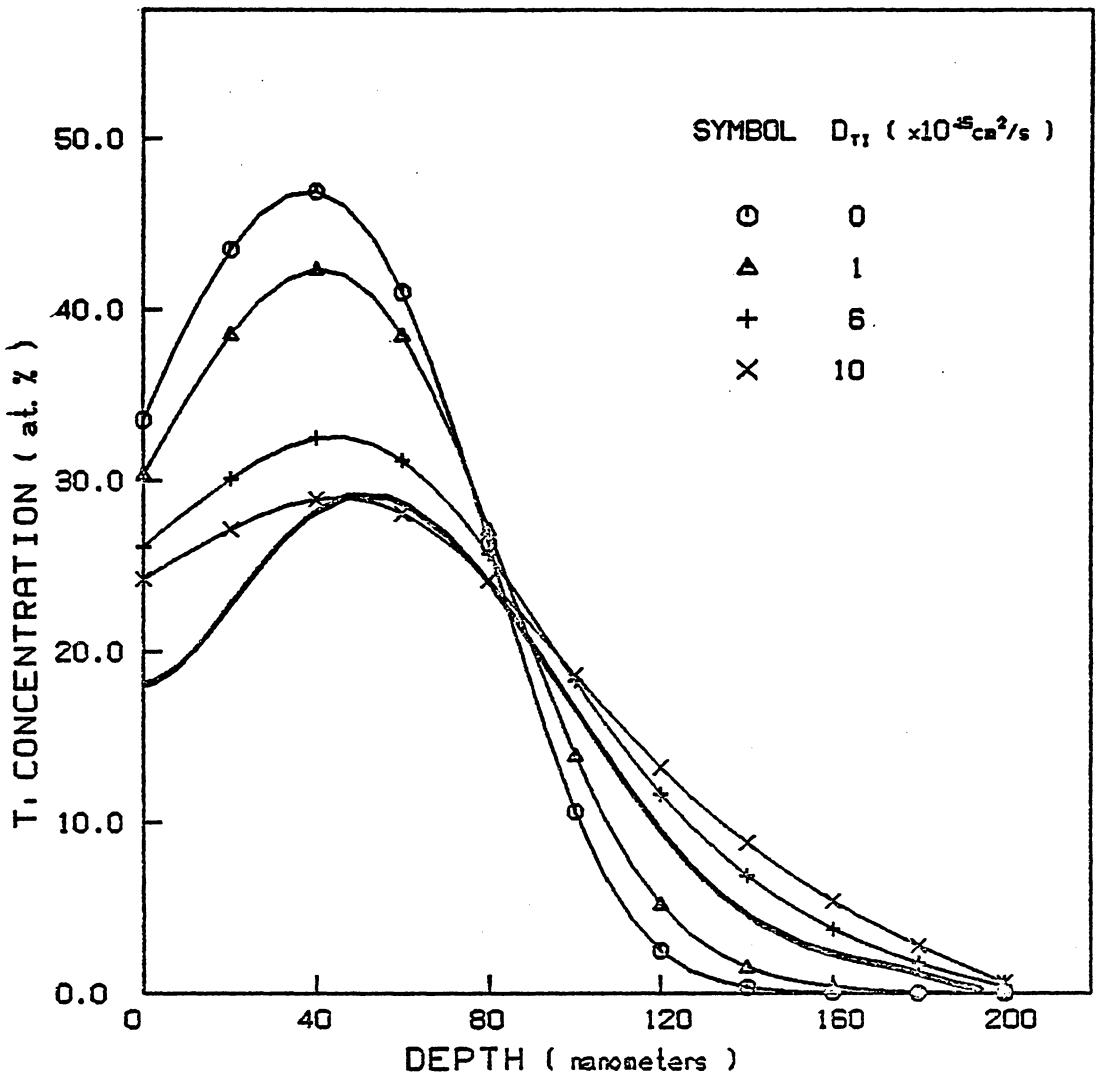

Figure 24. Experimental (heavy line) and calculated profiles (for various Ti diffusivities) for a fluence of $40 \times 10^{16}/cm^2$ at 190 keV.

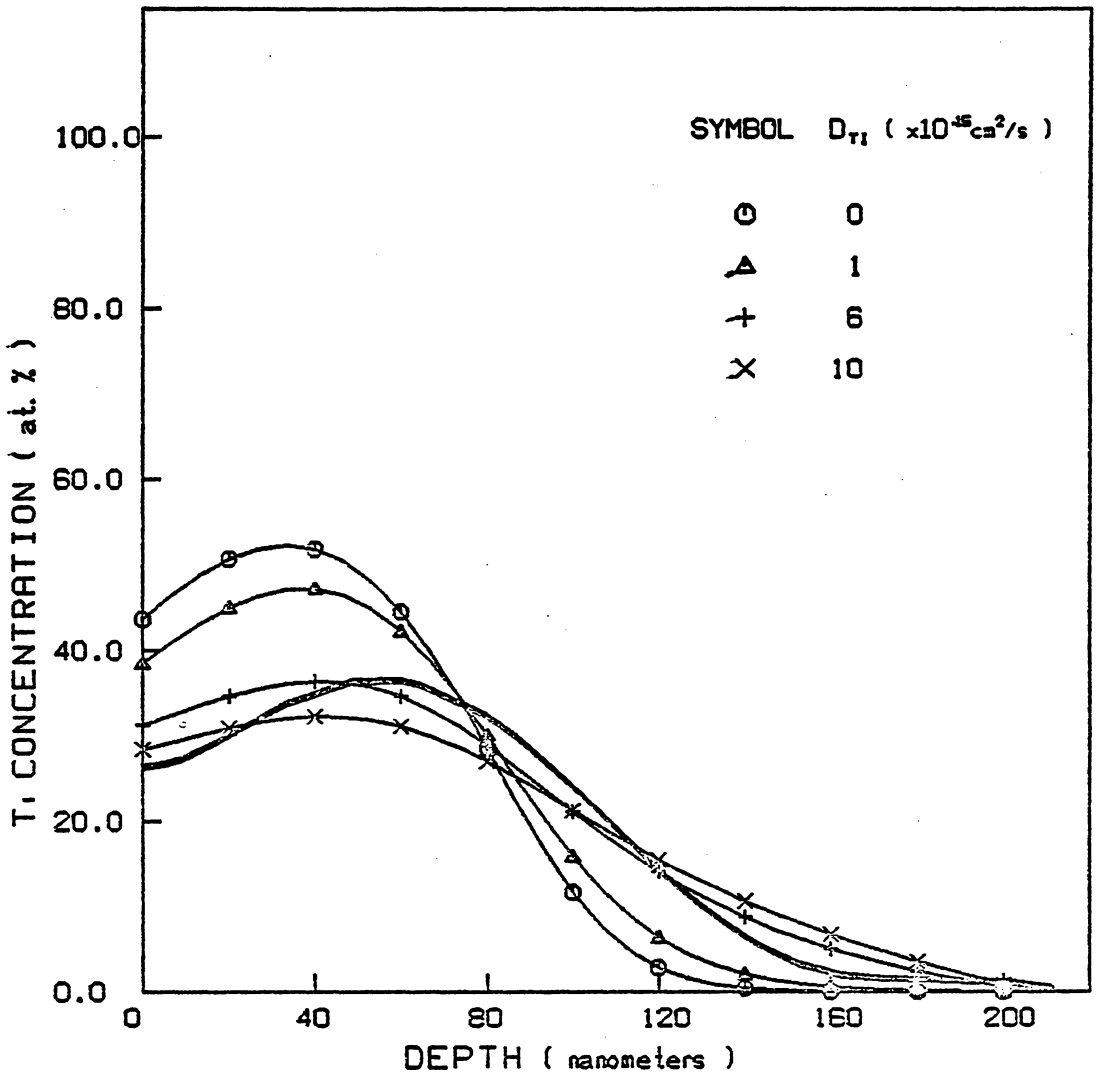

Figure 25. Experimental (heavy line) and calculated profiles (for various Ti diffusivities) for a fluence of $50 \times 10^{16}/cm^2$ at 190 keV.

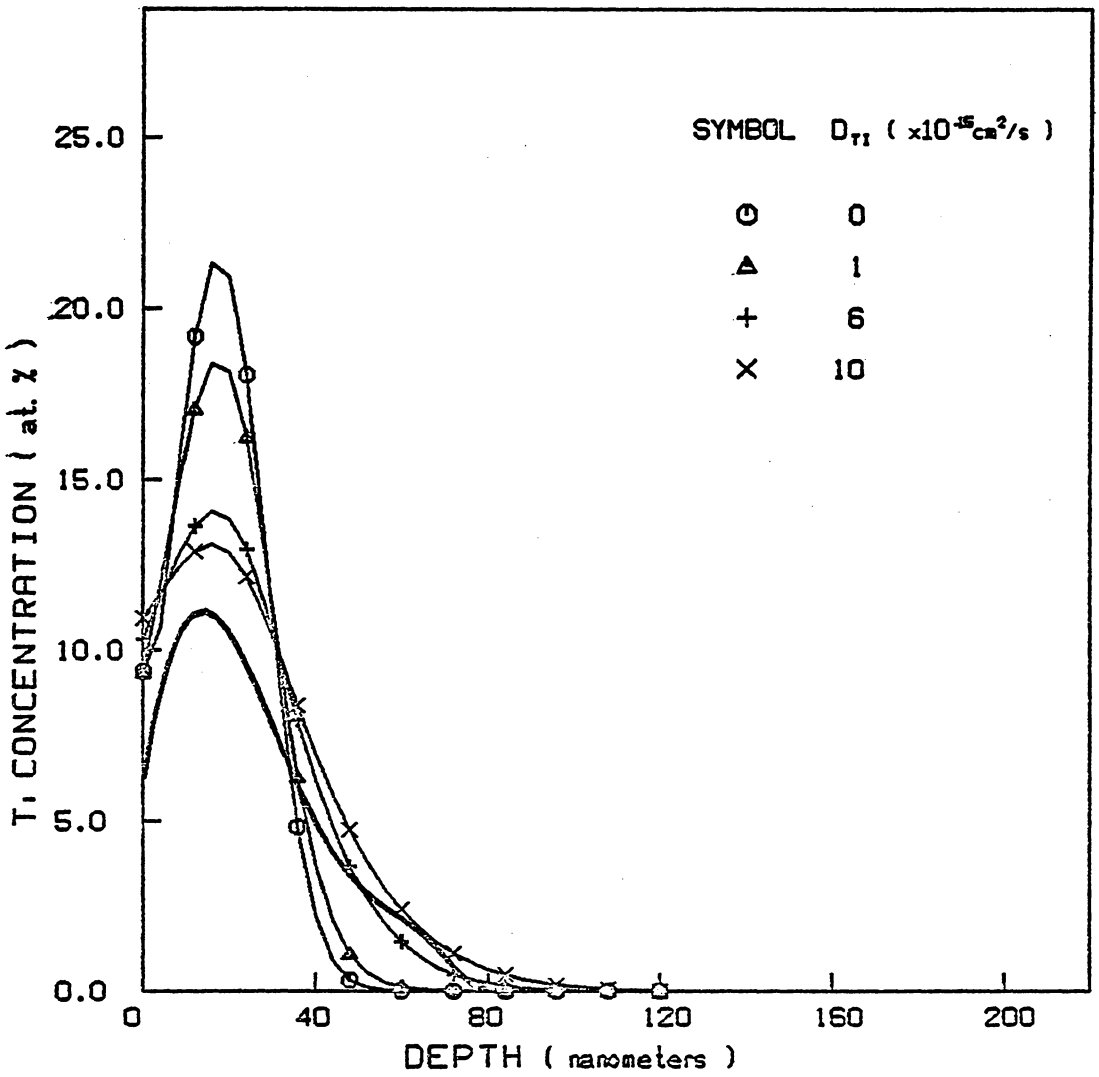

Figure 26. Experimental (heavy line) and calculated profiles (for various Ti diffusivities) for a fluence of $5x10^{16}/cm^2$ at 55 keV.

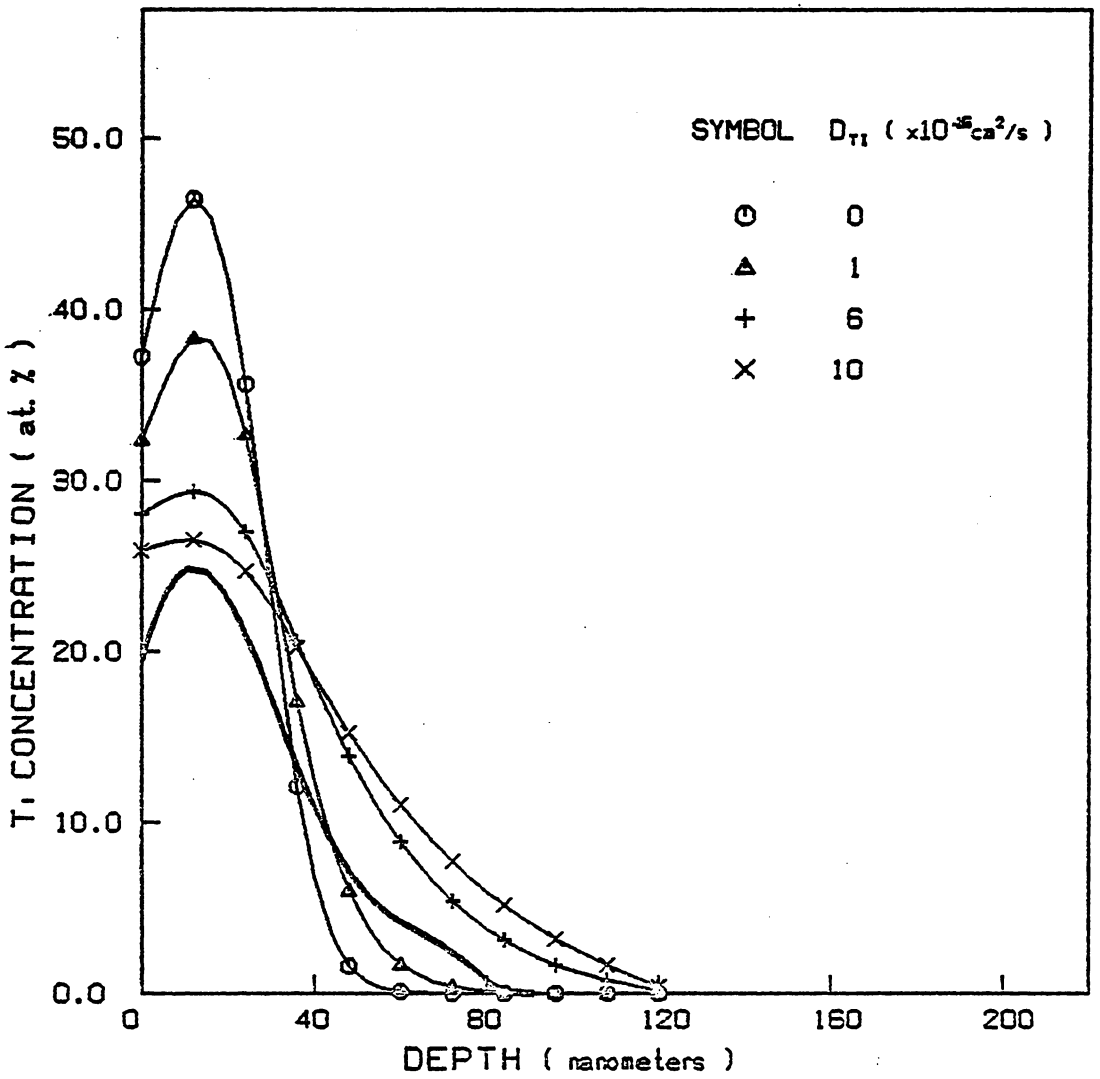

Figure 27. Experimental (heavy line) and calculated profiles (for various Ti diffusivities) for a fluence of $16 \times 10^{16}/cm^2$ at 55 keV.

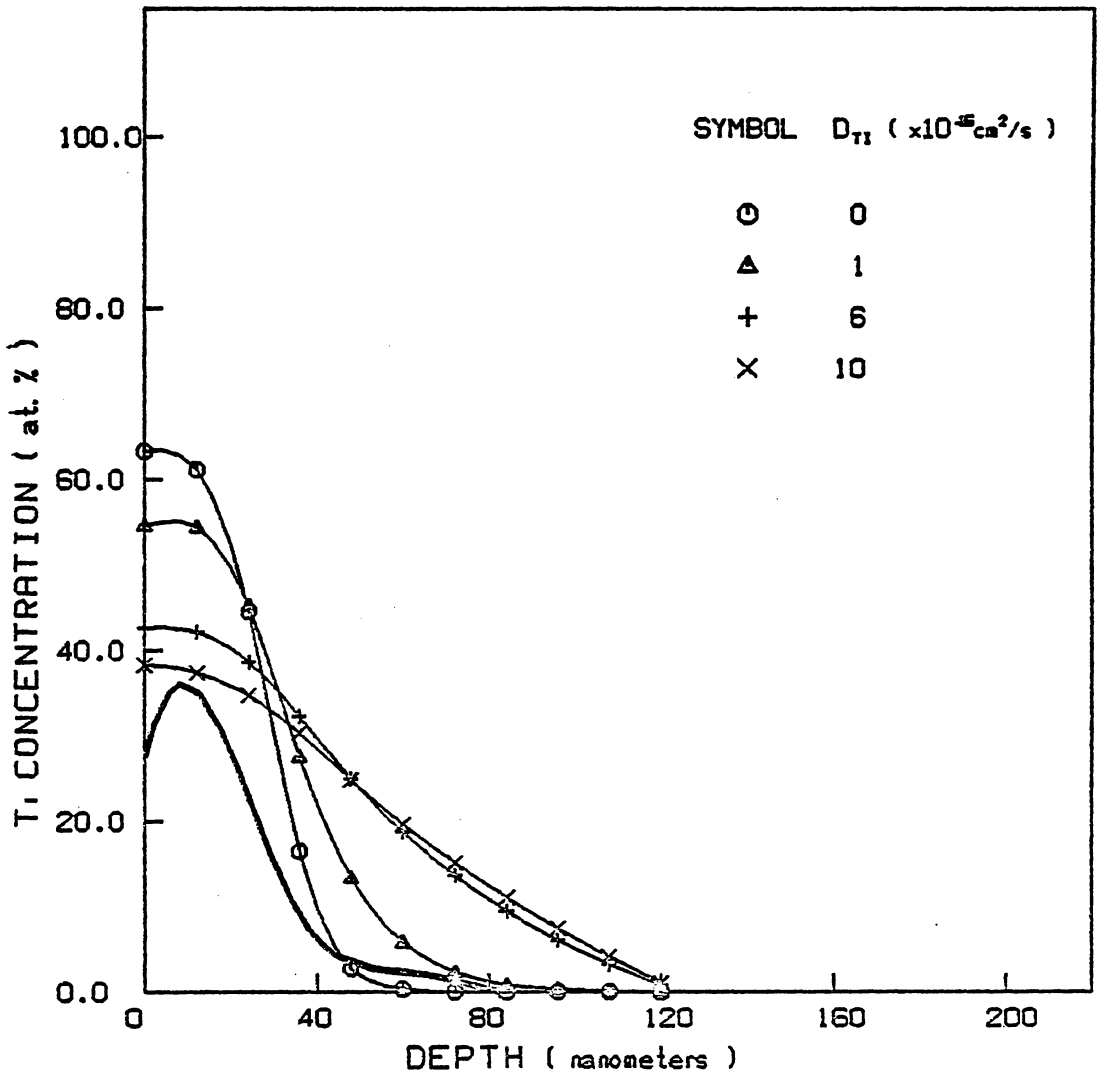

Figure 28. Experimental (heavy line) and calculated profiles (for various Ti diffusivities) for a fluence of $40 \times 10^{16}/cm^2$ at 55 keV.

sumption used in the calculations that every Ti adsorbs a carbon is probably no longer valid. Figs. 36-42 show the results of calculations in which $[C]^s$ is restricted to 16 at%. The results are better than the ones without the saturation limit. It should also be noted that these calculations assume a sputtering yield of 2.0, which as discussed above seems to be too high for the high fluences. As an order of magnitude estimate it may be concluded that the value of the effective diffusivity of carbon is around $D_C = 6x10^{-15} cm^2/sec$.

To facilitate clearer observation of the sensitivity of the profiles to the fitted parameters, corresponding figures are grouped together in Figs. 43-47, for six of the seven experimental profiles studied. (The profile for the lowest fluence of $5x10^{16}/cm^2$ at 190 keV was found to be insensitive to the variation of the parameters of interest and is hence omitted.) Fig. 43 shows calculated and experimental [Ti]-versus-depth profiles for three fluences at each of two energies for different sputtering yields. Figs. 44 and 45 show the sensitivity of the calculated profiles to the value of D_{Ti} for sputtering yields of 1.5 and 2 respectively. Figs. 46 and 47 show the calculated carbon profiles for the two cases, without and with surface saturation respectively.

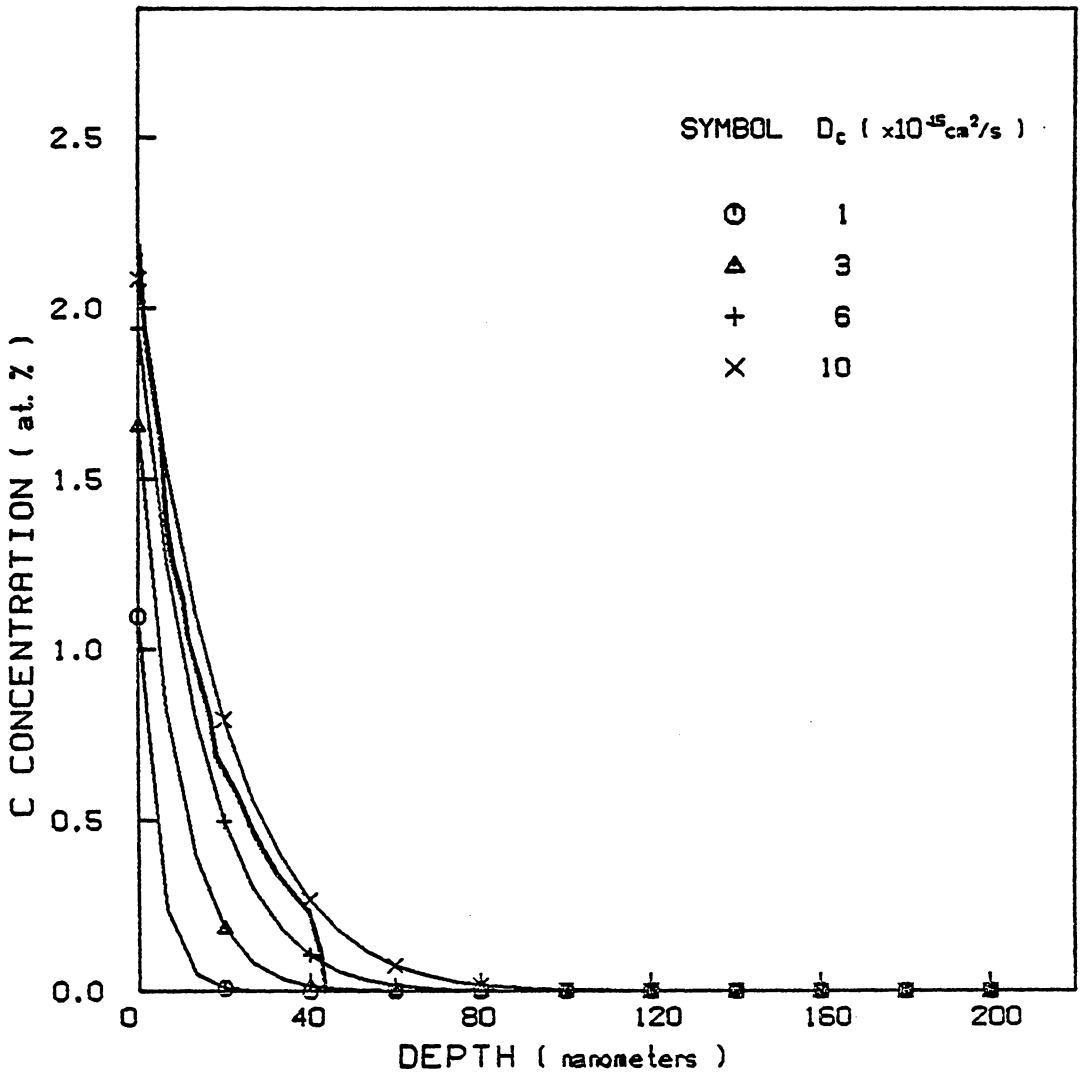

Figure 29. Experimental (heavy line) and calculated profiles (for various C diffusivities) for a fluence of $5x10^{16}/cm^2$ at 190 keV (without saturation of carbon at surface).

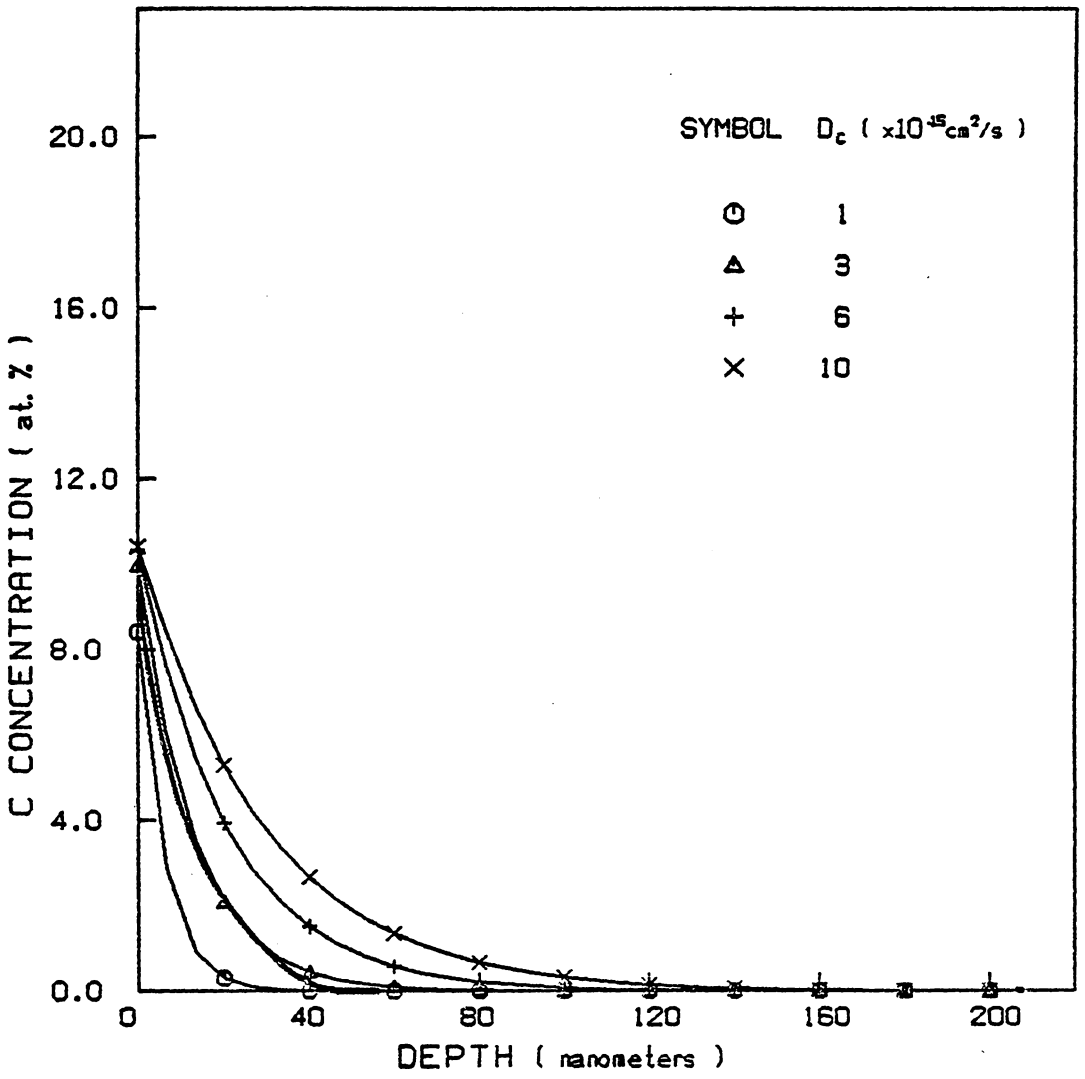

Figure 30. Experimental (heavy line) and calculated profiles (for various C diffusivities) for a fluence of $16 \times 10^{16}/cm^2$ at 190 keV (without saturation of carbon at surface).

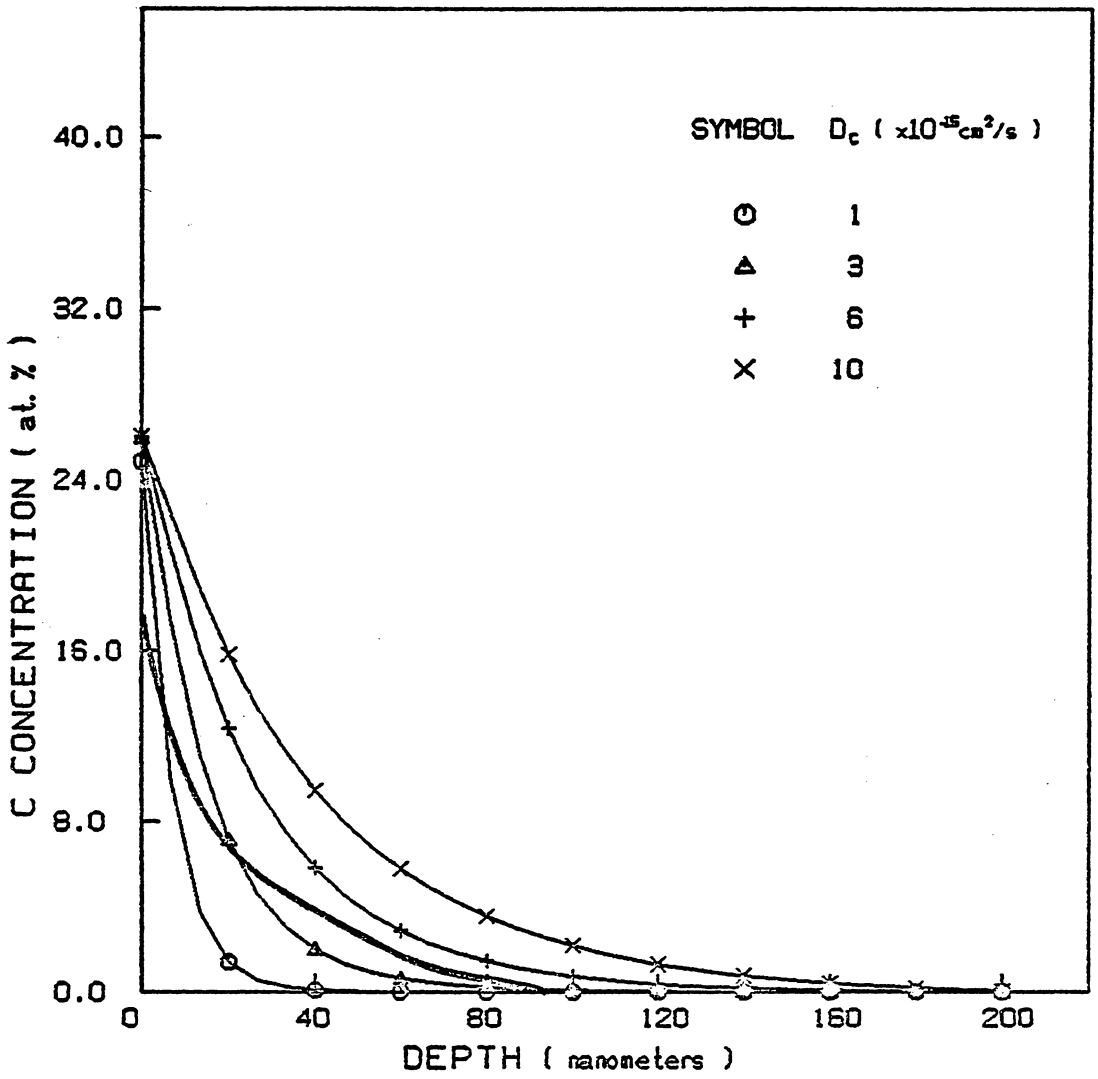

Figure 31. Experimental (heavy line) and calculated profiles (for various C diffusivities) for a fluence of $40x10^{16}/cm^2$ at 190 keV (without saturation of carbon at surface).

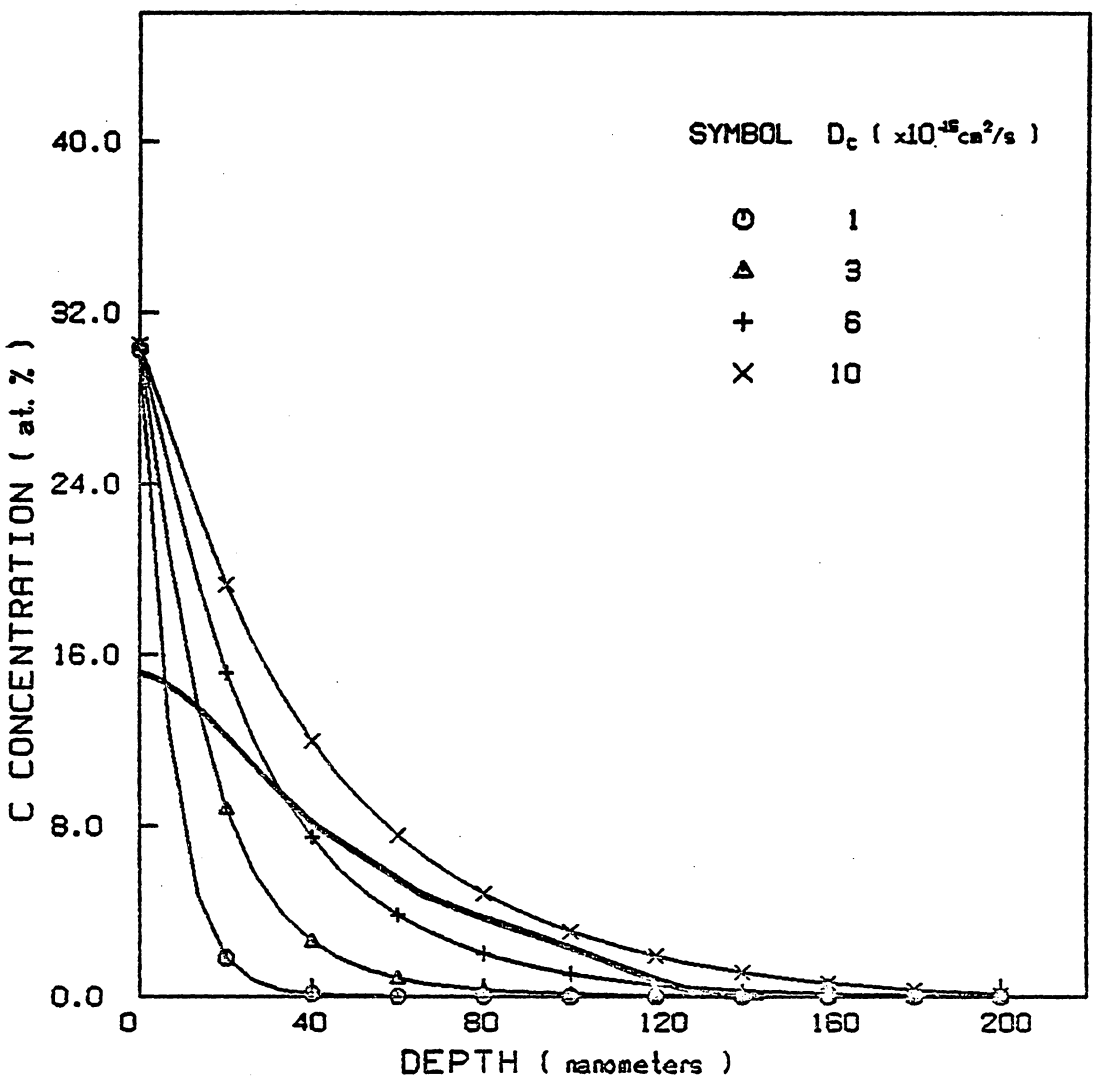

Figure 32. Experimental (heavy line) and calculated profiles (for various C diffusivities) for a fluence of $50 \times 10^{16}/cm^2$ at 190 keV (without saturation of carbon at surface).

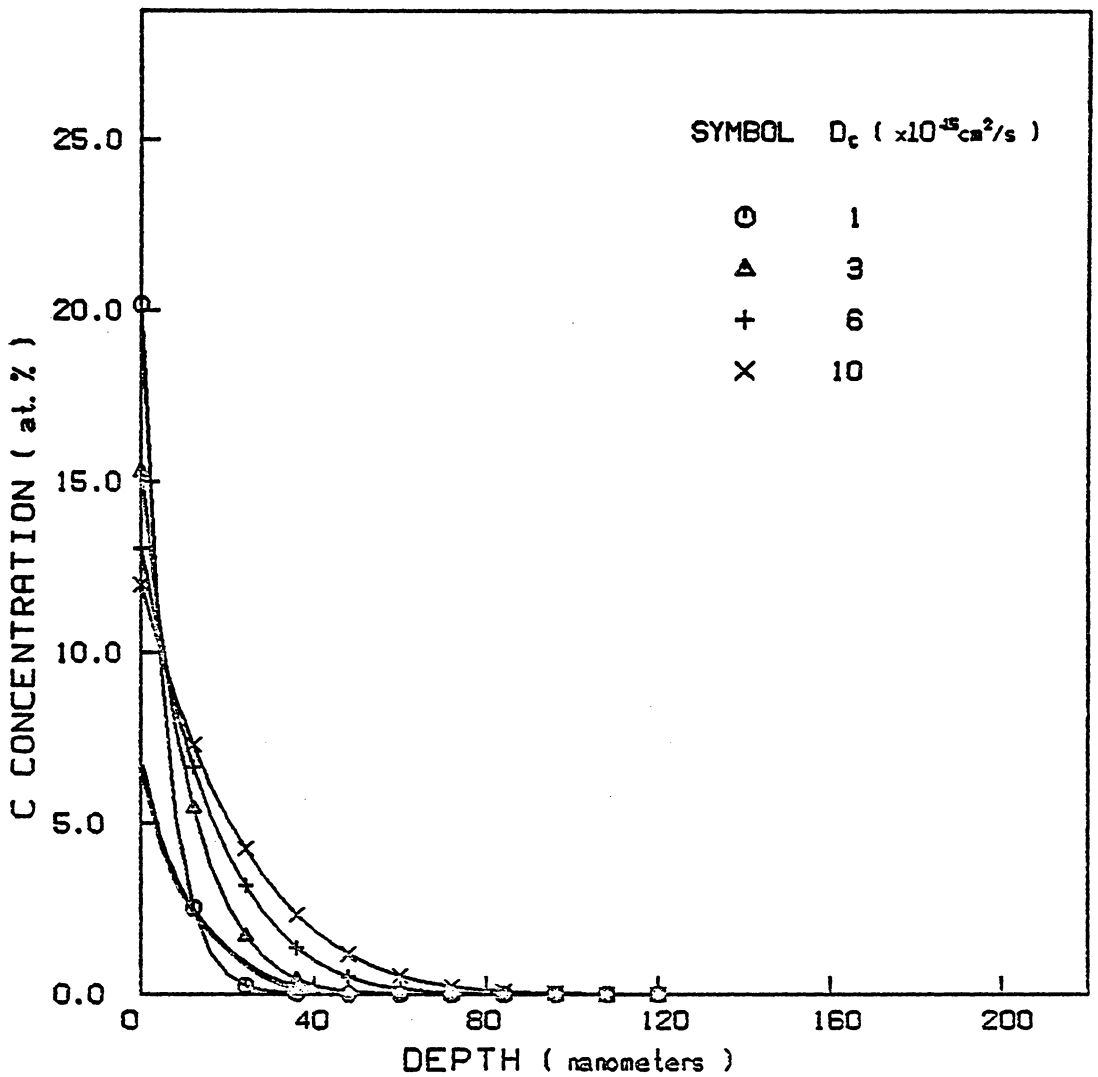

Figure 33. Experimental (heavy line) and calculated profiles (for various C diffusivities) for a fluence of $5x10^{16}/cm^2$ at 55 keV (without saturation of carbon at surface).

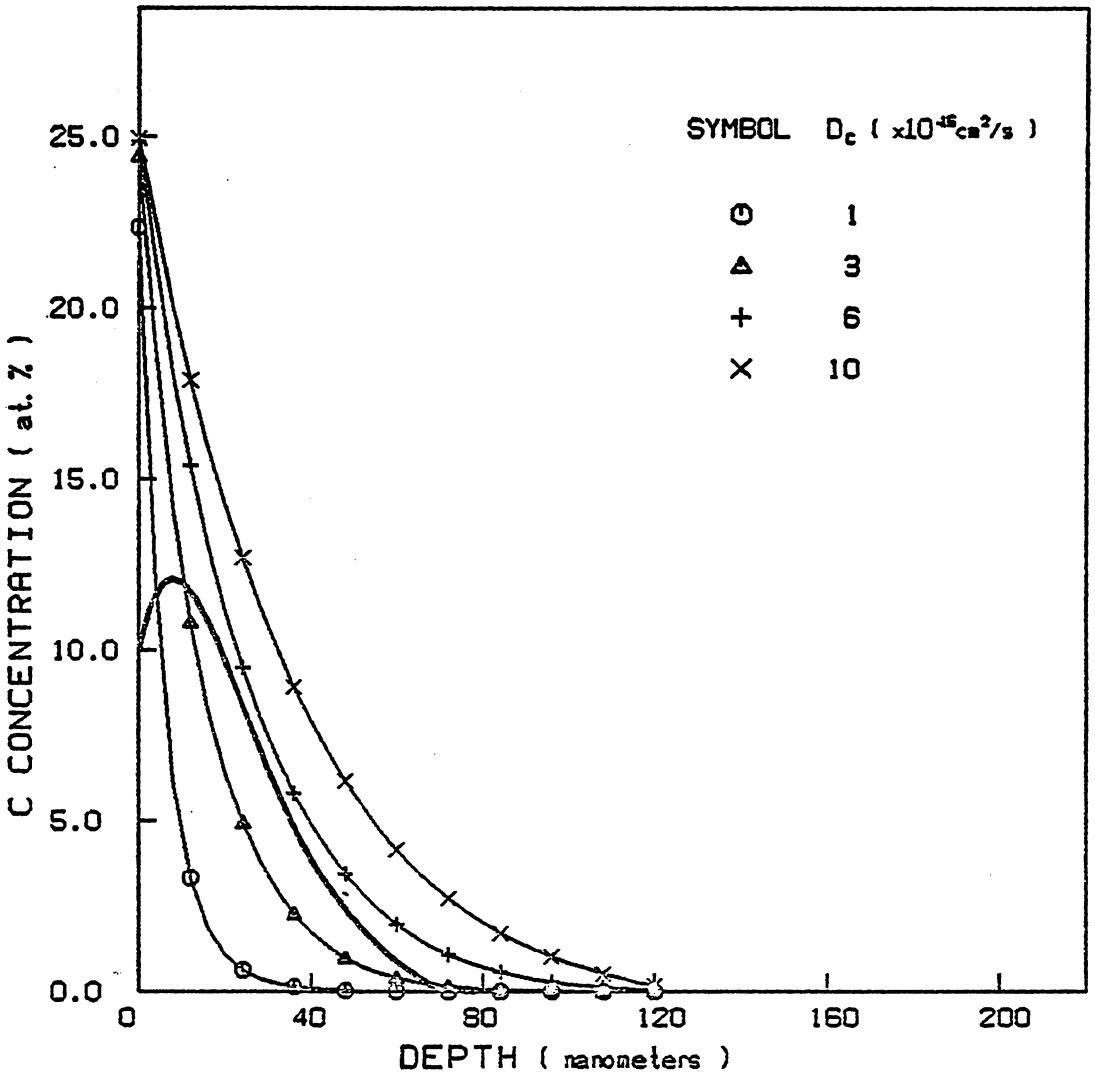

Figure 34. Experimental (heavy line) and calculated profiles (for various C diffusivities) for a fluence of $16 \times 10^{16}/cm^2$ at 55 keV (without saturation of carbon at surface).

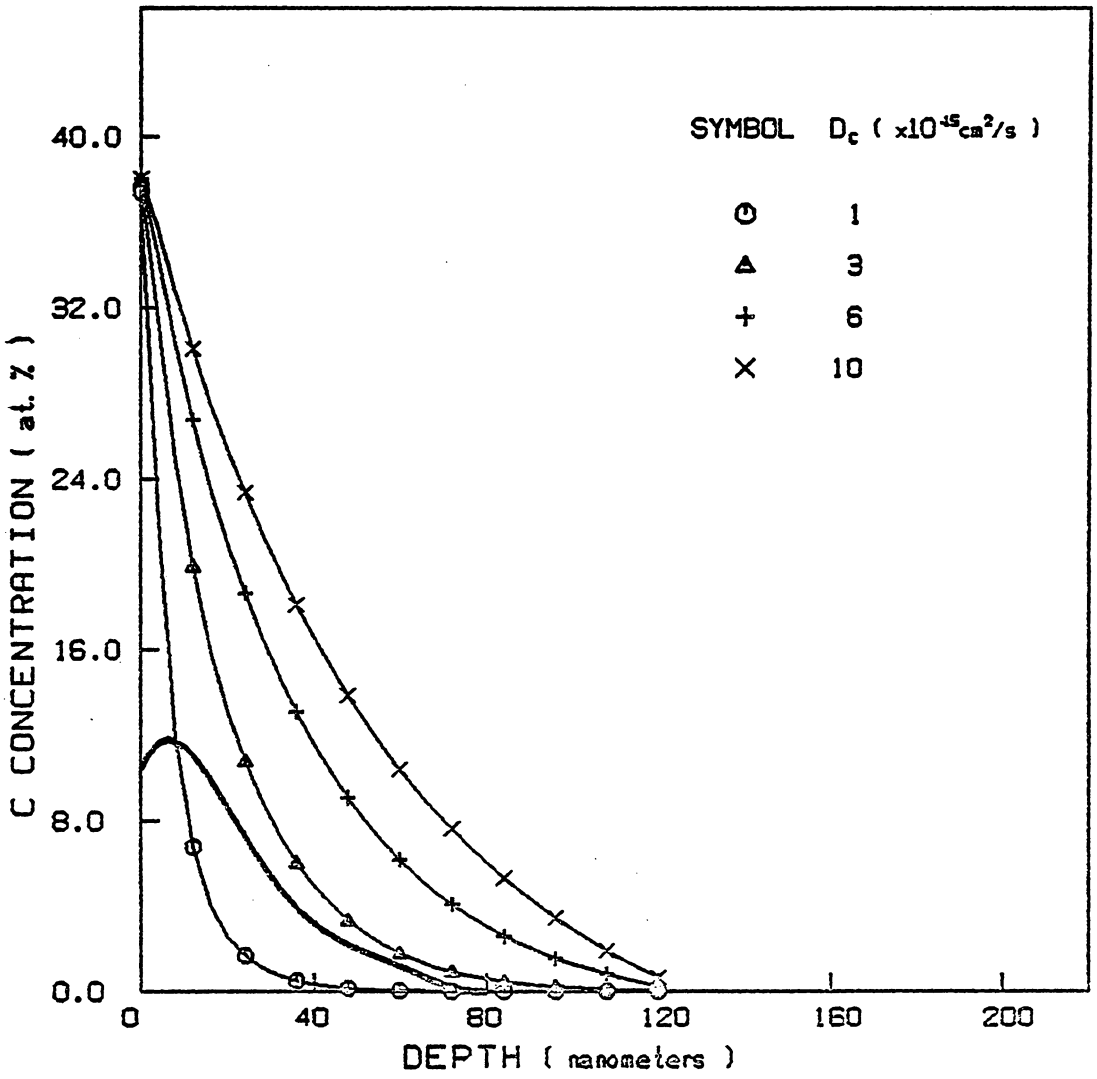

Figure 35. Experimental (heavy line) and calculated profiles (for various C diffusivities) for a fluence of $40 \times 10^{16}/cm^2$ at 55 keV (without saturation of carbon at surface).

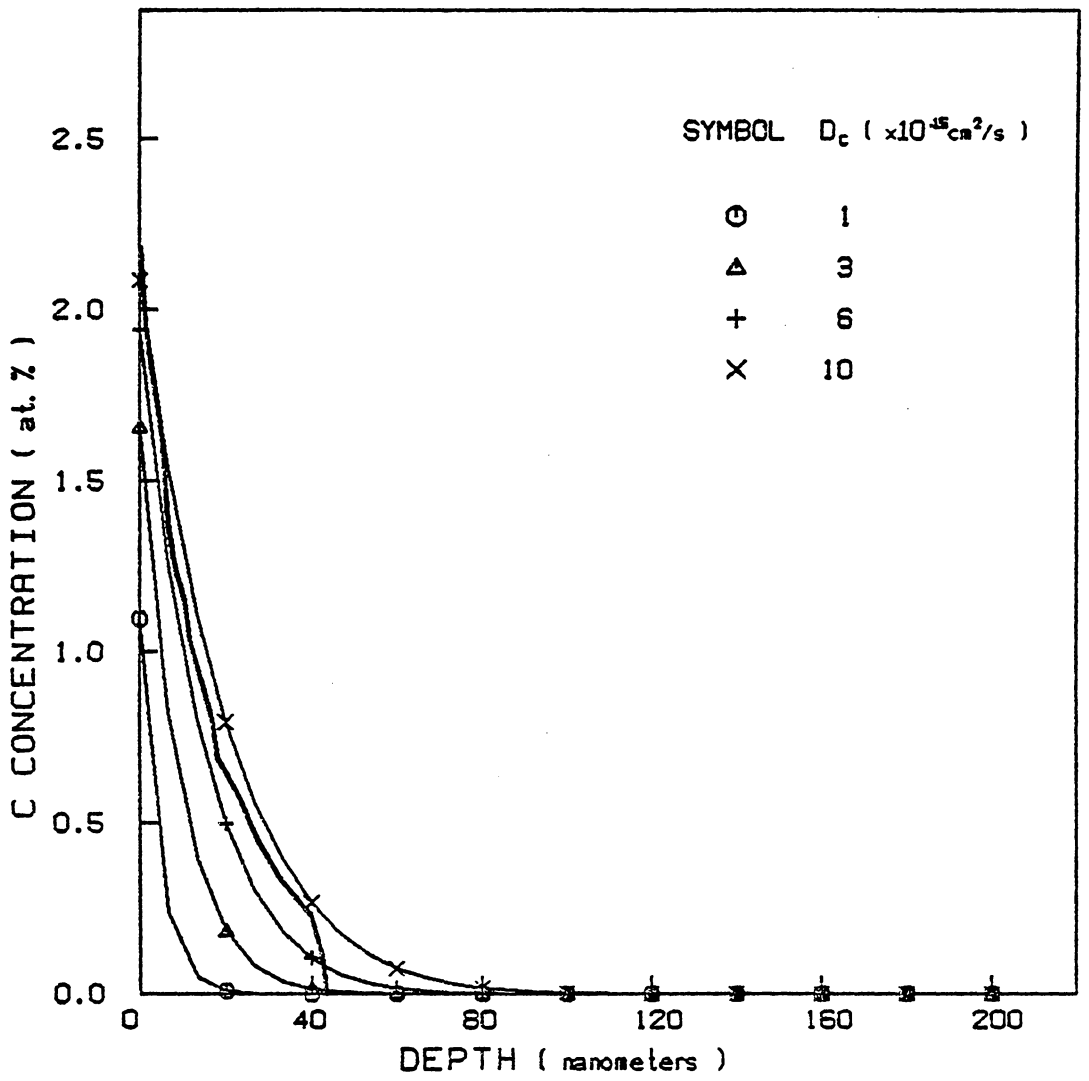

Figure 36. Experimental (heavy line) and calculated profiles (for various C diffusivities) for a fluence of $5x10^{16}/cm^2$ at 190 keV (with saturation of carbon at surface at 16 a/o).

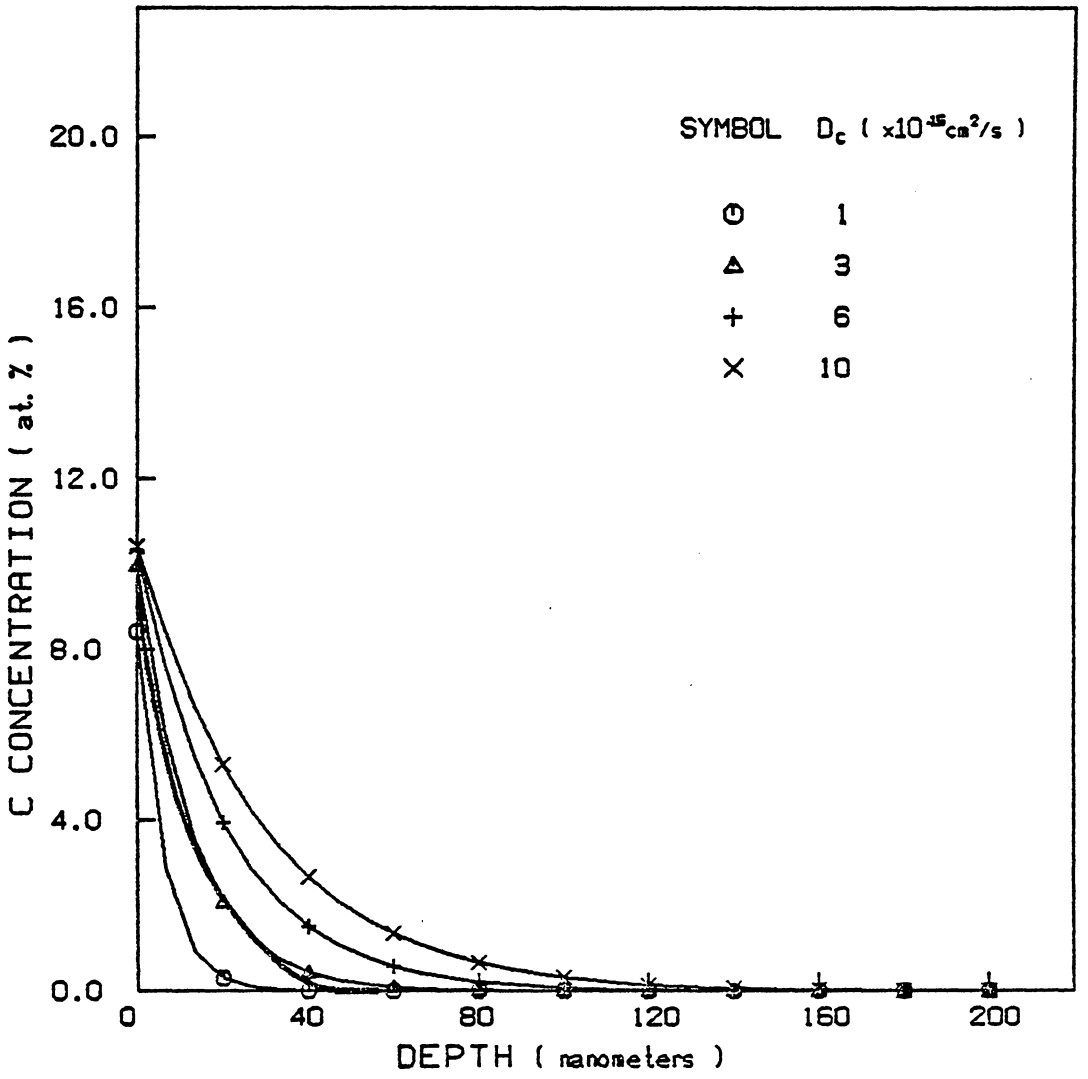

Figure 37. Experimental (heavy line) and calculated profiles (for various C diffusivities) for a fluence of $16 \times 10^{16}/cm^2$ at 190 keV (with saturation of carbon at surface at 16 a/o).

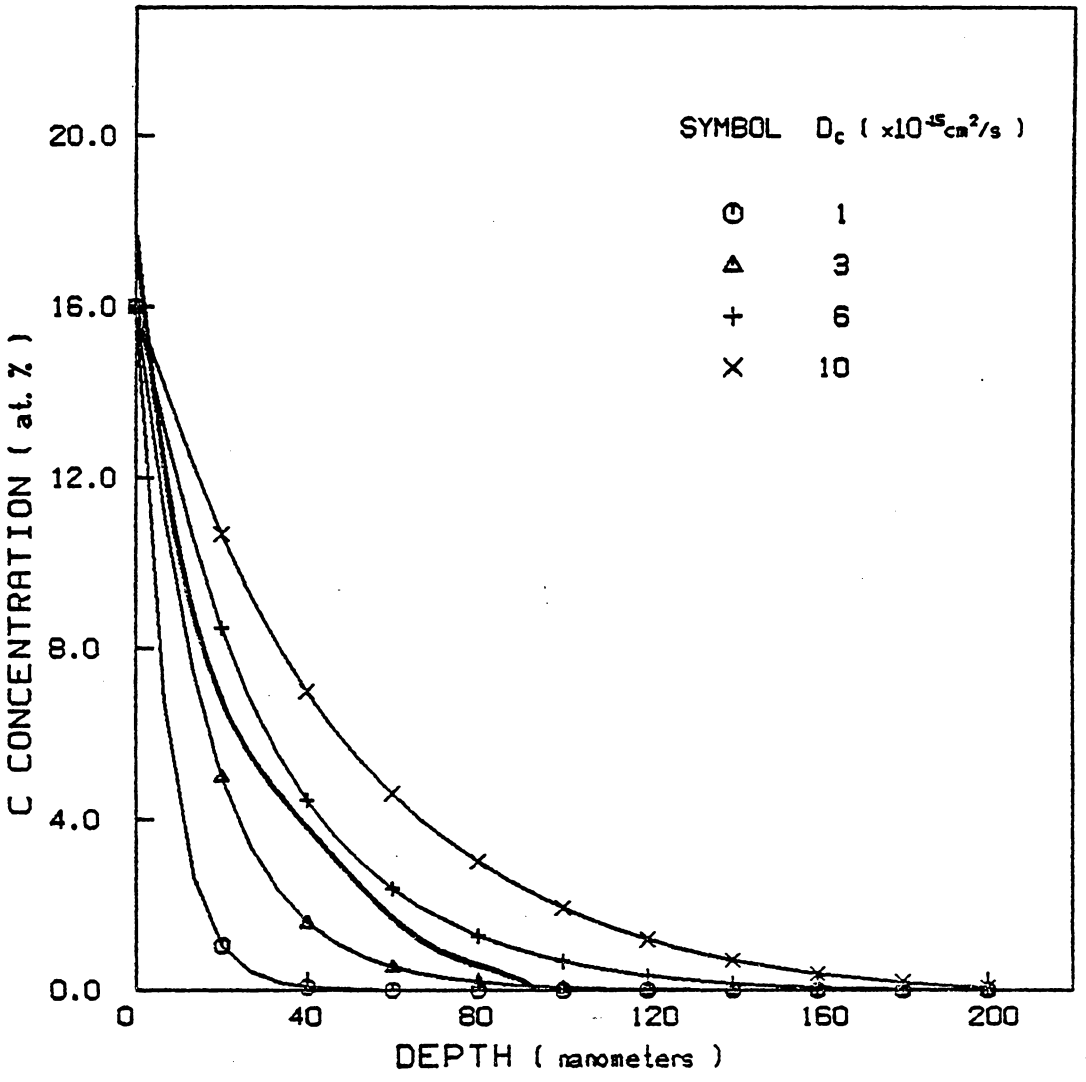

Figure 38. Experimental (heavy line) and calculated profiles (for various C diffusivities) for a fluence of $40 \times 10^{16}/cm^2$ at 190 keV (with saturation of carbon at surface at 16 a/o).

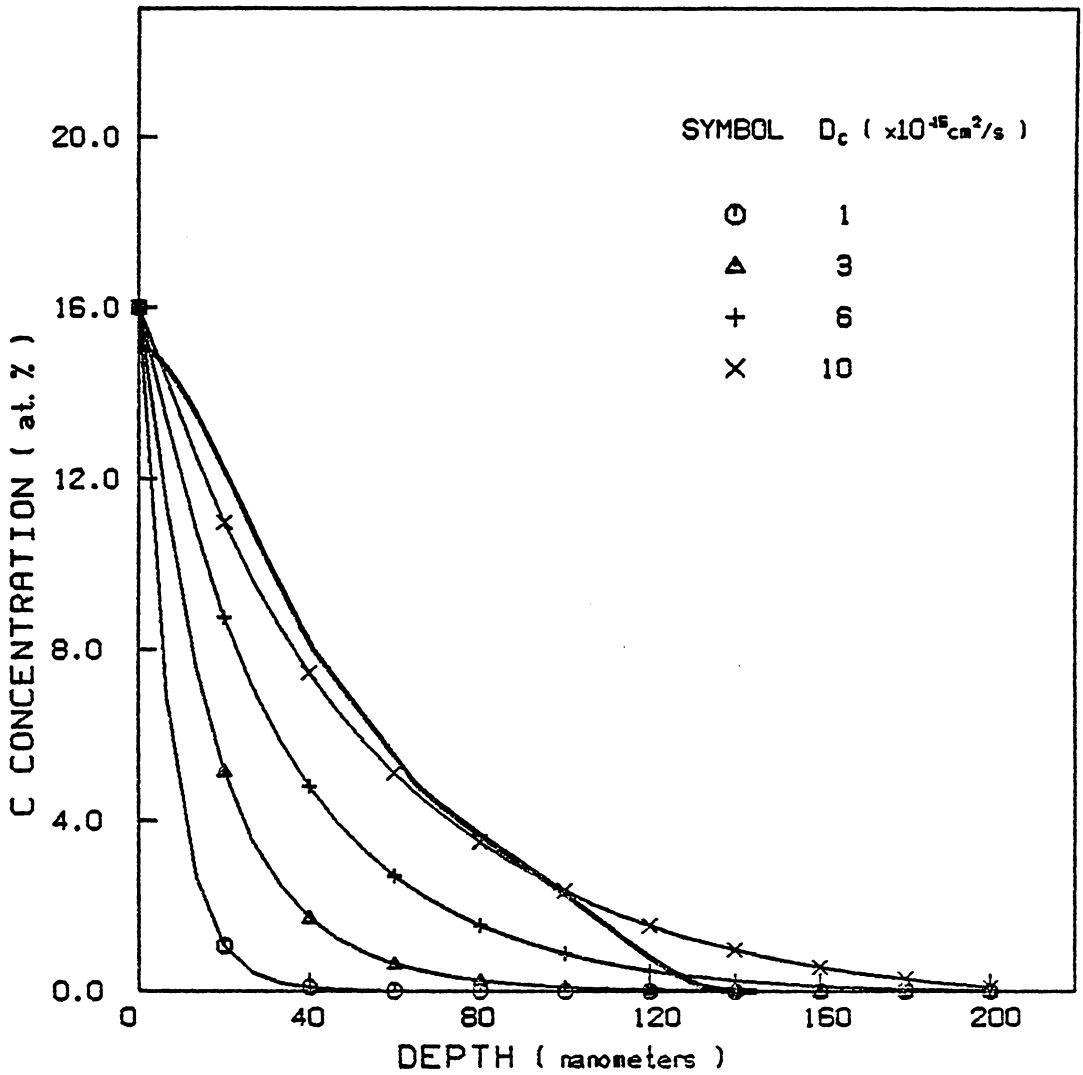

Figure 39. Experimental (heavy line) and calculated profiles (for various C diffusivities) for a fluence of $50 \times 10^{16}/cm^2$ at 190 keV (with saturation of carbon at surface at 16 a/o).

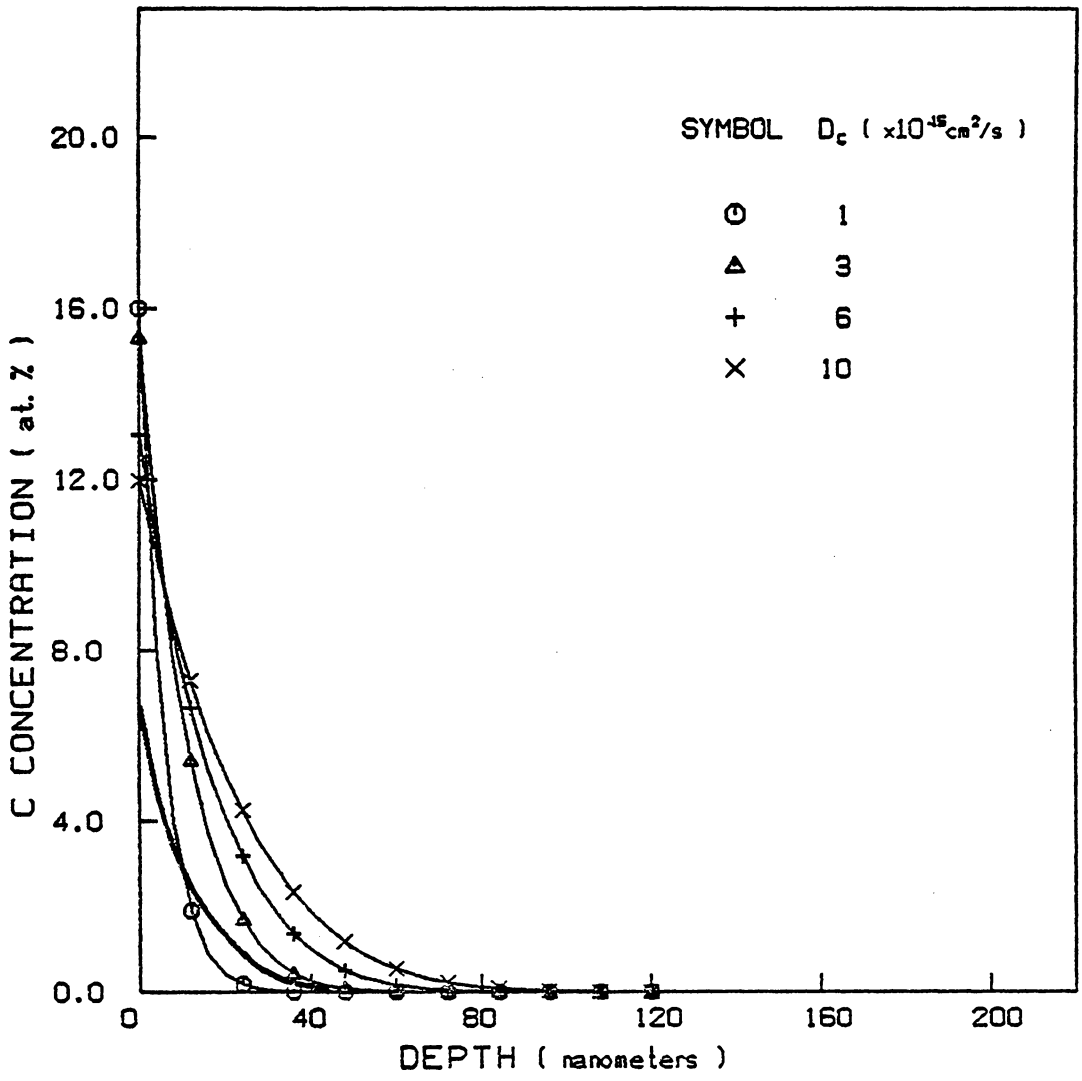

Figure 40. Experimental (heavy line) and calculated profiles (for various C diffusivities) for a fluence of $5 \times 10^{16}/cm^2$ at 55 keV (with saturation of carbon at surface at 16 a/o).

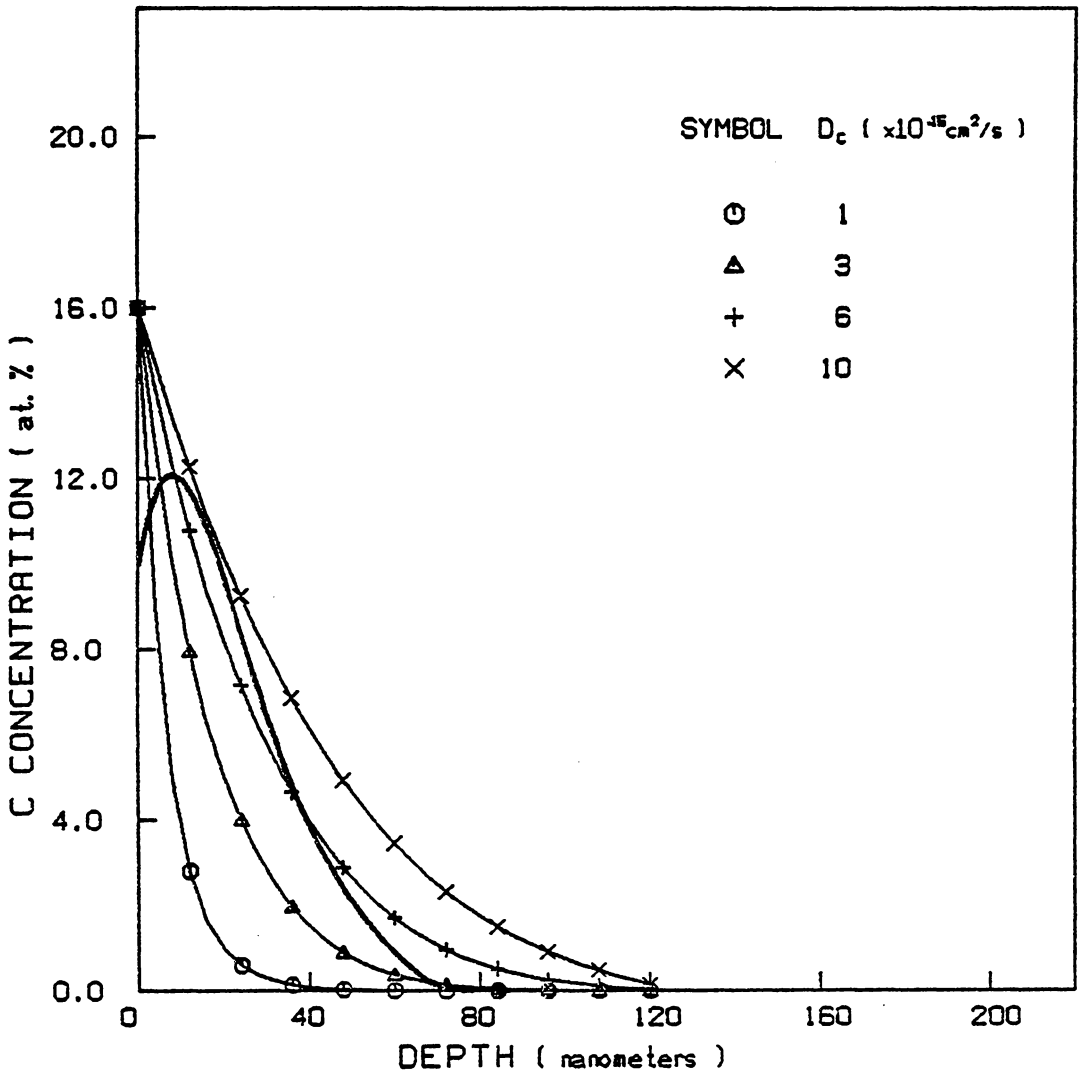

Figure 41. Experimental (heavy line) and calculated profiles (for various C diffusivities) for a fluence of $16 \times 10^{16}/cm^2$ at 55 keV (with saturation of carbon at surface at 16 a/o).

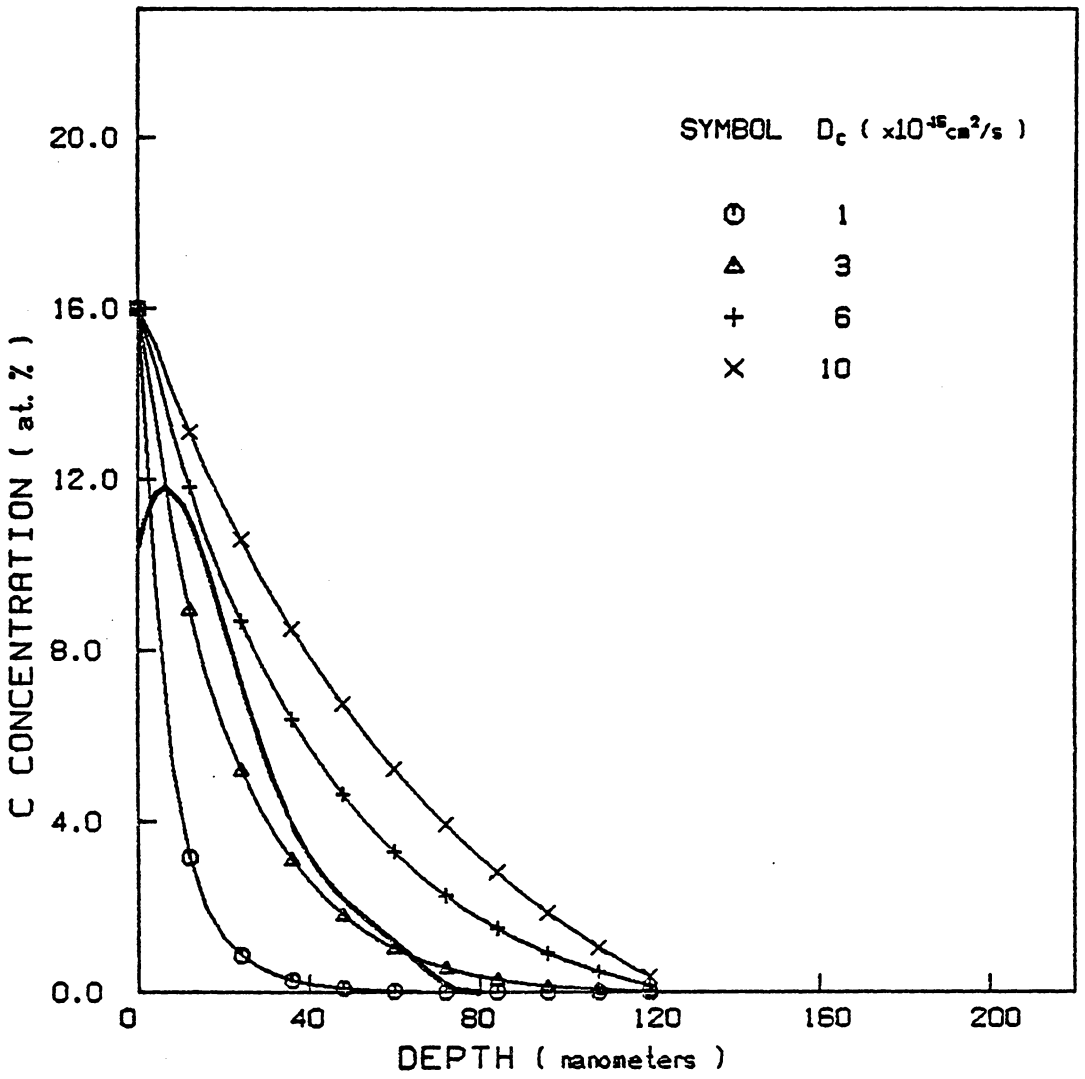

Figure 42. Experimental (heavy line) and calculated profiles (for various C diffusivities) for a fluence of $40 \times 10^{16}/cm^2$ at 55 keV (with saturation of carbon at surface at 16 a/o).

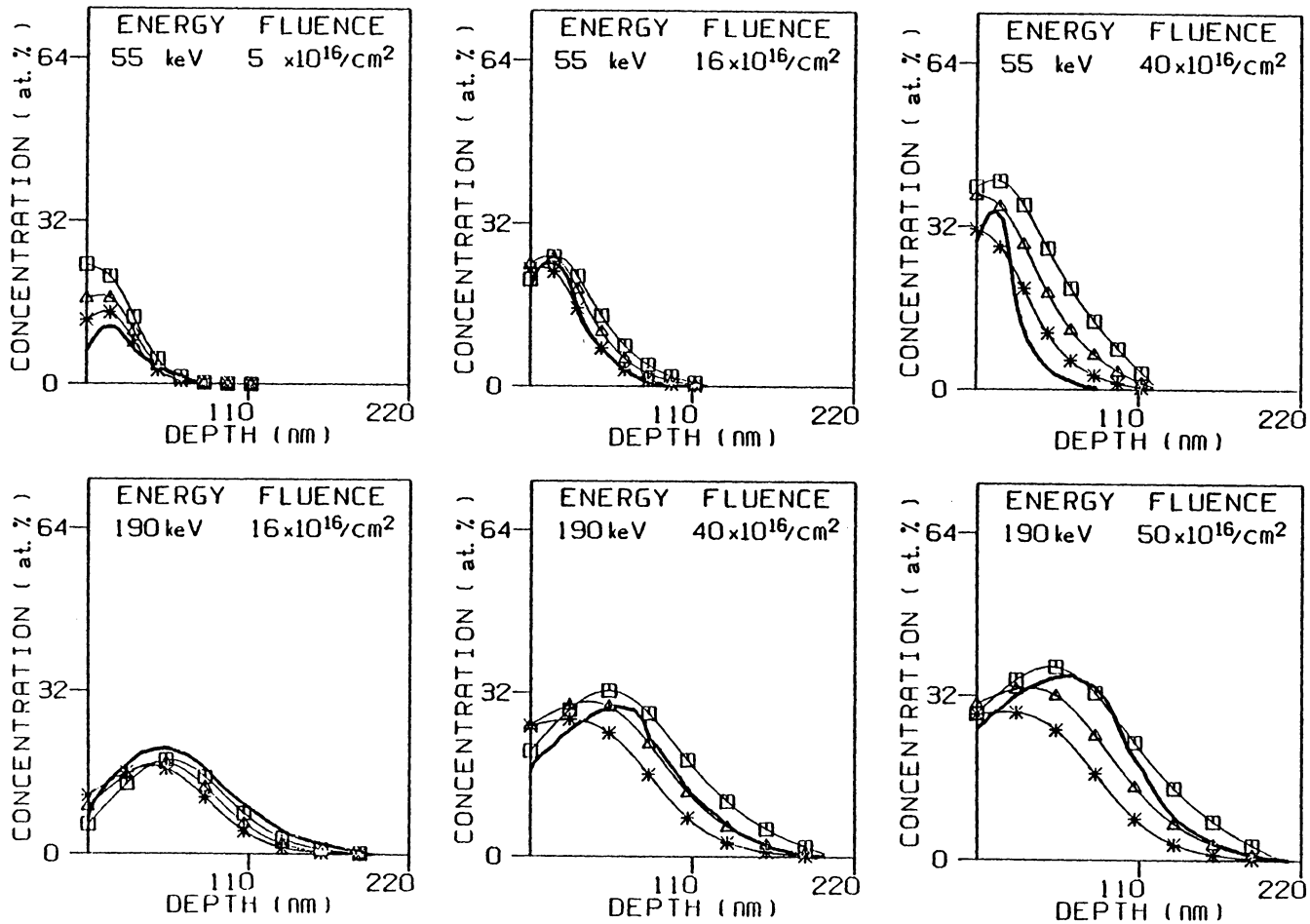

Figure 43. Experimental (heavy line) and calculated Ti profiles for several values of S [□ : 1.0; Δ : 2.0; * : 3.0], with a Ti diffusivity of $6 \times 10^{-15} cm^2/s$.

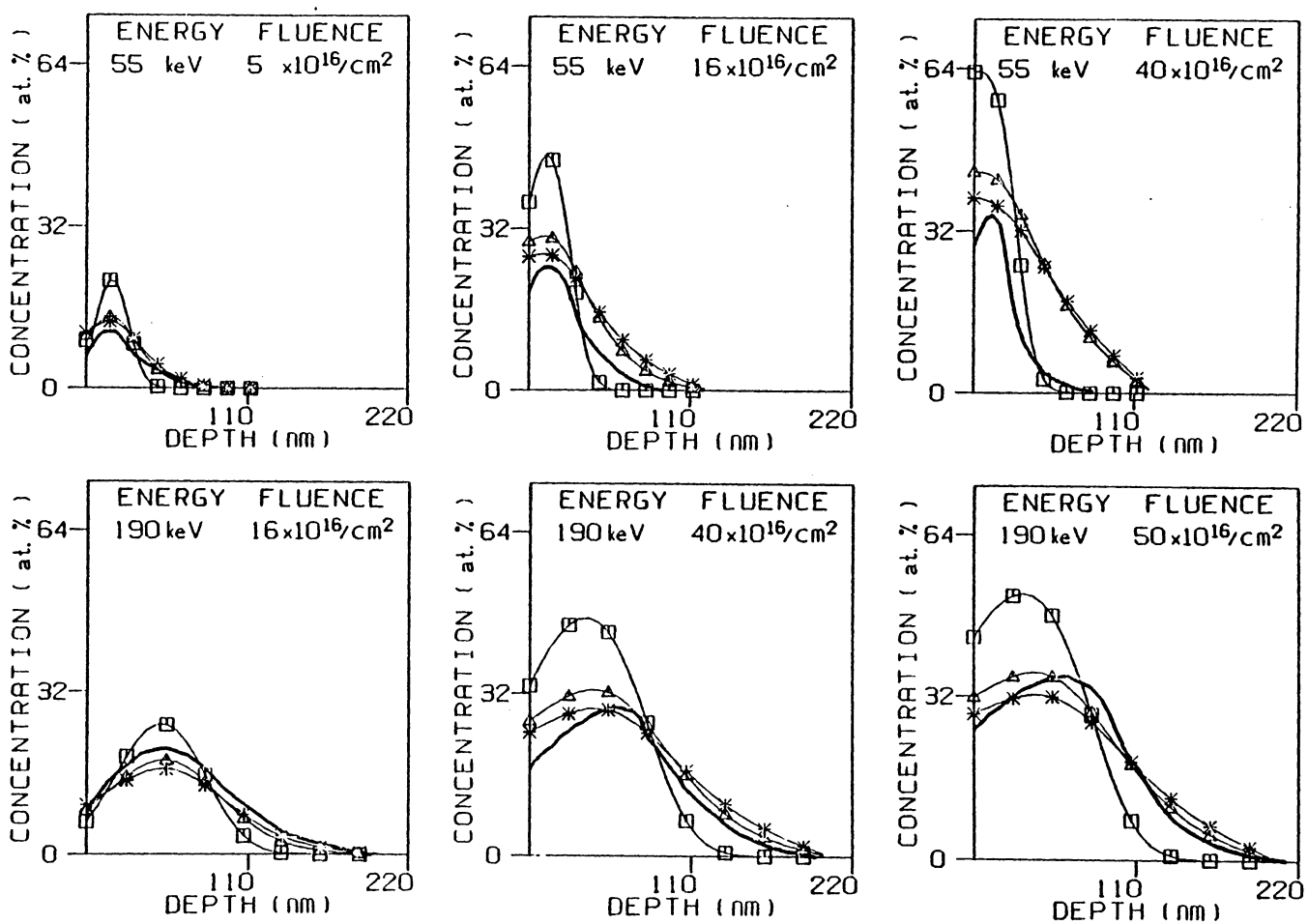

Figure 44. Experimental (heavy line) and calculated Ti profiles for several values of Ti diffusivity [□ : 0; Δ : 6; * : 10(x10^{-15}cm^2/s)], with S = 1.5.

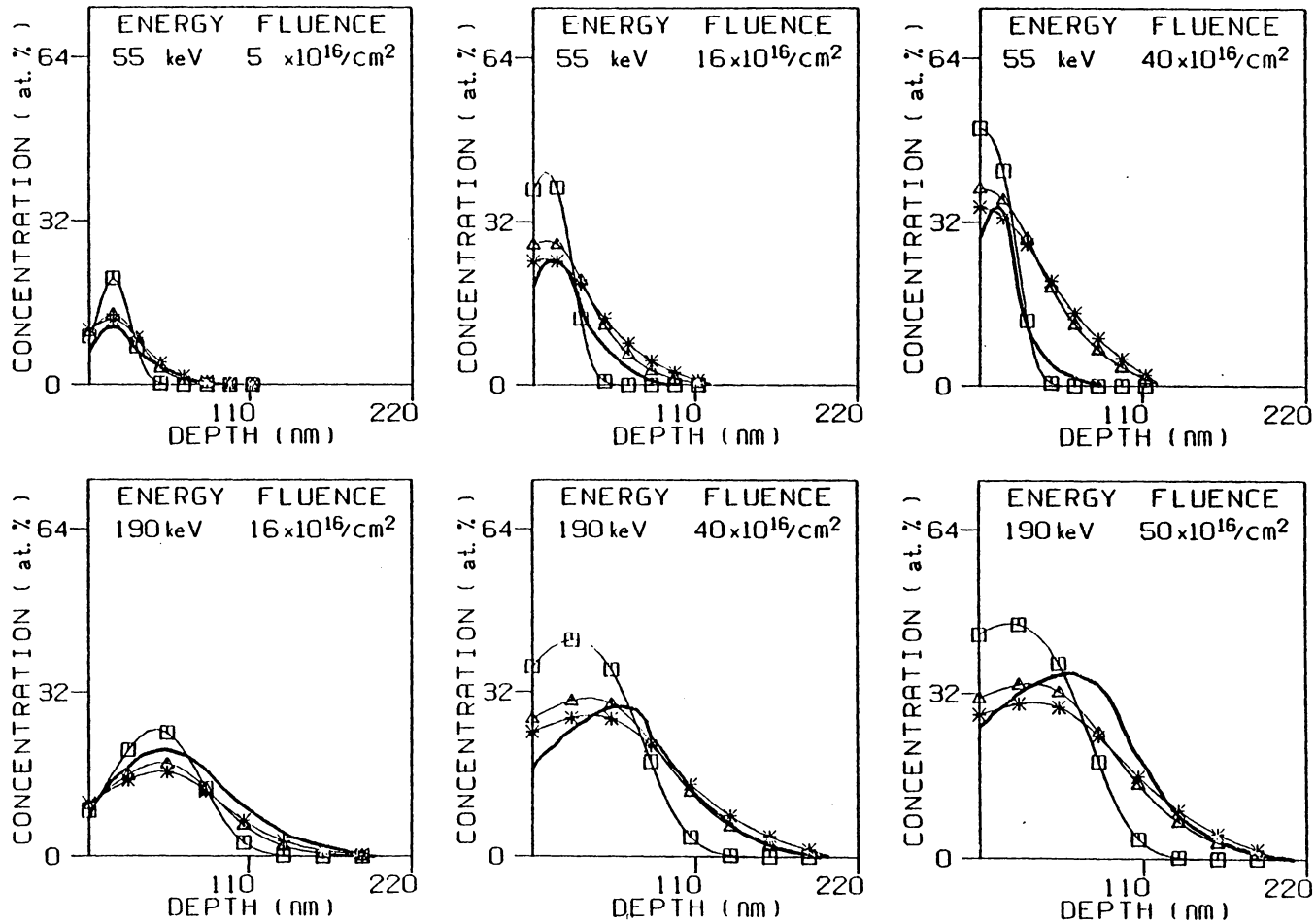

Figure 45. Experimental (heavy line) and calculated Ti profiles for several values of Ti diffusivity [□ : 0; Δ : 6; * : 10($\times 10^{-15}$ cm^2/s)], with S = 2.

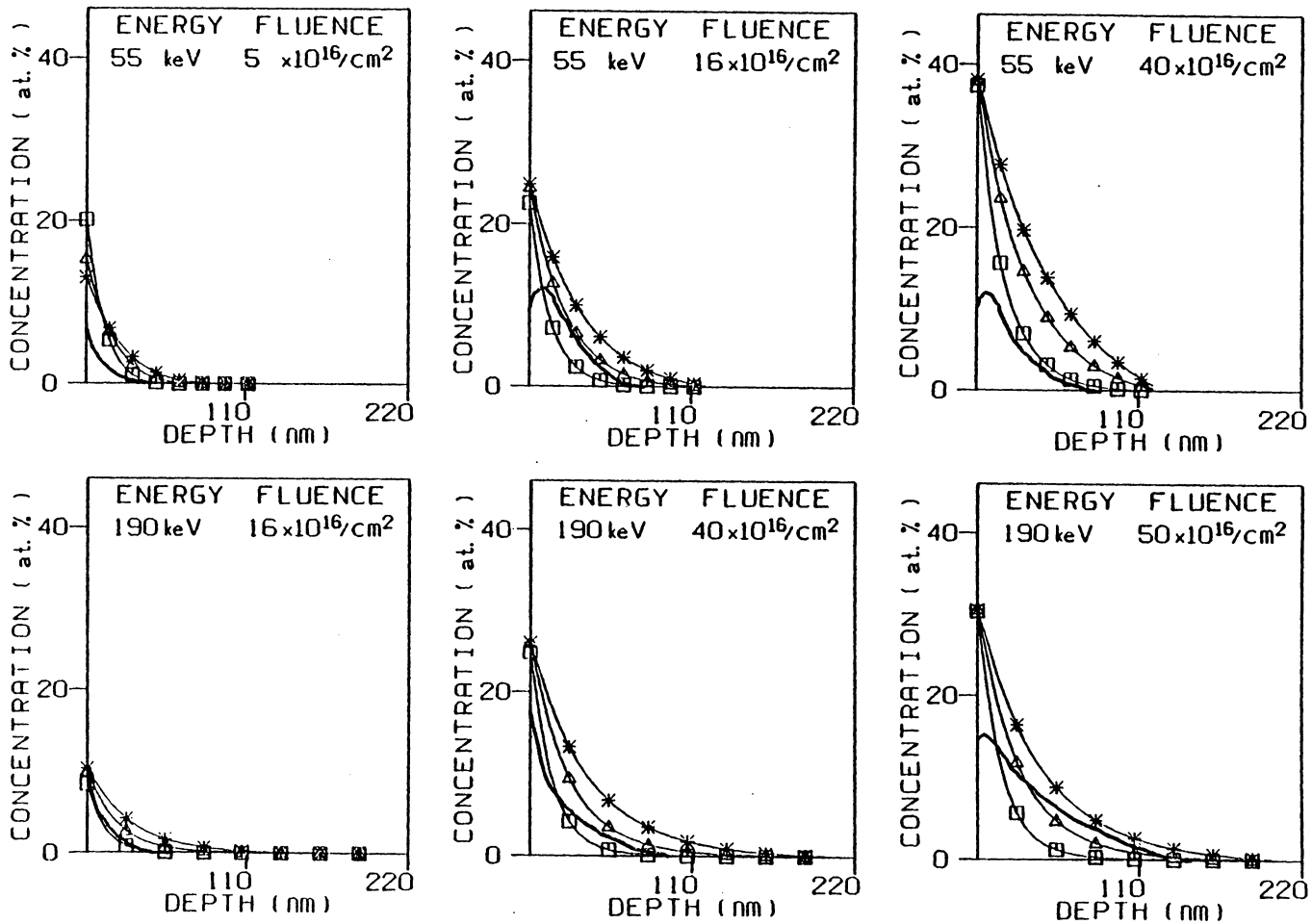

Figure 46. Experimental (heavy line) and calculated C profiles for several values of C diffusivity [□ : 3; Δ : 6; * : 10($\times 10^{-15}$ cm²/s)], with S = 2, and without saturation of C at surface.

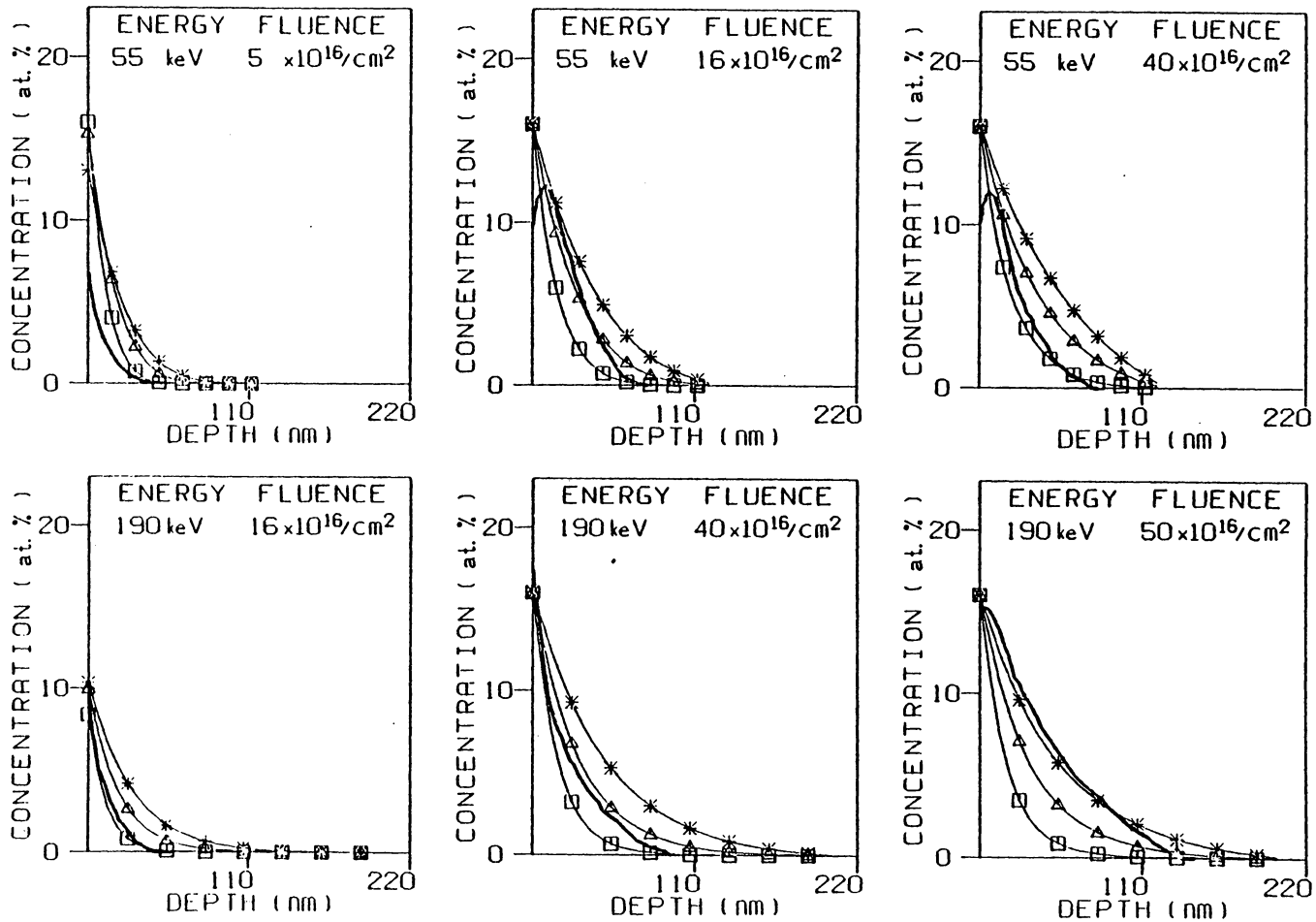

Figure 47. Experimental (heavy line) and calculated C profiles for several values of C diffusivity [□ : 3; Δ : 6; * : 10($\times 10^{-15}$ cm^2/s)], with S = 2, and with saturation of C at surface.

7.0 DISCUSSION

Composition-versus-depth profiles calculated from the coupled diffusion equations (1a) and (1b) were found to be in good agreement with the experimentally determined profiles for high fluences of Ti implanted into steel. To achieve agreement the computational method had to take into account the effects of sputtering and lattice dilation, as done by previous investigators, as well as diffusion-like processes. Lattice dilation and the sputter erosion of the surface had to be included in order to obtain reasonable agreement with experiment based on the values for range and straggling given by LSS theory. Other phenomena may also be present in high fluence ion implantation, namely preferential sputtering and radiation induced segregation. However the agreement obtained in the present work suggests that these effects are not very significant for Ti implanted into steel. For other cases where the implanted and target species have very different atomic masses, preferential sputtering may be very significant and should be included in the calculations.

The calculated curves in Figs. 43-45 show the effects of diffusivity on the Ti profiles as they evolve toward steady state at highest fluences. Atoms diffuse away from peak concentrations thereby reducing the peak maximum value

and broadening the profile. This broadening, in turn, modifies the surface concentrations and retained doses of implanted Ti, relative to the nondiffusing profiles. At low fluences, sputtering brings more of the out-diffusing Ti atoms to the surface, reducing the retained dose (slightly) but increasing the surface Ti concentration, $[Ti]^s$. This early gain of $[Ti]^s$ is soon lost at higher fluences as the initial peak depth approaches the surface with its peak concentration diminished by diffusion. A steady state profile, which would be reached a short time later without diffusion, is delayed by the reduced surface concentration. A broader steady state profile is finally achieved at higher fluences, with a comparable increase in the dose of retained Ti. At steady state, the surface concentration is limited by sputtering. The maximum concentration that can be reached is equal to the inverse of the sputtering yield of implanted atoms.

Several observations about the Ti implantation alloying process can be drawn from the results of the present work.

First, the sputtering yield of steel by Ti atoms is approximately 2 at fluences below those needed to form a carburized surface, but less than 2 at higher fluences. For Ar and Fe ions sputtering off Fe targets, sputtering yields of 2.2 and 2.8, respectively have been measured (46). It is possible that the sputtering yield of Ti is lowered when it is bonded to C (51). When carbon is present at the surface

some C atoms are also sputtered. Thus the number of Ti atoms sputtered is reduced and the sputtering yield of Ti is effectively lowered. While C atoms are lost from the surface due to sputtering, they are immediately regained from the atmosphere maintaining the C concentration at the same level. More generally, it is even possible that the anomalous dips in the self sputtering yield of reactive metals (V, Ti, Zr, Nb, Hf, Ta) presented by Almen and Bruce (28) over twenty years ago are attributable to carburization effects.

Second, the broadened profiles obtained experimentally can be accounted for by an effective diffusivity for Ti of $D_{Ti} = 6x10^{-15} cm^2/sec$. Since this value of thermal diffusivity would require a temperature of 580°C (12) the diffusivity observed in the present problem is clearly implantation-induced. Radiation enhanced diffusion is expected to produce an effective diffusivity of this order of magnitude for implantation fluxes between $1\text{-}10x10^{13}$ ions/sec-cm^2 (53). Furthermore, if the effective diffusion coefficient is calculated on the basis of the Kinchin-Pease relation (38), similar values are obtained.

Finally, a diffusion-like process accounts nicely for the inward migration of C into steel during Ti implantation. The assumption of a saturation value for the C adsorbed on the surface, which resulted in better agreement with experiment, is reasonable as follows. The dissociative

chemisorption process, believed to produce surface carbide species (3) is in competition with a molecular desorption process which reduces the surface carbide concentration. Both processes have thermal contributions and, at room temperature, the chemisorption process cannot be expected to be 100% efficient.

The present model cannot definitely identify the mechanism of the observed effective diffusion of C, $D_C = 6x10^{-15} cm^2/sec$. Three processes can contribute to this effective diffusivity value. These are thermal (non-enhanced) diffusion, radiation enhanced thermal diffusion and cascade mixing. Thermal diffusion of C in Fe at the sample temperature (40°C) is $10^{-16} cm^2/sec$ (16), and therefore contributes only 2% of the migration process. A recent Monte-Carlo type calculation for the collision cascade effect during the carburization of Cr implanted Cr could account for no more than 20% of the C adsorbed as observed experimentally (17). It appears that in the present case both collision cascades and radiation-enhanced diffusion may contribute to the inward migration of C, although the latter may be more significant. The effect of the chemical affinity of C for Ti on diffusivity still needs to be explored.

8.0 CONCLUSIONS

The formalism developed permits generation of concentration versus depth profiles under complicated implantation conditions such as vacuum carburization during sputtering. The present calculations provide semi-quantitative evaluation of several of the dynamic processes present in high fluence reactive ion implantation. For the case of Ti implanted into 52100 steel the following can be concluded: the sputtering yield decreases from a value greater than 2 to a value smaller than 2 as fluence increases, possibly due to the incorporation of carbon with increasing fluence.

It is necessary to incorporate lattice dilation and a diffusion process for Ti in order to explain the experimental results; otherwise a range and straggling that are very different from those predicted by LSS theory would be required. The order of magnitude of this diffusion process is characterized by a value of $D_{Ti} = 6x10^{-15} cm^2/sec$, which is consistent with a cascade mixing mechanism.

The diffusion process responsible for C penetration can be described by Fick's law and is characterized by an apparent diffusion coefficient of $D_C = 6x10^{-15} cm^2/sec$. It is likely that both radiation enhanced diffusion and cascade mixing contribute to the inward migration of C. The amount

of C adsorbed at the surface can be adequately described by a one to one relation with the amount of Ti at the surface up to a certain saturation limit around 16 at.% carbon. The chemistry at the surface has an important effect.

8.1 PROSPECTIVE FOR FURTHER WORK:

Further work in the modeling of high fluence implantation processes could include different types of effects on the ion collection profiles. Since the cascade-mixing process would have a diffusion-like effect mainly up to the peak range, a need for introducing depth dependent diffusivity arises. Modeling of implantation experiments done at different temperatures, would be useful to determine whether or not carbon penetration is a thermally activated process. Experiments using different ion fluxes to obtain the same fluences would also help in understanding the carbon penetration mechanism. Preferential sputtering of one of the components in the target could have significant effects on the retained dose of the implanted ions and also introduce a varying surface recession rate. Since the implantation process introduces a large defect population, radiation induced segregation of the constituents of the target material could occur. Another area for computer modeling is the implanta-

tion of N into iron leading to the precipitation of second phases which would be diffusion dependent. Lastly, ion beam mixing using argon beam on a multilayered target presents an immense potential for semiconductor applications and is in need of theoretical modeling.

9.0 REFERENCES

1. D. I. Potter, M. Ahmed and S. Lamond, J. of Metals, 35(8), 17 (1983).

2. V. Ashworth, R. P. M. Procter and W. A. Grant, "Treatise on Materials Science and Technology", vol. 18, Ion Implantation, edited by J. K. Hirvonen, Academic Press, New York, New York (1980).

3. P. L. Bonara, M. Bassoli, G. Cerisola, P. L. DeAnna, S. Lo Russo, P. Mazzoldi, B. Tiveran, I. Scotoni, C. Tosello and A. Bernard, Nucl. Inst. and Meth., 182/183, 1001 (1983).

4. G. Dearnaley, J. of Metals, 35(9), 18 (1982).

5. G. Dearnaley, Nucl. Inst. and Meth., 182/183, 899 (1981).

6. F. H. Stott, Zhou Perde, W. A. Grant and R. P. M. Proctor, Corrosion Science, 22, 305 (1982).

7. C. R. Clayton, Nucl. Instr. and Meth., 182/183, 865 (1981).

8. N. E. W. Hartley, Thin Solid Films, Tech., 64, 177 (1979).

9. J. K. Hirvonen, J. Vac. Science and Tech., 15, 1662 (1978).

10. C. A. dos Santos, M. Behar and I. J. R. Baumvol, J. Phys. D: Appl. Phys. 17, 551 (1984).

11. N. E. W. Hartley, in 'Ion Implantation' edited by J. K. Hirvonen (Academic Press, NY, 1980) p.17.

12. G. K. Hubler, in 'Metastable Materials Formation by Ion Implantation', edited by S. T. Picraux and W. J. Choyke (Elsevier, NY, 1982) p. 341.

13. I. L. Singer, in 'Ion Implantation and Ion Beam Processing of Materials' edited by G. K. Hubler, O. W.

Holland, C. R. Clayton and C. W. White (North-Holland, NY 1984) p.585.

14. I. L. Singer, Nucl. Inst. and Meth., 182/183, 923 (1981).

15. I. L. Singer, R. N. Bolster and C. A. Carosella, Thin Solid Films, 73, 283 (1980).

16. C. A. Carosella, I. L. Singer, R. C. Bowers and C. R. Gosset, in 'Ion Implantation Metallurgy' (Metallurgical Society of AIME, Warrendale, Pennsylvania, 1980), p. 103.

17. J. A. Knapp, D. M. Follstaedt and S. T. Picraux, Appl. Phys. Lett., 37, 330 (1980).

18. I. L. Singer, C. A. Carosella, and J. R. Reed, Nucl. Instr. Methods, 182/183, 923 (1981).

19. J. M. Poate, Thin Solid Films, 58, 133 (1979).

20. I. L. Singer and T. M. Barlak, Appl. Phys. Lett. 43, 457 (1983).

21. I. L. Singer, J. Vac. Sci. Technology. A, 1, 419 (1983).

22. F. Schulz, K. Wittmaak and J. Maul, Radiat. Eff., 18, 211 (1973).

23. F. Schulz and K. Wittmaak, Radiat. Eff., 29, 31 (1976).

24. H. Krautle, Nucl. Instrum. Methods, 134, 167 (1976).

25. J. F. Gibbons, W. S. Johnson and S. W. Mylorie, 'Projected Range Statistics - Semiconductors and Related Materials',2nd ed. (distributed by Halstead Press, 1975).

26. I. Manning and G. P. Mueller, Comp. Phys. Comm., 7, 85 (1974).

27. J. P. Biersack and L. G. Haggmark, Nucl. Inst. Meth., 174, 257 (1980).

28. O. Almen and G. Bruce, Nucl. Instr. and Meth., 11, 257 (1961).

29. O. Almen and G. Bruce, Nucl. Instr. and Meth., 11, 279 (1961).

30. M. T. Robinson, Appl. Phys. letters, 41, 49 (1962).

31. E. Selin, S. E. Arnell and O. Almen, Nucl. Instr. Meth., 56, 218 (1967).

32. E. Arminen, A. Fontell and V. K. Lindroos, Phys. Stat. Sol.(a), 4, 663 (1971).

33. H. J. Smith, Phys. Letters,ethods, 37A, 289 (1971).

34. J. P. Biersack, Rad. Effects, 19, 249 (1973).

35. H. H. Andersen, Rad. Effects, 19, 257 (1973).

36. H. Krautle and S. Kalbitzer, in 'Proc. III Int. Conf. Implantation in Semiconductors and other Materials', ed. by B. L. Crowder, (Plenum Press, NY 1973) p. 585.

37. E. F. Krimmel and H. Pfleiderer, Rad. Effects, 19, 83 (1973).

38. S. M. Myers, Nucl. Instr. Methods, 168, 265 (1980).

39. P. Sigmund, Appl. Phys. Lett.,s, 14, 114 (1969).

40. M. J. Drinkwine and D. Lichtman, 'Partial Pressure Analyzers and Analysis', American Vacuum Society Monograph Series (AVS, 1980) p. 64.

41. Y. Fukuda, G. M. Lancaster, F. Honda and J. W. Rabalais, J. Chem. Phys., 15, 3447 (1978).

42. H. H. Andersen and H. L. Bay, in "Sputtering by Particle Bombardment I", edited by R. Behrisch (Springer Verlag 1981), p. 173.

43. M. P. Hooker and J. T. Grant, Surface Sci., 62, 21 (1977).

44. J. B. Benziger, Appl. Surf. Sci., 6, 105 (1980).

45. H. J. Mathieu, J. B. Mathieu, D. E. McClure and D. Landolt, J. Vac. Sci. Technol., 14, 1023 (1977).

46. N. K. Sharma and W. S. Williams, Thin Solid Films, 54, 75 (1978).

47. J. Crank, The Mathematics of Diffusion, 2nd ed., p. 4; Clarendon press, Oxford, 1975.

48. J. I. Goldstein and A. E. Moren, met. Trans., 9A, 1515 (1978).

49. A. R. Mitchell, "Computational Methods in Partial Differential Equations",(J. Wiley and Sons, New York 1976) Chapt. 2.

50. A. H. Eltoukhy and J. E. Greene, J. Appl. Phys., 51, 4444 (1980).

51. P. Varga and E. Taglauer, Journal of Nuclear Materials, 111/112, 726 (1981).

52. J. H. Swisher, Trans. AIME, 242, 2433 (1968).

53. G. Dearnaley, J. H. Freeman, R. S. Nelson, and J. Stephen, "Ion Implantation", (North Holland, Oxford, 1973), p. 228.

54. C. J. Smithells, "Metals Reference Book", 3rd edition (Butterworths, Washington, 1962), p. 594.

55. R. H. Bassel, K. S. Grabowski, M. Rosen, M. L. Roush, and F. Davarya, to be published in Nucl. Instr. and Meth.

APPENDIX A. PROGRAM LISTINGS

Given below is the listing of the program 'IMPLANT' that was used to generate the implantation concentration profiles.

```
C
C     ......................IMPLANT......................
C
C     THIS   PROGRAM  CALCULATES THE  CONCENTRATION PROFILES
C     OF THE  IMPLANTED ION & CARBON ( WHICH  IS  PICKED  UP
C     DURING IMPLANTATION).
C
C     THE LANGUAGE USED IS FORTRAN-77.
C
C     TO  RUN THE  PROGRAM, AN  INPUT FILE IS REQUIRED WHICH
C     GIVES THE FOLLOWING DATA.:-
C     LINE 1) NUMBER OF (A) IMPLANT  ENERGIES, (B) FLUENCES,
C             (C) FLUXES, (D)SPUTTERING YIELDS.
C     LINE 2) ENERGY, MAX IMPLANT. DEPTH , RANGE, STRAGGLING
C             (------------------DO -----------------------)
C             TO AS MANY LINES AS THERE ARE IMPLANT ENERGIES
C     LINE 3) TIME IN  HOURS  CORRESPONDING TO THE DIFFERENT
C             FLUENCES IN INCREASING ORDER.
C     LINE 4) THE CORRESPONDING FLUENCES.
C     LINE 5) THE DIFFERENT FLUX VALUES USED IN CM/SEC.
C     LINE 6) THE DIFFERENT SPUTTERING YIELDS USED.
C     LINE 7) THE  DIFFUSIVITIES  D11, D12, D13, D22, D33 IN
C             CM2/SEC.
C     LINE 8) THE INITIAL  BULK  CONCENTRATION VALUES OF C1,
C             C2, AND C3 NAMELY C10, C20, AND C30.
C     LINE 9) THE  INCREMENT OF TIME IN SECONDS.
C
C     THE  CALCULATED VALUES GO INTO AN  OUTPUT FILE. ASSIGN
C     STATEMENTS  HAVE TO  BE USED  DESIGNATE  THE INPUT AND
C     OUTPUT FILE.  FILE 11 IS FOR THE INPUT AND FILE 25 FOR
C     THE OUTPUT.
C
C     THE PROGRAM  MAKES USE OF  TWO  SUBROUTINES VMULFF AND
C     LINV1F WHICH ARE AVAILABLE IN THE IMSL (MATH) LIBRARY.
C
C     THE PROGRAM HAD BEEN CHANGED TO INCLUDE  THE EFFECT ON
C     CARBON  PICKUP DUE TO  ELEMENTS  OTHER THAN  THE  IMP-
C     LANTED IONS AND TO CONSIDER  SATURATION  OF  CARBON AT
C     SURFACE. THE CHANGES AND THE CORRESPONDING  STATEMENTS
C     ARE PRESENT AS COMMENT CARDS.
C
C     THE FOLL IS AN EXAMPLE OF AN INPUT FILE.:-
```

```
C     L 1)        2,4,1,3
C     L 2)        190.0,2.0E-5,6.5E-6,3.2E-6
C                 55.0,1.0E-5,2.0E-6,.86E-6
C     L 3)        0.15,0.48,1.20,1.50
C     L 4)        5.0,16.0,40.0,50.0
C     L 5)        1.1E-9
C     L 6)        2.0,1.5,1.75
C     L 7)        0.6E-14,.0,.0,0.6E-14,.0
C     L 8)        0.0,0.0,0.0
C     L 9)        60.0
C
C     DEFINITIONS
C
      INTEGER R,S
      REAL*4 MATRIX(90,90), MAT(90,90)
      DIMENSION X(90), D(90), C1(60), C2(60), C3(60)
      DIMENSION XD(31), X1(31), X2(31), X3(31)
      DIMENSION A(3,3), B(3,3), C(3,3), T(3,3), P(5,4)
      DIMENSION LW(90), MW(90), DX(60), WKAREA(90)
      DIMENSION EPS(60), C1P(60), C2P(60), C3P(60)
      DIMENSION XMAX(10), YMAX(10), TMAX(20), XP(10),
     :SPUT(20), FLU(10), FLUXX(10), FLNC(20), YP(10),
     :ENERGY(10), SIG(10), CSIG(10), NTV(20)
C
      CALL ERRSET (208,256,-1)
C
C     READ CONDITIONS
C
      READ(11,*) IPV,IFV,JFV,ISV
      READ(11,*) (ENERGY(I),XMAX(I),XP(I),SIG(I),I=1,IPV)
      READ(11,*) (TMAX(I),I=1,IFV)
      READ(11,*) (FLNC(I),I=1,IFV)
      READ(11,*) (FLU(I),I=1,JFV)
      READ(11,*) (SPUT(I),I=1,ISV)
      READ(11,*) D11,D12,D13,D22,D33
      READ(11,*) C10,C20,C30
      READ(11,*) DELT
C
C     GET DIFFUSIVITIES (FROM SUBROUTINE IN THE FUTURE)
C     CHANGE  PROGRAM  TO  ACCEPT  FUNCTIONS  AND  FLUXES AS
C     BOUNDARY CONDITIONS HERE
C
      WRITE(25,*) IPV,IFV,JFV,ISV
C
C
      NXGRID = 30
      DO 134 IP=1,IPV
      DELX=XMAX(IP)/NXGRID
C
```

```
C     IF(IP.EQ.2)IFV=IFV-1
C
      DO 144 IWZ = 1,IFV
      NTV(IWZ) = 3600*TMAX(IWZ)/DELT
  144 CONTINUE
      NTVMAX = NTV(IFV)
C
C     FORM MATRIX
C     FIRST A,B,C MATRICES
C
      A(1,1) = DELT*D11/(2*DELX**2)
      A(1,2) = DELT*D12/(2*DELX**2)
      A(1,3) = DELT*D13/(2*DELX**2)
      A(2,3) = 0
      A(2,1) = 0
      A(3,1) = 0
      A(3,2) = 0
      A(2,2) = DELT*D22/(2*DELX**2)
      A(3,3) = DELT*D33/(2*DELX**2)
      B(1,1) = -2*A(1,1) -1
      B(2,2) = -2*A(2,2) -1
      B(3,3) = -2*A(3,3) -1
      B(1,2) = -2*A(1,2)
      B(1,3) = -2*A(1,3)
      B(2,1) = 0
      B(2,3) = 0
      B(3,1) = 0
      B(3,2) = 0
      DO 460 R=1,3,1
      DO 460 S=1,3,1
      C(R,S)=A(R,S)
460   CONTINUE
C
C     NOW FORM THE TRIDIAGONAL MATRIX OF A  B, AND C
C
      DO 100 L=1,30,1
      DO 100 IH=1,30,1
      IF (IH.EQ.L-1) GO TO 50
      IF (IH.EQ.L)   GO TO 60
      IF (IH.EQ.L+1) GO TO 70
      DO 45 I=1,3,1
      DO 45 J=1,3,1
      T(I,J) = 0
45    CONTINUE
      GO TO 80
50    CONTINUE
      DO 550 R=1,3,1
      DO 550 S=1,3,1
```

```
      T(R,S)=A(R,S)
550   CONTINUE
      GO TO 80
60    CONTINUE
      DO 570 R=1,3,1
      DO 570 S=1,3,1
      T(R,S)=B(R,S)
570   CONTINUE
      GO TO 80
70    CONTINUE
      DO 590 R=1,3,1
      DO 590 S=1,3,1
      T(R,S)=C(R,S)
590   CONTINUE
80    CONTINUE
      DO 100 I=1,3,1
      DO 100 J=1,3,1
      M = 3*(L-1)+I
      N = 3*(IH-1)+J
      MATRIX(M,N) = T(I,J)
100   CONTINUE
C
C     INVERT MATRIX
C     INCLUDE INVERSION WITHIN LOOP WHEN  VARIABLE DIFFUSIV-
C     ITIES ARE USED
C
      LNVF2=90
      LNVF3=90
      LNVF5=0
      CALL LINV1F(MATRIX,LNVF2,LNVF3,MAT,LNVF5,WKAREA,IER)
C
      DO 134 JF=1,JFV
      DO 134 IS=1,ISV
C
C     FORM INITIAL CONCENTRATION VECTORS
C
      DO 200 I=1,60
      C1(I) = C10
      C2(I) = C20
      C3(I) = C30
200   CONTINUE
C
C     START LOOP
C
      INC=1
      DO 134 NT=1,NTVMAX
C
      DO 225 I=1,60,1
      DC2=(FLU(JF)*DELT/(2.507*SIG(IP)))*EXP(-(((I-1)*DELX-
```

```
     :XP(IP))**2)/(2*SIG(IP)**2))
      C2(I)=(C2(I)+DC2)/(1.0+DC2)
 225  CONTINUE
      EPS(1) = 0.0
      DX(1) = 0.0
      DO 226 I=2,60,1
      DX(I)=DELX*(FLU(JF)*DELT/(2.507*SIG(IP)))*EXP(-(((I-1)
     :*DELX-XP(IP))**2)/(2*SIG(IP)**2))
      EPS(I)=EPS(I-1) +DX(I)
 226  CONTINUE
C
      SPIU=(FLU(JF)*DELT*SPUT(IS))/DELX
      IKE = INT(SPIU)
      SPIKE = SPIU-IKE
C
      DO 379 IQ=1,60-IKE-1
      C1(IQ)=C1(IKE+IQ)+((C1(IKE+IQ+1)-C1(IKE+IQ))*SPIKE)
      C2(IQ)=C2(IKE+IQ)+((C2(IKE+IQ+1)-C2(IKE+IQ))*SPIKE)
      C3(IQ)=C3(IKE+IQ)+((C3(IKE+IQ+1)-C3(IKE+IQ))*SPIKE)
C
 379  CONTINUE
C
C     CARBON PICKED UP IS EQUAL TO THE TI PRESENT
C
      C1(1)=C10+C2(1)
C
C*****//CHANGE PROG TO CONSIDER SATURATION OF C AT SURFACE//
C     IF (C1(1).GE.0.16) THEN
C     C1(1)=0.16
C     END IF
C*************************************************************
C
C     LATTICE DILATION
C
      NTK = 2
      DO 255 I=2,60
      DELIM1 = (I-1)*DELX
      DO 256 J=NTK,60
      IF((EPS(J)+(J-1)*DELX).GE.DELIM1) THEN
      NTK = J
      DOX = (EPS(J)+(J-1)*DELX) - DELIM1
      GO TO 257
      END IF
 256  CONTINUE
 257  C1P(I) = ( (C1(NTK-1)-C1(NTK))*DOX/(DELX+DX(NTK)) )
     :+ C1(NTK)
      C2P(I) = ( (C2(NTK-1)-C2(NTK))*DOX/(DELX+DX(NTK)) )
     :+ C2(NTK)
      C3P(I) = ( (C3(NTK-1)-C3(NTK))*DOX/(DELX+DX(NTK)) )
```

```
     :+ C3(NTK)
 255  CONTINUE
C
      DO 275 I=2,60,1
      C1(I)=C1P(I)
      C2(I)=C2P(I)
      C3(I)=C3P(I)
      EPS(I)=0
 275  CONTINUE
C
C     FORM D
C
      D21 = 0.0
      D23 = 0.0
      D31 = 0.0
      D32 = 0.0
C
C     CNS AND CN(31) ARE  PSEODO-POINTS  OUTSIDE THE CURRENT
C     F-D GRID.  CNS ARE  GIVEN A VALUE EQUAL TO THAT AT THE
C     SURFACE  SINCE  THERE ARE NO ATOMS  DIFFUSING OUT FROM
C     THE SURFACE. CN(31) ARE ALREADY KNOWN FROM THE EXTEND-
C     ED SPACE GRID USED (I.E. 60 INSTEAD OF 30 GRID POINTS)
C
      C1S = C1(1)
      C2S = C2(1)
      C3S = C3(1)
C
      D(1) = (DELT*D11/(2*DELX**2))*(2*C1(1)-C1(2)-2*C1S)-
     :C1(1)+(DELT*D12/(2*DELX**2))*(2*C2(1)-C2(2)-2*C2S)
     :+(DELT*D13/(2*DELX**2))*(2*C3(1)-C3(2)-2*C3S)
      D(2) = (DELT*D22/(2*DELX**2))*(2*C2(1)-C2(2)-2*C2S)-
     :C2(1)+(DELT*D23/(2*DELX**2))*(2*C3(1)-C3(2)-2*C3S)
     :+(DELT*D21/(2*DELX**2))*(2*C1(1)-C1(2)-2*C1S)
      D(3) = (DELT*D33/(2*DELX**2))*(2*C3(1)-C3(2)-2*C3S)-
     :C3(1)+(DELT*D32/(2*DELX**2))*(2*C2(1)-C2(2)-2*C2S)
     :+(DELT*D31/(2*DELX**2))*(2*C1(1)-C1(2)-2*C1S)
      DO 300 I=2,29,1
      D(3*I-2) = (DELT*D11/(2*DELX**2))*(2*C1(I)-C1(I+1)-
     :C1(I-1))-C1(I)+(DELT*D12/(2*DELX**2))*(2*C2(I)-
     :C2(I-1)-C2(I+1))+(DELT*D13/(2*DELX**2))*(2*C3(I)-
     :C3(I-1)-C3(I+1))
      D(3*I-1) = (DELT*D22/(2*DELX**2))*(2*C2(I)-C2(I+1)-
     :C2(I-1))-C2(I)+(DELT*D23/(2*DELX**2))*(2*C3(I)-
     :C3(I-1)-C3(I+1))+(DELT*D21/(2*DELX**2))*(2*C1(I)-
     :C1(I-1)-C1(I+1))
      D(3*I) = (DELT*D33/(2*DELX**2))*(2*C3(I)-C3(I+1)-
     :C3(I-1))-C3(I)+(DELT*D32/(2*DELX**2))*(2*C2(I)-
     :C2(I-1)-C2(I+1))+(DELT*D31/(2*DELX**2))*(2*C1(I)-
```

```
     :C1(I-1)-C1(I+1))
300   CONTINUE
      D(88)=(DELT*D11/(2*DELX**2))*
     :(2*C1(30)-2*C1(31)-C1(29))-C1(30)
     :+(DELT*D12/(2*DELX**2))*
     :(2*C2(30)-2*C2(31)-C2(29))
     :+(DELT*D13/(2*DELX**2))*
     :(2*C3(30)-2*C3(31)-C3(29))
      D(89)=(DELT*D22/(2*DELX**2))*
     :(2*C2(30)-2*C2(31)-C2(29))-C2(30)
     :+(DELT*D23/(2*DELX**2))*
     :(2*C3(30)-2*C3(31)-C3(29))
     :+(DELT*D21/(2*DELX**2))*
     :(2*C1(30)-2*C1(31)-C1(29))
      D(90)=(DELT*D33/(2*DELX**2))*
     :(2*C3(30)-2*C3(31)-C3(29))-C3(30)
     :+(DELT*D32/(2*DELX**2))*
     :(2*C2(30)-2*C2(31)-C2(29))
     :+(DELT*D31/(2*DELX**2))*
     :(2*C1(30)-2*C1(31)-C1(29))
C
C     SOLVE SYSTEM OF EQUATIONS
C
      JVMLF3=90
      JVMLF4=90
      JVMLF5=1
      JVMLF6=90
      JVMLF7=90
      JVMLF9=90
      CALL VMULFF(MAT,D,JVMLF3,JVMLF4,JVMLF5,JVMLF6,JVMLF7,
     :X,JVMLF9,IERR)
C
C     FROM X FORM CONCENTRATION VECTORS
C
      DO 400 I=1,30,1
      C1(I) = X(3*I-2)
      C2(I) = X(3*I-1)
      C3(I) = X(3*I)
  400 CONTINUE
C
      C1(1) = C10+C2(1)
C
      IF (NT.NE.NTV(INC)) GO TO 134
C
      DO 600 I=1,31,1
      XD(I)=(I-1)*DELX*1.E7
      X1(I)=C1(I)
      X2(I)=C2(I)
      X3(I)=C3(I)
```

```
      X1(I)=X1(I)*100.0
      X2(I)=X2(I)*100.0
      X3(I)=X3(I)*100.0
C
C     FILE 25 IS THE OUTPUT FILE
C
      WRITE(25,14) XD(I),X1(I),X2(I),X3(I)
 14   FORMAT(F8.3,2X,F8.3,2X,F8.3,2X,F8.3,2X)
600   CONTINUE
C
      YMAX(IP)=XMAX(IP)*10000000.0
      YP(IP)=XP(IP)*10000000.0
      CSIG(IP)=SIG(IP)*10000000.0
      FLUXX(JF)=FLU(JF)*1.0E9
      WRITE(25,66)
      WRITE(25,67)
      WRITE(25,68)
 66   FORMAT(1X,'IMPLANT    MAX   FLUENCE   RANGE   SIGMA ',
     :'   SPUT.     FLUX            ')
 67   FORMAT(1X,'ENERGY    DEPTH   (10**16)                ',
     :'      YIELD   (10**-9)       ')
 68   FORMAT (1X,' (KEV)    (NM)    (/SQ.CM)  (NM)     (NM)
     :            ')
      WRITE(25,69) ENERGY(IP),YMAX(IP),FLNC(INC),YP(IP),
     :CSIG(IP),SPUT(IS),FLUXX(JF)
 69   FORMAT (1X,F7.2,4X,F7.2,2X,F7.2,3X,F7.2,3X,F7.2,2X,
     : F7.2,3X,F7.2,6X)
      WRITE(25,666)
 666  FORMAT (1X,'DIFFUSIVITIES (SQ.CM/SEC)  ')
      WRITE(25,63)
 63   FORMAT (1X,'   D11          D12          D13        ',
     :'  D22          D33         ')
      WRITE(25,64) D11,D12,D13,D22,D33
 64   FORMAT (1X,5(E10.3,3X),7X)
      INC = INC + 1
 134  CONTINUE
      STOP
      END
```

Given below is the listing of the program used to plot the output generated by the program 'IMPLANT'.

```
C
C     THIS PROGRAM READS THE OUTPUT FROM THE PROGRAM
C     'IMPLANT' AND THE EXPERIMENTAL DATA FROM FILE 17
C     AND ILLUSTRATES THEM AS A GRAPH. THE PLOT IS BASED ON
C     THE PLOT10 PACKAGE SUBROUTINES.
C
      CHARACTER TIT2*32,TIT3*32,TIT4*27
      CHARACTER TIT2A*48,TIT3A*44
      DIMENSION TITLE1(16),TITLE2(21),TITLE3(19),TITLE4(7)
      DIMENSION TITLE5(16),DETL1(18),DETL2(18)
      DIMENSION X1(33),C1(33),C2(33),C3(33),X1X(33),X2X(33)
      DIMENSION C1X(33),C2X(33),C3X(33)
      DIMENSION LC1(5),LC2(6),LC3(6),LCX(3),LX(5),LY(5)
      DATA LC1/'EXPE','RIME','NTAL',' CAR','BON '/
      DATA LC2/'EXPE','RIME','NTAL',' TAN','TALU','M'/
      DATA LC3/'EXPE','RIME','NTAL',' CHR','OMIU','M'/
      DATA LCX/'CALC','ULAT','ED  '/
      DATA LX/'DEPT','H (N','ANOM','ETER','S)'/
      DATA LY/'CONC','ENTR','ATIO','N (A','T.%)'/
      DATA TIT2,TIT2A /' ENERGY    DEPTH    (&X10¬#16@) ',
     1'                        YIELD     (&X10¬#-9@)    '/
      DATA TIT3,TIT3A /'   (&K&EV)        (&N&M)      ( ',
     1'/&#CM@¬2)       (&N&M)       (&N&M)         '/
      DATA TIT4/'DIFUSIVITIES (&#CM@¬2/&S)'/
      READ (TIT2,21) (TITLE2(I),I=1,8)
      READ (TIT2A,22) (TITLE2(I),I=9,20)
      READ (TIT3,21) (TITLE3(I),I=1,8)
      READ (TIT3A,23) (TITLE3(I),I=9,19)
      READ (TIT4,24) TITLE4
   21 FORMAT (8A4)
   22 FORMAT (12A4)
   23 FORMAT (11A4)
   24 FORMAT (6A4,A3)
      IFVO=1
      READ (25,*) IPV,IFV,JFV,ISV
      CALL PLOTS (0.,0.,50)
      DO 134 IP=1,IPV
      IF (IP.EQ.2) IFV=IFV-1
      DO 134 IF=1,IFV
C     READING EXP DATA
      IXEXP = 31
      READ (17,*) (X1X(I),C1X(I),I=1,IXEXP)
      READ (17,*) (X2X(I),C2X(I),I=1,IXEXP)
C
```

```
      DO 134 JF=1,JFV
      DO 134 IS=1,ISV
      IX=31
      READ (25,*) (X1(I),C2(I),C1(I),C3(I),I=1,IX)
 69   FORMAT (16A4,///,18A4,//,16A4,/,18A4)
      READ (25,69) TITLE1,DETL1,TITLE5,DETL2
      CALL FACTOR (0.5)
      CALL SCALE (X1,11.0,IX,1)
      CALL SCALE (C1,10.,IX,1)
      CALL SCALE (X1X,11.0,IXEXP,1)
      CALL SCALE (X2X,11.0,IXEXP,1)
      CALL SCALE (C2,10.,IX,1)
      CALL SCALE (C1X,10.,IXEXP,1)
      CALL SCALE (C2X,10.,IXEXP,1)
      CALL PLOT (2.,3.5,-3)
      CALL PLOT (-1.00,15.50,3)
      CALL PLOT (12.00,15.50,2)
      CALL PLOT (12.00,11.50,2)
      CALL PLOT (-1.00,11.50,2)
      CALL PLOT (-1.00,15.50,2)
      CALL PLOT (-1.00,13.90,3)
      CALL PLOT (12.00,13.90,2)
      CALL PLOT (12.00,13.20,3)
      CALL PLOT (-1.00,13.20,2)
      CALL PLOT (-1.00,13.15,3)
      CALL PLOT (12.00,13.15,2)
      CALL PLOT (12.00,12.15,3)
      CALL PLOT (-1.00,12.15,2)
      CALL VPISYM (-0.80,15.10,0.2,TITLE1,0.0,64)
      CALL VPISYM (-0.80,14.6000,0.2,TITLE2,0.0,80)
      CALL VPISYM (-0.80,14.10,0.2,TITLE3,0.0,75)
      CALL VPISYM (-0.80,13.45,0.2,DETL1,0.0,72)
      CALL VPISYM (-0.80,12.750,0.2,TITLE4,0.0,27)
      CALL VPISYM (-0.80,12.35,0.2,TITLE5,0.0,64)
      CALL VPISYM (-0.80,11.750,0.2,DETL2,0.0,72)
      CALL PLOT (6.50,9.0,3)
      CALL PLOT (6.90,9.0,2)
      CALL SYMBOL (7.20,9.0,0.2,LCX,0.,12)
      CALL SYMBOL (6.70,8.4,0.2,2,0.,-1)
      CALL SYMBOL (7.20,8.4,0.2,LC1,0.,20)
      CALL SYMBOL (6.70,7.8,0.2,4,0.,-1)
      CALL SYMBOL (7.20,7.80,0.2,LC2,0.,21)
      X1(32)=AMIN1(X1(32),X1X(32),X2X(32))
      C1(32)=AMIN1(C1(32),C2(32),C1X(32),C2X(32))
      X1(33)=AMAX1(X1(33),X1X(33),X2X(33))
      C1(33)=AMAX1(C1(33),C2(33),C1X(33),C2X(33))
      DO 10 J=1,2
      C2(IX+J)=C1(IX+J)
      C3(IX+J)=C1(IX+J)
```

```
      X1X(IXEXP+J)=X1(IX+J)
      C1X(IXEXP+J)=C1(IX+J)
      C2X(IXEXP+J)=C1(IX+J)
      X2X(IXEXP+J)=X1(IX+J)
 10   CONTINUE
      CALL AXIS (0.,0.,LX,-18,11.0,0.,X1(IX+1),X1(IX+2))
      CALL AXIS (0.,0.,LY,20,10.,90.,C1(IX+1),C1(IX+2))
      CALL PLOT (10.0,0.,3)
      CALL PLOT (12.0,0.,2)
      CALL PLOT (12.0,10.,2)
      CALL PLOT (0.,10.,2)
      CALL LINE (X1X,C1X,IXEXP,1,-1,4)
      CALL LINE (X2X,C2X,IXEXP,1,-1,2)
      CALL LINE (X1,C1,IX,1,0,0)
      CALL LINE (X1,C2,IX,1,0,0)
      CALL PLOT (15.25,17.5,3)
      CALL PLOT (15.25,-3.5,2)
      CALL PLOT (18.0,-3.5,-3)
 134  CONTINUE
      CALL PLOT (2.0,0.0,999)
      STOP
      END
```

The vita has been removed from the scanned document